NASA/TP—1999–209576

The Geophysical Fluid Flow Cell Experiment

J.E. Hart, D. Ohlsen, S. Kittelman, and N. Borhani
University of Colorado, Boulder, Colorado

F. Leslie and T. Miller
Marshall Space Flight Center, Marshall Space Flight Center, Alabama

September 1999

The NASA STI Program Office…in Profile

Since its founding, NASA has been dedicated to the advancement of aeronautics and space science. The NASA Scientific and Technical Information (STI) Program Office plays a key part in helping NASA maintain this important role.

The NASA STI Program Office is operated by Langley Research Center, the lead center for NASA's scientific and technical information. The NASA STI Program Office provides access to the NASA STI Database, the largest collection of aeronautical and space science STI in the world. The Program Office is also NASA's institutional mechanism for disseminating the results of its research and development activities. These results are published by NASA in the NASA STI Report Series, which includes the following report types:

- TECHNICAL PUBLICATION. Reports of completed research or a major significant phase of research that present the results of NASA programs and include extensive data or theoretical analysis. Includes compilations of significant scientific and technical data and information deemed to be of continuing reference value. NASA's counterpart of peer-reviewed formal professional papers but has less stringent limitations on manuscript length and extent of graphic presentations.

- TECHNICAL MEMORANDUM. Scientific and technical findings that are preliminary or of specialized interest, e.g., quick release reports, working papers, and bibliographies that contain minimal annotation. Does not contain extensive analysis.

- CONTRACTOR REPORT. Scientific and technical findings by NASA-sponsored contractors and grantees.

- CONFERENCE PUBLICATION. Collected papers from scientific and technical conferences, symposia, seminars, or other meetings sponsored or cosponsored by NASA.

- SPECIAL PUBLICATION. Scientific, technical, or historical information from NASA programs, projects, and mission, often concerned with subjects having substantial public interest.

- TECHNICAL TRANSLATION. English-language translations of foreign scientific and technical material pertinent to NASA's mission.

Specialized services that complement the STI Program Office's diverse offerings include creating custom thesauri, building customized databases, organizing and publishing research results…even providing videos.

For more information about the NASA STI Program Office, see the following:

- Access the NASA STI Program Home Page at ***http://www.sti.nasa.gov***

- E-mail your question via the Internet to help@sti.nasa.gov

- Fax your question to the NASA Access Help Desk at (301) 621–0134

- Telephone the NASA Access Help Desk at (301) 621–0390

- Write to:
  NASA Access Help Desk
  NASA Center for AeroSpace Information
  800 Elkridge Landing Road
  Linthicum Heights, MD 21090–2934

NASA/TP—1999–209576

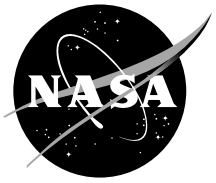

The Geophysical Fluid Flow Cell Experiment

J.E. Hart, D. Ohlsen, S. Kittelman, and N. Borhani
University of Colorado, Boulder, Colorado

F. Leslie and T. Miller
Marshall Space Flight Center, Marshall Space Flight Center, Alabama

National Aeronautics and
Space Administration

Marshall Space Flight Center • MSFC, Alabama 35812

September 1999

Acknowledgments

The authors thank the Microgravity Sciences and Applications Division of NASA for support of the GFFC flight experiment and the analysis of the unique data set obtained on USML2. We also are grateful to Gary Glatzmaier of Los Alamos National Laboratory who supplied some of the computational results for this publication.

Available from:

NASA Center for AeroSpace Information
800 Elkridge Landing Road
Linthicum Heights, MD 21090–2934
(301) 621–0390

National Technical Information Service
5285 Port Royal Road
Springfield, VA 22161
(703) 487–4650

TABLE OF CONTENTS

This report is organized as follows. The body of the report is a summary of Geophysical Fluid Flow Cell (GFFC) results from the United States Microgravity Laboratory USML - 2 in November 1995. The GFFC instrument previously flew on Spacelab 3 in May of 1985. However, results from this mission have previously been reported at length in the open literature. References to this are included in the bibliography. Following the main summary of results are a number of appendices which give more detailed discussions and presentations of the data in depth. Lastly, included with this report is a set of CD - roms which contain the data that has been extracted from the GFFC data films. These data include complete sets of images of the convection patterns observed during both SL - 3 and USML - 2, as well as raw and reduced instrument performance data gotten off the minute LED display layouts imbedded in the 16mm flight film data set.

1. INTRODUCTION

Large-scale motions of the atmospheres of planets and in the convection zones of rotating stars are strongly constrained by rotation, under the action of Coriolis forces, and gravity, which is manifest in the buoyancy forces that drive thermal circulations. The resulting flow structures are often surprising and continue to baffle scientists seeking fundamental understanding of such phenomena as the zonal bands of Jupiter, the origin of extremely high winds in the tropics and subtropics of Jupiter, Saturn and Neptune, the persistent differential rotation of the Sun, the complex patterns of convection in the slowly-rotating mantle of the Earth, and the rapidly rotating flows in the Earth's core that are thought to generate the Earth's magnetic field.

Several idealized theories have been offered as explanations for some of these phenomena. Busse (1970, 1973, 1983) considers that Coriolis forces associated with planetary rotation dominate the large-scale (global) dynamics on the major planets. He hypothesized that motions in planetary atmospheres are constrained by the Taylor-Proudman theorem, which states that winds should be invariant along the axis of rotation for sufficiently high planetary rotation. His idea is sketched in figure 1. The axial invariance leads to a set of nested cylinders with convection occurring as columnar pipes inside the cylinders. Nonlinear interactions of individual convection columns can lead to large scale "zonal" winds (i.e. winds that are invariant with changes in longitude). The theories of Busse presume that the Taylor-Proudman theorem applies. However, this constraint is known to break down when stratification or turbulence (e.g. small-eddy viscosity) is strong enough. The precise nature of the breakdown of axial invariance due to turbulence is not known. A major goal of the USML2 experiments was to observe the parameter-space dependence of this process for comparison with scaling theory and computational simulations.

2 THE PRINCIPLE OF THE GFFC

The microgravity laboratory allows the study of fundamental physical processes that are masked or overpowered by gravitational influences in the terrestrial laboratory. One such physical force in dielectric liquids is that due to imposed electric fields. In a thermally stratified fluid, the dielectric polarization force is small compared to gravitational thermally induced buoyancy unless the field strengths and dielectric constant are unrealistically large (e.g. the electric field is well above the dielectric breakdown point). Therefore microgravity is required. The GFFC is an instrument based on electrohydrodynamic flow instability in a spherical annular geometry. It can be shown that for the particular electrodynamic system we use, the dominant flow instability is directly analogous to the buoyancy driven modes in rotating spherical shells. Thus observations of the evolution of the electrohydrodynamic instabilities, and their dependence on rotation rates and other parameters, show us how normal buoyant fluids should behave in the presence of heating and radial gravity.

Detailed descriptions of the GFFC experiment have appeared previously (Hart et. al., 1986a,b, 1990, 1991), so only a brief overview is given here. Fig. 2 shows a cross-section of the working

cell. A dielectric silicone oil is contained in a hemispherical annular gap between a nickel sphere and a sapphire dome. The gap $d = R_o - R_i$ is about 1 cm (see table 1). By using servo-controlled heaters imbedded in the inner sphere, and at the pole and equator of the outer sphere, various temperature distributions can be set up on the two surfaces bounding the working fluid. These are denoted $T_i(\theta)$ and $T_o(\theta)$ respectively, where θ is the latitude. The simplest applied heating occurs when T_o and T_i are constant with $T_i > T_o$. This latitudinally invariant convectively unstable heating distribution corresponds, for example, to astrophysically motivated simulations of stellar convection where nuclear burning at the core leads to a spherically symmetric destabilization of the convection layer. Latitudinally varying heating relates to planetary convection situations where the differential heating from the Sun either dominates or significantly affects the circulation in the fluid. Cases with a hotter pole or a hotter equator are both of interest. The latter has obvious connections to terrestrial planets like the Earth, but the geophysically relevant distribution of boundary temperature depends on how, in the case of planetary atmospheres, solar radiation is deposited with altitude.

A large alternating voltage V_o is imposed across the working fluid (a transparent but electrically conducting coating of Indium is applied to the inner surface of the sapphire dome for this purpose). The hemispherical annular gap shown in fig. 2 is continued below the equator to form a spherical capacitor. The large voltage (up to 10 kilovolts rms) gives rise to a substantial electric field in the fluid. There then occur both electromagnetic and gravitational buoyancy forces in the fluid which are given by

$$\bar{F} = q\bar{E} - \frac{1}{2}E^2\nabla\varepsilon + \frac{1}{2}\nabla\left\{E^2\rho\frac{D\varepsilon}{D\rho}\right\} - \bar{g}\,\rho \qquad (1)$$

where q is the free-charge density, E(r,t) the instantaneous electric field which is a function of radius r and time t, ρ the fluid density, ε the dielectric permittivity, and g the gravitational acceleration. E^2 is the dot product of the electric field vector.

The use of an alternating potential with a frequency large compared to the charge relaxation time for the silicone oil working fluid leads to a negligible contribution from the first term on the right side of (1). Because the oil is incompressible and divergence free, the flows are governed by vorticity equations. Thus the dynamically relevant forces are those which survive after taking the curl of eqn. (1). Namely,

$$\nabla\times\bar{F} = \rho_o\alpha\nabla T\times\nabla\phi + \varepsilon_o\frac{\gamma}{2}\nabla T\times\nabla E^2 \qquad (2)$$

where we have substituted the equations of state $\rho = \rho_o(1-\alpha T)$ and $\varepsilon = \varepsilon_o(1-\gamma T)$ for the density ρ and the permittivity ε as a function of the temperature T. Here α is the coefficient of thermal expansion and γ is the dependence of the dielectric constant on temperature. ϕ is the geopotential associated with whatever real gravity is present. Equation (2) shows that E^2 plays the same role as the geopotential in the dynamics.

Because $E^2 = \vec{E} \bullet \vec{E}$ has a time-average part that goes like r^{-4}, $\nabla E^2$is a radial vector decreasing like r^{-5} For the narrow gap used in the experiment the difference between r^{-2} and r^{-5} is relatively insignificant. However, because ε is quite small for non-polar fluids that can withstand a large applied potential, the electrodynamic buoyancy torques resulting from the curl of the polarization forces is small compared with terrestrial gravity. This smallness of the electrohydrodynamic polarization force is the main reason for placing the GFFC experiment in a microgravity environment. For example, table 1 gives typical values for the various parameters in the GFFC experiment. As shown in Hart et. al. 1986a, the effective electromagnetic gravity is

$$g_{em} = 2\varepsilon_o \frac{V^2 \beta^2 R_o^5}{(1+\beta) d^3 \rho r^5}$$

where r is the radius and β is the ratio of the gap width d to the inner radius. Using a maximum voltage of 10 kilovolts and the values in table 1, it can be seen that the effective gravity is about 0.13 g's or less at the outer boundary, decreasing as V is lowered.

3. PREVIOUS TERRESTRIAL EXPERIMENTS IN RELATION TO GFFC

Previous laboratory studies of convection have been constrained to rotating layers between parallel plates oriented perpendicular to gravity (e.g. Rossby, 1969). This is because when rotating shells are used, terrestrial gravity is no longer everywhere perpendicular to spherical surfaces so that symmetry with respect to geopotential is lost and anomalous motions are generated. Even so, laboratory experiments in planar layers of rotating fluids have previously played a significant role in geophysical fluid dynamics. However, because terrestrial gravity and rotation are parallel in these experiments, only dynamics relevant to the polar regions of planetary atmospheres are addressed. Indeed it has long been a goal of fluid dynamicists to warp gravity in such a way as to allow a continuous variation of the angle between rotation and gravity vectors as is found in atmospheres and oceans of global extent. Prior to the GFFC this was only possible in a fluid of constant density, or in fluids with a very limited representation of thermal stratification. For example, Hart (1972) studied β-plane dynamics for two immiscible fluid layers in which the aforementioned angle varies from one side of the experiment to the other.

4.1 CONTROL PARAMETERS AND EXPERIMENT PROCEDURES

There are four fundamental dimensionless parameters for the GFFC. The Prandtl number (the ratio of kinematic viscosity to thermal diffusivity) is fixed at 8.4. The aspect ratio β is fixed at 2.65. The Taylor number

$$Ta \equiv 4\Omega^2 d^4 / \nu^2 = 2.43 x 10^6 / \tau^2$$

(where τ is the rotation period of the cell) measure the effects of rotation relative to viscosity. The period ranged from 2 to 255 seconds. The Rayleigh number

$$Ra = g_{eff}\gamma\Delta T d^3 / \kappa\nu = 218.4\nabla T V^2 ,$$

where ∇T is the applied radial temperature difference (degrees C) and V is the applied voltage in kilovolts, measures the relative effects of buoyancy and diffusion. MOST OF THE RESULTS IN THIS PAPER ARE GIVEN IN TERMS OF VOLTAGE AND PERIOD, SO THE ABOVE RELATIONS MUST BE USED TO CONVERT TO DIMENSIONLESS PARAMETERS WITH PHYSICAL SIGNIFICANCE. The temperature differences was typically about 15 degrees while the applied voltages ranged from 0 to 10 kV. In addition to these non-dimensional number relating the magnitudes of the experimental controls, there is also the prescribed distribution of temperatures on the inner and outer spheres. These scale with ∇T, but with spherically symmetric thermal boundary conditions no additional information is required to specify the system. On SL - 3 an extensive set of experiments with a latitudinal component to the heating were attempted. These were intended to mimic the fact that Jupiter's atmosphere may be excited by both the Sun (giving a latitudinally varying heat input) and from internal heating (presumed to be isotropic). A few runs with latitudinal heating were attempted on USML-2 (we had hoped to do many). However, on USML-2 the thermal control system appeared not to be working properly, so such runs with large latitudinal gradients were curtailed. In any case a parameter

H = pole to equator temperature difference / inner to outer radial temperature difference

distinguishes between the various cases. In particular:

H = 0 is called the "Solar" case, because it is thought that the solar atmosphere is not excited by a latitudinally varying heat source.

H = 1 to 4 is called the "Jovian" case, for reasons stated above. Computational simulations and SL - 3 experiments were done for H = 1 to 3 . On USML-2 we had hoped to do runs with H = 3 and 4, but this proved impossible.

Figure 3 shows a schematic of the GFFC instrument as flown on USML2. The cell is mounted on a turntable containing devices to regulate the temperature on the spherical shells. Visualization of the electrohydrodynamical buoyancy modes is obtained remotely, as any probes will perturb the desired spherical symmetry of the electric field and would find themselves in a very hostile electromagnetic environment. An aspheric lens assembly projects a Ronchi ruling onto the inner sphere. This is reflected back upon the ruled grid itself and the resulting image is then photographed on 16mm film. Upon traversing the working fluid, light rays are bent due to index of refraction fluctuations in the silicone oil that are in turn caused by temperature variations in latitude or longitude. Thus the film records images which depict radially averaged horizontal temperature gradients in the fluid. These reveal patterns of convection which arise under various external conditions: rotation rate Ω, applied gravity (i.e. V), and heating distribution. During the filming, experiment performance data are recorded in digital (both decimal and binary) form on each frame. After the mission these data were read by a digital image acquisition system on the ground after the film is processed. The images of the convection cell were also recorded by a video camera. This video image includes four pieces of information concerning the experiment parameters. This is a very small fraction of the

parameter and performance data recorded on the 16mm film. Thus the film was the primary data storage medium for refined analysis after the flight, but the video system allowed for interactive experiments to be carried out during the USML-2 mission.

Figure 3b illustrates the part of the GFFC hemisphere that is seen by the film and video camera. Although coverage includes the entire 90 span in latitude, only a limited range of longitude is covered. However, by combining 8 successive images that are taken each 45 degrees in longitude, we can present full hemispherical views. This works well for medium rotation rates (so the camera can take 8 images around a circumference quite rapidly), and for slowly evolving convection states (so that the convection is quasi-steady for one turn of the cell. The procedure for unwrapping the imagary is explained in APPENDIX 2.

The generic experiment procedure was:

a) Fix the external parameters of the experimental run. These are the rotation rate Ω, the photography protocols, and the boundary temperature distributions.

b) After an initial setup begin taking 16mm photographs through the backfocus Schlieren system. The frame rate was about 1 per rotation of the cell at high rotation rates (Ω> 1 radian per sec.), making it possible to reconstruct a long time series of images to look for periodicities, aperiodicity, etc.

c) Repeat with the new Ra (obtained by ramping or jumping the applied voltage V).

d) After a range of Ra's are explored at fixed Ω, Ti, and To, move on to cases with different rotation rates and heating distributions. Each Ra ramp experiment lasted 6 hours. In all, thirty 6 hour runs were made.

4.2 INSTRUMENT PERFORMANCE

During the USML2 mission the downlinked astronaut monitoring information suggested there was a problem with the thermal controller. The actual temperatures obtained on the spheres did not match the commanded values very well. The binary LED data on the film, after using the postflight thermal calibration curves, confirmed this. Figures 4 and 5 illustrate the history of boundary temperatures for two 6 hour runs. Both runs have horizontally uniform commanded temperatures of 25 (outer sphere) and 40 (inner sphere) degrees. Because of calibration shifts (possibly during launch), the controller thought the outer sphere was too hot, and reacted by cooling it too much. However, during the run, as convection transferred heat from the inner to the outer sphere, the instrument cooler could not keep up and the inner sphere drifted upwards. Also notable is the non-uniformity of inner sphere temperature, approaching 10 percent of the applied gradient. APPENDIX 1 contains a summary of all the runs (which had film recording, see below). These detailed results are consistent with the comments made above.

The astronaut monitors of the instrument panel suggested that experiments which commanded large imposed latitudinal temperature differences (with latitudinal variations as large or larger

than the requested radial variation) were in thermal error by order one amounts. In these cases, use of the postflight calibration indicated better performance than expected from the real-time monitoring data sent down during the flight, but still with considerable (30 percent) differences from the commands. This means that it will likely be necessary to use the detailed thermal data taken from the film to build useful interpretive computational models of the GFFC results because one cannot rely on the assumption that the commanded temperatures actually were attained during the USML2 runs. Unfortunately the film camera failed during run 19 (out of 30), so that is impossible to get detailed quantitative results from the last 11 experiments because precise data on the thermal boundary conditions are not available for these runs. However, the downlinked video provides some qualitative information on flow states. Nonetheless, it was decided to concentrate our analysis and interpretation efforts on the 16mm film because of the much more complete instrument thermal records and much higher and more uniform temporal sequencing of the imagery.

5 RESULTS FOR SPHERICALLY SYMMETRIC HEATING

Runs 1 through 19 concentrated on the issue of the evolution of convection with spherically symmetric heating. Of these 19 runs, for which full 16mm film data were obtained, only runs 2 and 19 had commanded non-symmetric (i.e. latitudinally varying) thermal boundary conditions.

Figure 6a summarizes several of these spherically symmetric runs by showing individual snapshots of the convection on the parameter plane of the experiments. H = 0 denotes spherically symmetric heating. Each image shows the equivalent of an astronomer's telescopic view of a star with the south pole at the bottom and the equator at the top (see figure 3b for a detailed discussion of the viewing). For high Taylor number (low rotation period, e.g. 2 seconds) the convection initiates as prograde propagating polar disturbances, followed closely, as Ra is increased, by north-south oriented columnar ("banana cell") modes (compare to figure 1).

The GFFC camera can be set to take a sequence of images each 45 degrees in longitude. If the motion is not evolving too fast in time, it is possible to take a set of 8 of these telescopic views, unwrap the peculiar birds-eye geometry, and merge the images into a full hemispheric (equal latitude line) projection. Figure 7 illustrates one example of this processing technique for a state with both propagating banana cell disturbances and non-periodic polar waves. A computational simulation of this state by Miller and Leslie is included for comparison. At weak to moderate supercriticality the comparison between simulation and experiment is reasonably good.

As Ra moves higher so that the motions become turbulent, the polar convection eats northwards into the banana cell regime, basically eliminating the presence of axially symmetric elements in the motion. As the period of rotation is increased, the convection states become more complicated. The separation of polar and banana cells decreases and the eradication of banana cells with increasing Ra is more rapid.

At very low Taylor number (long period of rotation) the convection is more transitory and patterns are less well defined. However, some runs showed evidence for persistent states with

relatively simple geometry. Figure 8 shows some examples from a run with a 48 second period. The voltage was commanded to ramp quickly to 1.5 kV, hold there, then run up to 3.5 kV and back down down to hold at 1.5 kV again. During the first four hours of the run the states (fig. 8a, b) were irregular in time and space. However, the system finally settled down into a persistent wavenumber two propagating eddy (8c). One possible conclusion is that the system exhibits hysteresis (e.g. 8a and 8c are two fundamentally different states that are possible at essentially the same parameter setting). However, because the flows near 8a are not periodic, while 8c is, another interpretation is simply that it takes many hours for the fluid system to equilibrate and the images in 8a and 8b have not reached statistical equilibrium.

5.1 COMPUTATIONAL SIMULATION OF SPHERICALLY SYMMETRIC FLOWS

Figure 9 shows a regime diagram obtained from a 3D computational "Miller-Leslie" model (a variant of that described by Miller, et. al., 1992) using 30 radial points, 62 latitudinal points and 45 longitudinal wavenumbers. The model boundary conditions correspond to the experiment, except that purely symmetric temperatures (e.g. averaging fig. 4 in latitude) were used. At high Taylor number the states are similar with prograde propagating polar modes coming in first as Ra in increased, and clear indication of banana cells in the mid-latitudes and tropics. The states at low Taylor number appear to be more stable (less transitory) than in the experiments. Multiple states (or hysteretic behavior) were found in the simulations. For example there are two qualitatively different but persistent states of motion at Ta= 1000, Ra = 20,000. In general, the simulations using this model do a good job at describing the motions at high Ta and low to moderate Ra, but seem to give overly simple states at low Ta. At low Ta the onset of convection occurs at a lower Ra, and the supercriticality, at a fixed voltage (3 kV, for example), is much higher so that there may be resolution problems in some of the low Ta runs. Also, at this time it is not known how sensitive the computed flows are to modest latitudinal variations in the boundary temperatures.

5.2 THE ONSET OF CONVECTIVE INSTABILITY

A new camera action protocol, implemented on the USML2 flight that gives a closely spaced time series of images at a fixed longitude permits an accurate determination of the onset of convection (i.e. the fundamental horizontal symmetry breaking instability). Figure 10 shows the observed onset points. As illustrated in figures 6 and 7, there are two types of modes, prograde polar and prograde propagating banana cells, the latter having strong north-south alignment. The experimental curves represent fits through data from 9 runs at different rotation rates. At high Ta polar modes come in first as Ra is raised, while at lower Ta the banana cells onset first. Figure 7b shows the onset wavenumber and propagation rates for banana cells. The wavenumber drops rapidly as the rotation period increases, as does the prograde propagation rates of the banana cells.

Onset data can be compared with predictions of computational simulation, and this provides a useful validation of the latter because the weak motions associated with the instability tests most of the terms in the model while not requiring enormous 3D resolution. Figure 10 shows that the

Miller-Leslie model comes quite close the experimental result for the 4 second period, although the separation between polar and banana modes is smaller than observed and the onset points are slightly higher. More simulations that include a fit to the actual (not smoothed) thermal boundary conditions are planned. The Glatzmaier (1983, see also Hart, Glatzmaier, Toomre, 1986) model has higher resolution, but because it is a pseudo-spectral code, it does not implement the rigid boundary condition of the GFFC present at the equator (see figure 2). The tips of the banana cells should generate Ekman layers long the equatorial barrier, and should be more damped in the presence of this wall. Thus it is not too surprising that the Glatzmaier model predicts that banana cells should arise first, at a lower Ra.

5.3 TRANSITION LATITUDES FOR TURBULENT FLOWS

A very important result from the GFFC experiments, obtained by combining data from the 18 runs done with symmetric heating, is an estimate of the parametric conditions required to observe axial (banana cell) convection in highly nonlinear and turbulent flow. Such results cannot be obtained computationally over the entire range of the GFFC parameter values. What is the latitidunal limit for banana (axially aligned) structures in the flows? If this critical latitude shrinks to zero, then the object will not have a banana cell regime. If the results from the experiments conform to an asymptotic scaling relation, then it might be possible to use the GFFC results to predict whether or not a rotating star or planet will have aligned giant cells in its atmosphere. Fig. 10 shows data for one rotation rate. As the voltage increases the banana cell domain shrinks towards the equator. For V > 8 kilovolts, the basic planetary rotation is too weak to align the motion in the north-south direction.

Attempts to derive a scaling in this complex geometry typically involve some perhaps tenuous assumptions, but the GFFC results can be used as an independent check. One simple idea is that the transition boundary is related to the existence of more constrained geostrophic convection equatorward of a transition latitude θ, and we take θ to be the latitude at which the convection has unit Rossby number. The Rossby number measures the relative strengths of advection and Coriolis forces and is given by $R_o = U / 2\Omega \sin(\theta) d$ where U is a characteristic convection velocity. If we take the convection velocity to be estimated by buoyancy-induced free fall, then $\approx \sqrt{g_{em} \gamma \Delta T d}$ and setting the Rossby number equal to 1 gives the scaling relation (for fixed Prandtl number):

$$\sin(\theta) \propto R_o^{-1/2} T_o^{1/2} \propto (\tau V)^{-1}. \qquad (3)$$

An alternative model, using estimates of U from the numerical β-convection model of Brummell and Hart (1992) that includes local boundary curvature in the dynamics, gives a somewhat different scaling:

$$\sin(\theta) \propto R_o^{-3/4} T_o^{15/24} \propto V^{-3/2} \tau^{-5/4}. \qquad (4)$$

In the second result the transition latitude falls faster with V because in the Brummel-Hart free slip β-convection model, the motions develop high speed jets by mean flow instability. The

zonal flows dominate the convection and the high velocities associated with these jets lead to a prediction that unit Rossby number is reached sooner .

Fig. 11 shows that the data are consistent with the simple thermal Rossby number scaling. The data are not consistent with the β-convection scaling. This is in concert with the observation from GFFC that no high speed jets (which would be associated with anomalous disturbance propagation rates) were observed. Also, the β-convection model predicts vacillatory states involved with mean flow instability. Such periodic pattern pulsation states were not seen in the USML2 GFFC results either. Thus full sphericity seems to detract from the potential for strong jet formation. This result needs to be tempered by the possibility that the GFFC experiments, conducted with a Prandtl number of 8.4, may not accurately predict what might happen in a low Prandtl flow, or in atmospheres with forcing parameters well outside the GFFC experimental range. If, however, the Prandtl number dependence turns out to be weak (as checked, perhaps, by computational simulation), the scaling (3) may allow determination of the flow regimes to be expected in rotating stars and planets where the applied temperature difference (or supercriticality) is known. Unfortunately whereas (3) is independent of diffusion parameters (a plus!), if one must use observations of emitted heat flux in order to estimate the Rayleigh number (through a Nusselt number scaling), this then re-introduces the thermal diffusivity into the scaling. Future work in the application of such scaling relations as (3) and (4) to astrophysical situations will determine whether or not the obstacle of having only a poor knowledge of small-eddy diffusivity is significant.

6 CONCLUSIONS

The GFFC experiments on USML2 returned an extensive data set on the nature of convection in rotating spherical shells with nearly horizontally symmetric applied thermal boundary conditions. The main results extracted to date have many facets. Some results are discouraging with respect to our initial expectations, but some results were surprising and should provide fuel for more theoretical investigation and computational simulation that will increase our general understanding of rotating convection in spherical shells:

On the down side:

1) There was lack of experimental evidence for vacillatory states of convection that had been predicted in some simple theoretical models. This may be a geometry and Prandtl number problem.

2) There was no robust evidence for banding or axisymmetric jet formation as hoped for in order to explain differential rotation on the Sun or the multiple zonal jets on the giant planets. We did observe differential propagation of patterns (prograde , retrograde, prograde, moving from equator to pole), suggesting three different zones of instability. We do not know whether or not mean zonal motion plays a role in the differential propagation (perhaps computational simulations could help here), but whatever mean flows are present seem weak compared with the overturning motions of the convection eddies (i.e. the propagation rates are slow compared with the pattern fluctuation timescales).

These experiments seem to rule out rapidly rotating banana cell convection as a cause for these phenomena when operating over the parameters range studied here. Thus, if banana cell convection is the root cause, it must be operating at a significantly different setting. A possibility is that parameters may be such as to place the system in the banana republic regime (see figure 11), but at a much higher Rayleigh and Taylor number. Experiments could address this situation only in a geometry with a much larger gap width.

3) Although SL-3 returned some very interesting data on H unequal to zero flows (that were successfully interpreted using theory and numerical models), USML-2 experiments had difficulty in replicating or extending the SL - 3 experiments because of thermal control problems.

On the plus side:

1) There is good agreement between computational simulations of the onset of instability and the experiments.

2) The observation of much more complicated and transitory convection at low rotation than found in the computational simulation models suggests a sensitive dependence on physical boundary conditions, or on computational resolution. An unraveling of this situation by the modelers will no doubt improve our ability to simulate flows of this type.

3) Unanticipated patterns of convection at modest rotation rates (i.e. 16 second and 48 second periods) also will prove to be a useful challenge to computational codes. The mixture of quasi-axisymmetric motions at mid latitudes with non-axisymmetric motions at the pole and the equator is particularly surprising. The degree to which this may be related to the presence of the equatorial baffle in the GFFC instrument remains to be sorted out.

4) Approximate verification of a simple scaling law for the existence of columnar convective turbulence in highly stressed shells. This relation and its simple physical interpretation should be useful in categorizing the convection state of rotating geophysical objects like planets and stars.

All in all, the two flights of the GFFC have provided much data on rotating convection over about 80% of the parameter range in the original design. There is still much work necessary to interpret physically the results from USML-2, particularly in the low rotation cases.

7 SUGGESTIONS FOR FURTHER ANALYSIS

Future analyses and comparisons with models should focus on how weak latitudinal variation in boundary temperatures may influence the dynamics, whether or not simulations with higher resolution can recover some of the low rotation GFFC results, and on further characterizations

of the important high Rayleigh number turbulent states observed in rotating spherical shells. Some of the more interesting questions to pursue include:

1) Can the transition latitudes for banana convection be reproduced computationally?

2) What caused the bizarre patterns of convection at low rotation (e.g. appendix 2, figs 4 -7)?

3) Were 6 hour runs long enough to reach equilibrium? The models currently suggest much faster adjustment times than were observed experimentally. Are the models internally incorrect in their numerics, etc., or are they missing some essential physics? Perhaps the convection patterns at low rotation are very sensitive to the precise distribution of temperature on the boundaries, not only spatially, but temporally. In the USML-2 GFFC runs the temperatures did drift with time (by of order 10 - 20 %). Was this enough to keep some of the experiments from settling into a steady pattern?

On the experimental side, the use of electrostatically generated radial gravity in the configuration of the GFFC has proved its benefit and feasibility. However, to extend the range of parameters into more practically significant ranges, with Taylor and Rayleigh number thousands of times larger than that possible in the GFFC, an entirely new concept will be needed. This parameter range will likely elude modelers for many years, but is of much interest geophysically. We still don't understand the manner in which large scale coherent banana cell structures may re-emerge in a flow whose transition latitude has long ago (in a parameter sense) reached the equator. The intriguing possibility that sufficiently turbulent convection with many small eddies may organize itself into large scale structures (by collective action of the small scale eddies) might be addressed by laboratory experiments with a much deeper ($\times$ 20 or more) gap. The use of ferromagnetic fluids merits study in this regard.

8. ACKNOWLEDGMENTS

The authors would like to thank the Microgravity Sciences and Applications Division of NASA for support of the GFFC flight experiment and the analysis of the unique data set obtained on USML2. We also are grateful to Gary Glatzmaier, of Los Alamos National Laboratory who supplied some of the computational results for this publication.

9. REFERENCES

Brummell, N., and Hart, J.E., 1992, High Rayleigh number β-convection. *Geophys. and Astrophys. Fluid Dynamics*, **68**, 85 - 114.

Busse, F.H. 1970. Thermal instabilities in rotation systems. *J. Fluid Mech*, **44**, 441-460.

Busse, F.H. 1973. Differential rotating in stellar convection zones II. *Astron. and Astrophys.*, **28** 27-37.

Busse, F.H. 1983. A model of mean zonal flows in the major planets. *Geophys.and Astrophys. Fluid Dyn.*, **23**, 153-174.

Glatzmaier, G.A. 1983. Numerical simulations of stellar convective dynamos. I. The model and method. *J. Comp. Phys* , **55** ,461-484.

Hart, J.E. 1972 Experiments with two-dimensional rectilinear convective rolls at super-critical conditions. *Phys. Fluids*, **150**, 203-205.

Hart, J.E. 1972 A laboratory study of baroclinic instability. *Geophys. & Astrophys. Fluid Dynamics*, **3**, 181-209.

Hart, J.E., Toomre, J., Deane A., Hurlburt, N.E., Glatzmaier, G.A., Fichtl, G.H., Leslie, F., Fowlis, W.W. and Gilman, P.A. 1986b. Laboratory experiments on planetary and stellar convection performed on Spacelab 3. *Science*, **223**, 61-64.

Hart, J.E., Glatzmaier, G.A., and Toomre, J. 1986a. Space-laboratory and numerical simulations of thermal convection in a rotating hemispherical shell with radial gravity. *J. Fluid Mech.*, **173**, 519-544.

Hart, J.E., 1990. Microgravity laboratory simulations of planetary and stellar circulations. *Microgravity Science and Technolog y*, **3** , 143-147.

Miller, T.L., Lu, H.I., and Butler, K.A., 1992. A fully nonlinear, mixed spectra and finite-difference model for thermally driven, rotating flows. *J. Comp. Phyiscs.* **101**, 265-275.

Rossby, H.T., 1969 An study of Benard convection with and without rotation. *J. Fluid Mech.*, **36** , 309-335.

Toomre, J., Hart, J.E., and Glatzmaier, G.A. 1987 Spacelab experiments on convection in a rotating spherical shell with radial gravity. In *The Internal Solar Angular Velocity*, Ed. B.R. Durney and S. Sofia, 27-44, D.Reidel.

Table 1. Experiment parameters and characteristics of Dow Corning 0.65 centistoke silicone oil.

Nominal Fluid Properties (Dow Corning 0.65 cs 200 Fluid)		
Ambient density	$\bar{\rho}$	$760\ \mathrm{kg/m^3}$
Expansivity	α	$1.34 \times 10^{-3}\ ^\circ\mathrm{C}^{-1}$
Kinematic viscosity	ν	$6.5 \times 10^{-7}\ \mathrm{m^2/s}$
Thermal diffusivity	κ	$7.7 \times 10^{-8}\ \mathrm{m^2/s}$
Ambient permittivity	$\bar{\epsilon}$	$2.5\epsilon_0$
Vacuum permittivity	ϵ_0	8.90×10^{-12} farad/m
Dielectric variability	γ	$1.29 \times 10^{-3}\ ^\circ\mathrm{C}^{-1}$
Conductivity	σ	10^{-12} mho/m
Heat capacity	c	1.7×10^3 joules/kg °C
Dissipation loss factor	ϕ	$\approx 4 \times 10^{-5}$
Nominal Experiment Parameters		
Rotation rate	Ω	0–3 rad/s
Radial temp. difference	ΔT_r	0–25 °C
Voltage (r.m.s.)	V	0–10 kV
Voltage frequency	ω	300 Hz
Inner radius	R_i	2.402 cm
Outer radius	R_o	3.300 cm
Gap	d	0.908 cm
Aspect ratio	$\beta = R_i/d$	2.65
Prandtl number	Pr	8.4

TABLE 1

TABLE 2: GFFC (6 HOUR) RUNS PERFORMED ON USML-2, 1995

Run Number	Scenario Number	Rotation Period	Commanded / Obtained TOE	TIE	TOP	TIP	Voltage	Film Magazine	Camera Action	Comments
1	15	2	25 27.4→33.6	40 40	25 27.9→34.3	40 41	2→10	1248	3	Solar Ramp
2	136	48→5	20 29.8	30 39.7	30 30.3	40 40.7	3	1248	2	
		8	20 33.6→33.8	30→25 43.5→38.7	30→35 34.3→36.0	40 44.2→40.7	5→10		3	
3	22	4	25 32.2→34.2	30 31.1→32	40 37.5→40.6	45 43.6→45.2	2→10	1244	3	Baro Ramp H-3 not very well
4	17	4	25 25.6→31	40 39.9→40.1	25 26.3→31.1	40 40.7→40.1	2→10	1244	3	Solar Ramp
5	112	4	25 27.2→30.8	40 40	25 27.8→32.4	40 40	1→9	1244	8	Solar Ramp
6	182	8	25 25.6→31.0	40 40	25 26.2→31.0	40 40.7	0→9	1245	3	Solar Ramp
7	181	16	25 27.9→31.0	40 40	25 27.9→32.6	40 40.5	0→9	1245	2	Solar Ramp
8	171	3	25 25.6→31.0	40 40	25 26→32.4	40 42.4→40.7	1→9	1246	9	Solar Ramp
9	172	6	25 27.8→31.1	40 40	25 27.9→32.6	40 40.7	1→9	1246	9	Solar Ramp
10	198	48	25 25.6→30.0	40 40	25 26.3→31.1	40 40.7	0.52→8	1246	2	Mantle Ramp
11	191	96	25 25.6→29.8	40 40	25 26.2→31.1	40 40.7	0→9	1335	2	Mantle Ramp
12	145	4	25 25.6→31.1	40 40	25 26.3→37.5	40 42.4→40.7	0→9	1335	9	Solar Ramp
13	192	128	25 27.5→29.4	40 40	25 27.9→30.4	40 40.7	0.52→5	1335	1	Mantle Ramp
14	193	240	25 25.8→29.8	40 40.2→40.0	25 26.3→30.8	40 40.7	0.52→5	1335	1	Mantle Ramp
15	194	48	25 26.2→29.5	40 39.8→40.0	25 26.8→29.9	40 40.7	0.8→3.5 →0.8	1335	2	Look for Mantle Hyst. ●1.6kV
16	195	128	25 29→29.8 →29.2	40 40→39.8	25 29.6→30.4 →29.6	40 40.7→42.4 →40.7	0.8→3.5 →0.8	962	1	Look for Mantle Hyst. ●1.6kV
17	196	48	25 29.8→30.4	40 40.2→39.8	25 30.6→31.1	40 40.7	3, 1, 2, 1, 3, 2	962	2	Look for Mantle Hyst.
18	197	128	25 29.4→30.8	40 39.8→40.1	25 30.2→31.1	40 42.4→40.7 →42.4	2, 3, 1, 2, 3, 2	962	1	Look for Mantle Hyst.

Run umber	Scenario Number	Rotation Period	Commanded / Obtained TOE	TIE	TOP	TIP	Voltage	Film Magazine	Camera Action	Comments
19	161	48	30 36.4→37.5	45 45.8→44.8	45 43.4→45.5	55 53.5→56 →55.3	0.44→4	962	2	Jovian Lo V Ramp ·No film last 1/3?
20	29	48	25 27.9→31.1	35 35.2	35 36→34.3	45 45.6→43.9 →45.6	2→10		2	Jovian Hi V Ramp No film
21	163	2	30 35.9→37.5	45 45.2→44.8	45 42.8→45.6	55 55.2→53.5 →55.2	3→9	1247	8	Jovian Hi V Ramp No film last 1/6
22	164	8	30 35.8→40.2	40 39→40.7 →40.2	50 49.5→50.3 →47.1	55 53.5	2→9	1244A	8	Baro Ramp, H=3 No film last 2/3?
23	165	4	30 35.6→37.5	45 42→45.0	45 45.5→43.9	55 55.2→53.5	3→10	1245A	8 ✗	Jovian Ramp Film for 5 min.
24	157	2	25 26→31.1	40 40	25 26.8→32.4	40 42.4→40.7	2→10		8	Solar Ramp No film
25	158	2	25 26.6→30.8	40 40	25 27.5→31.1	40 42.4	2→10	1335A	9	Solar Ramp Film for 20 min?
26	173	6	25 25.6→31.1	40 40	25 26.3→32.7	40 42.4→40.7	1→9		8	Solar Ramp No film, Video?
27	169	4	30 37→40.2	40 40.2	50 48.6→50.3 →49.1	55 53.5→55.2	2→9	1246A	8	Baro Ramp, H=3 Film for 5 min?
28	220	16	30 38.3→39.5	40 40.3	50 47.9→50.3 →47.1→49.5	55 55.2→53.2	1→9		2	Baro Ramp, H=3 No film
29	219	128	25 25.6→27.9	40 40	25 26.3→27.9	40 42.4	2, 3, 2		1	Look for Mantle Hyst. @2 kV, No film

TABLE 3. GFFC RUNS PERFORMED ON SPACELAB - 3, 1985

Scenario Number	Rotation Period (sec)	(commanded parameters shown below) TOE (degreeC)	TIE (degreeC)	TOP (degreeC)	TIP (degreeC)	High Voltage Ramp (kV)	Comments
35	2	25	35	25	35	3.6 -> 10	6 hour Solar Ramp H = 0
40	48	25	40	25	40	5.0 -> 10	3 hour Solar Ramp H = 0
16	2	25	30	40	45	0 -> 10	3 hour "Jupiter" w/ latitudinal gradient H = 3
20	2	25	30	45	50	5 -> 10	3 hour "Jupiter" w/ latitudinal gradient H = 4
21	2	25	30	45	50	1 -> 3	3 hour "Jupiter" w/ latitudinal gradient H = 4
23	16	25	30	40	45	1 -> 3	3 hour "Jupiter" w/ latitudinal gradient H = 3
9	2	25	35	25	35	0 -> 1.6	5 hour solar with dye injection, H = 0
5	250	25	35	25	35	0 -> 1.0	5 hour basic instability run, H = 0
12	2	30	25	45	40	0 -> 10	3 hour ocean, stably stratified
13	2	30	25	45	40	0 -> 2	3 hour ocean, stably stratified
60	20	38	35	38	35	5.44 fixed	20 minute spin up run, stably stratified H = 0
43	2	30	45	30	45	5 - 6 - 5 - 6	voltage up down up jumps, H = 0
44	2	30	40	30	40	2 - 3 - 2 - 3	voltage up down up jumps, H = 0
24	16	25	35	35	45	5 -> 10	3 hour "Jupiter" w/ latitudinal gradient H = 1
25	16	25	35	35	45	1 -> 3	3 hour "Jupiter" w/ latitudinal gradient H = 1
41	48	25	35	35	45	5 -> 10	3 hour "Jupiter" w/ latitudinal gradient H = 1
42	48	25	35	35	45	1 -> 3	3 hour "Jupiter" w/ latitudinal gradient H = 1
18	2	25	35	35	45	5 -> 10	3 hour "Jupiter" w/ latitudinal gradient H = 1
22	16	25	30	40	45	5 -> 10	3 hour "Jupiter" w/ latitudinal gradient H = 3
16	2	25	30	40	45	0 -> 10	3 hour "Jupiter" w/ latitudinal gradient H = 3
17	2	25	30	40	45	0 -> 2	3 hour "Jupiter" w/ latitudinal gradient H = 3
19	2	25	35	35	45	1 -> 3	3 hour "Jupiter" w/ latitudinal gradient H = 1
20	2	25	30	45	50	5 -> 10	3 hour "Jupiter" w/ latitudinal gradient H = 4
21	2	25	30	45	50	1 -> 3	3 hour "Jupiter" w/ latitudinal gradient H = 4
34	2	25	35	25	35	1.4 -> 3.2	6 hour solar ramp, H = 0
38	16	25	35	25	35	3.6 -> 10	6 hour solar ramp, H = 0
4	20	25 -> 40	25	25 -> 40	25	0	Basic calibration, no applied voltage
5	250	25	35	25	35	0 -> 1.0	5 hour basic instability run, H = 0
46	2	25	45	25	45	5 -> 10	3 hour solar, H = 0
37	16	25	35	25	35	1.4 -> 3.2	6 hour solar, H = 0
39	48	25	40	25	40	0.48 -> 2.0	3 hour solar, H = 0

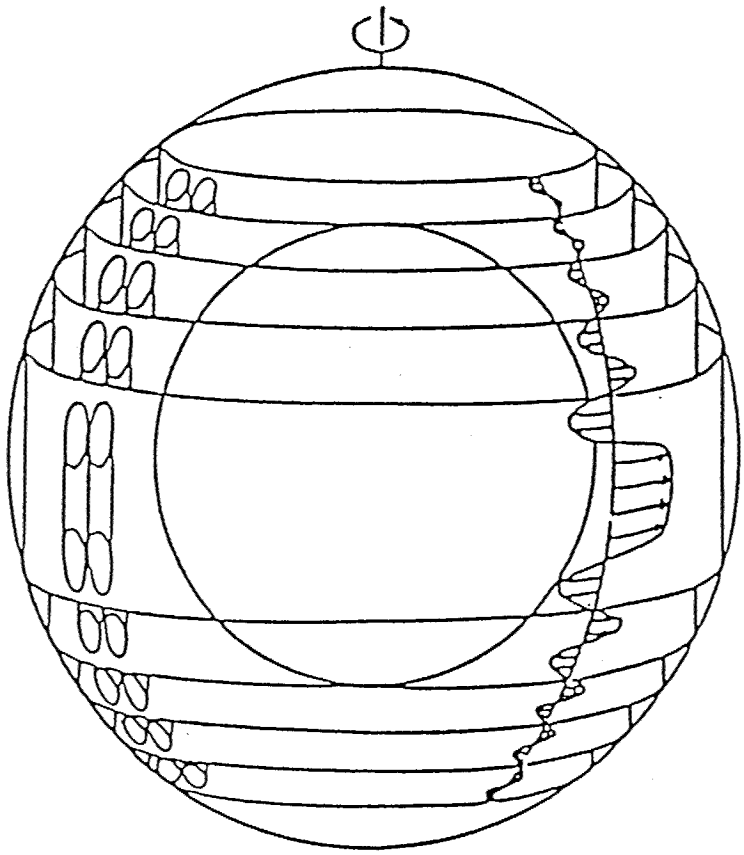

Figure 1. Nested convection cylinders in a rapidly rotating convecting liquid (after Busse, 1983)

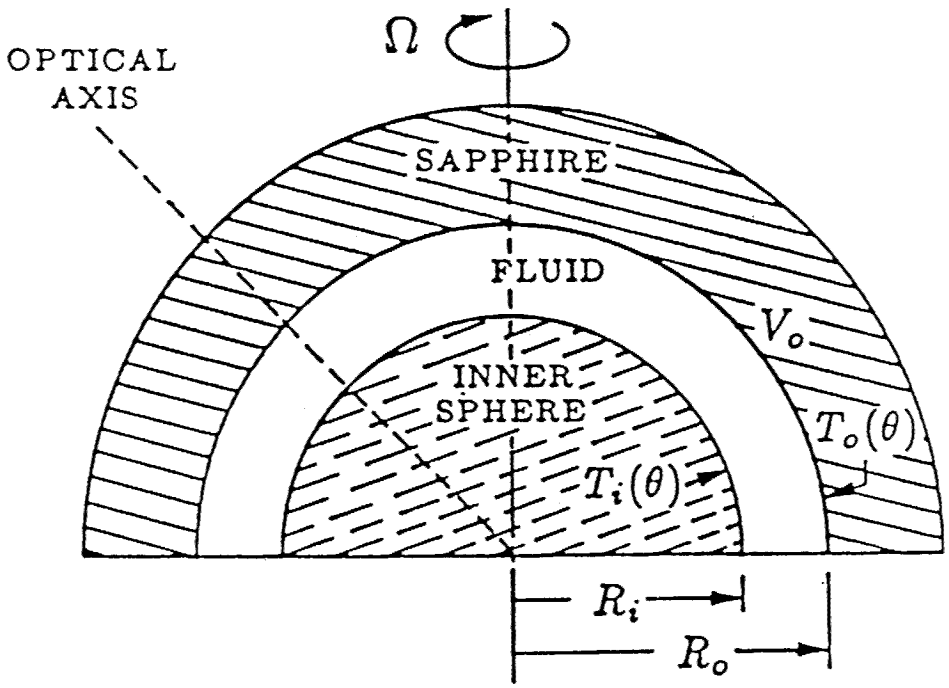

Figure 2. Schematic cross-section of the Geophysical Fluid Flow Cell. The gap contains 0.065 centistoke silicone fluid.

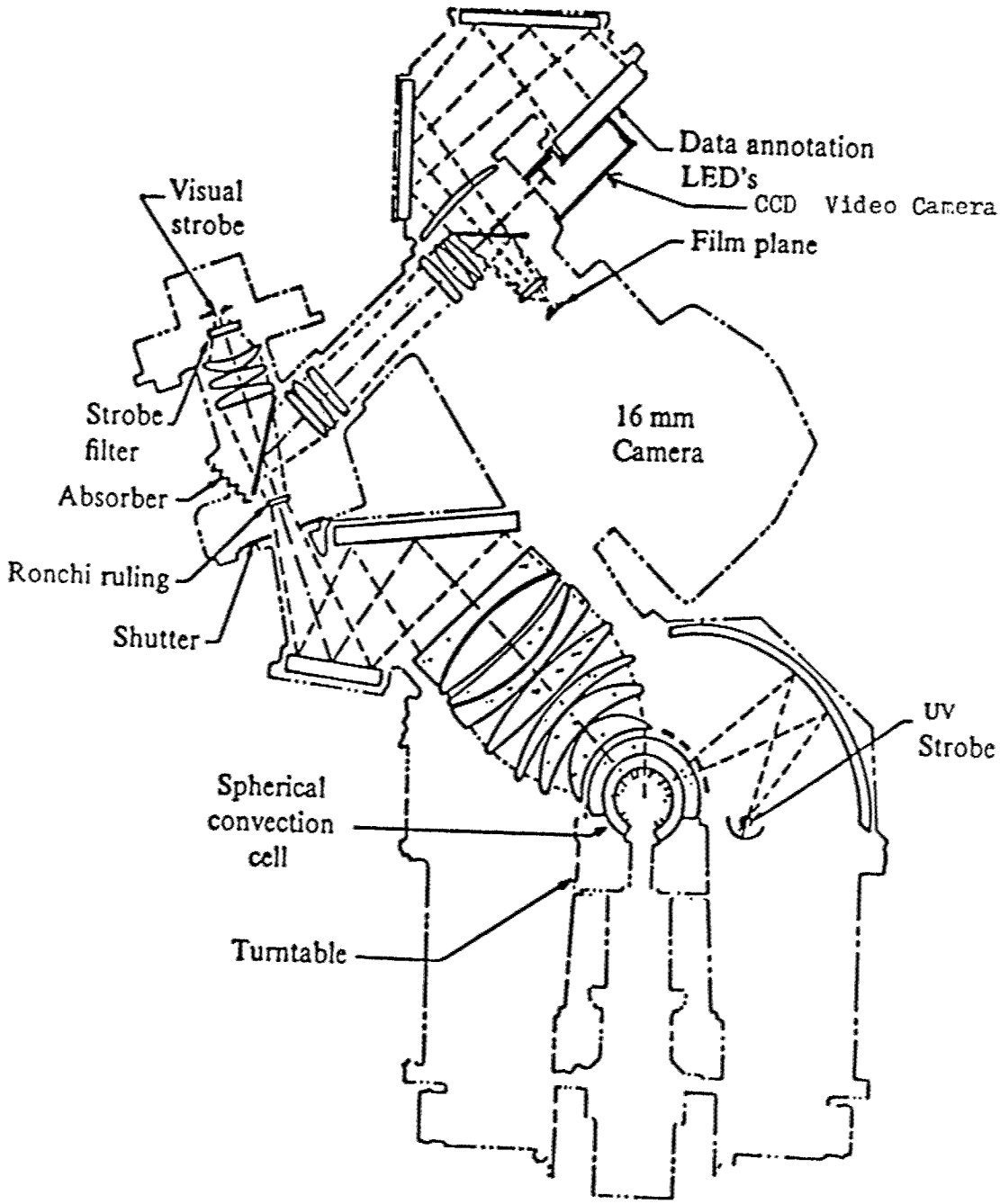

Figure 3a. Instrument cross-section. The optics provides a Schlieren visualization of convection in the spherical convection cell. A beam splitter diverts the image to both a 16mm and a video camera.

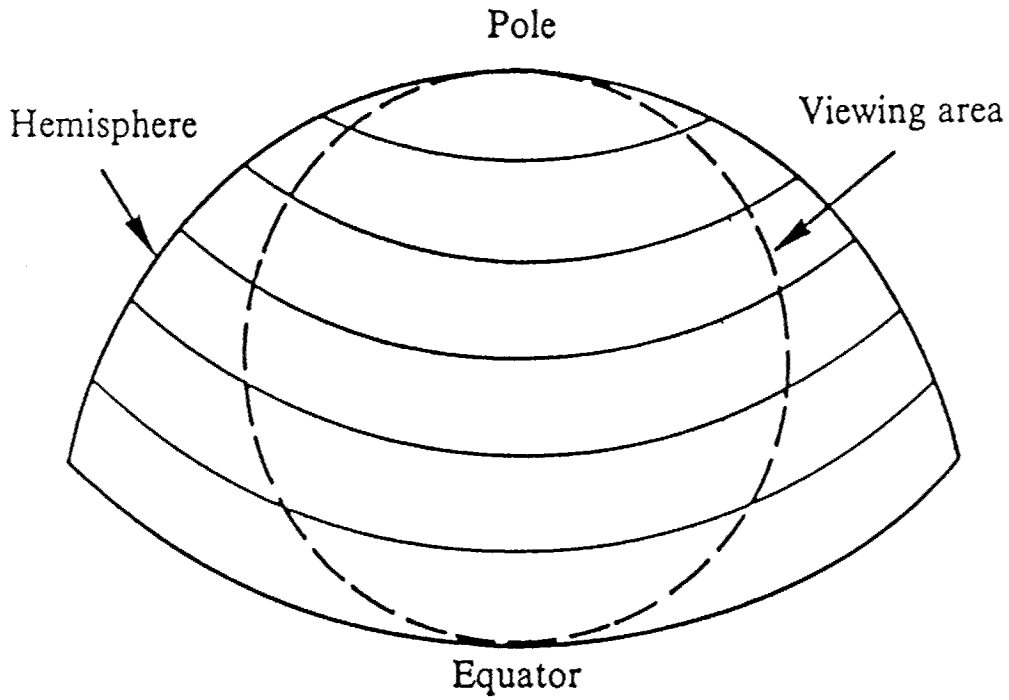

The view of the working fluid, mapped onto the sphere.

Fig. 3b. Sketch of the view of the GFFC sphere that is seen by the optical system. Much as a telescope views a planet the viewing area extends from the equator to the pole.

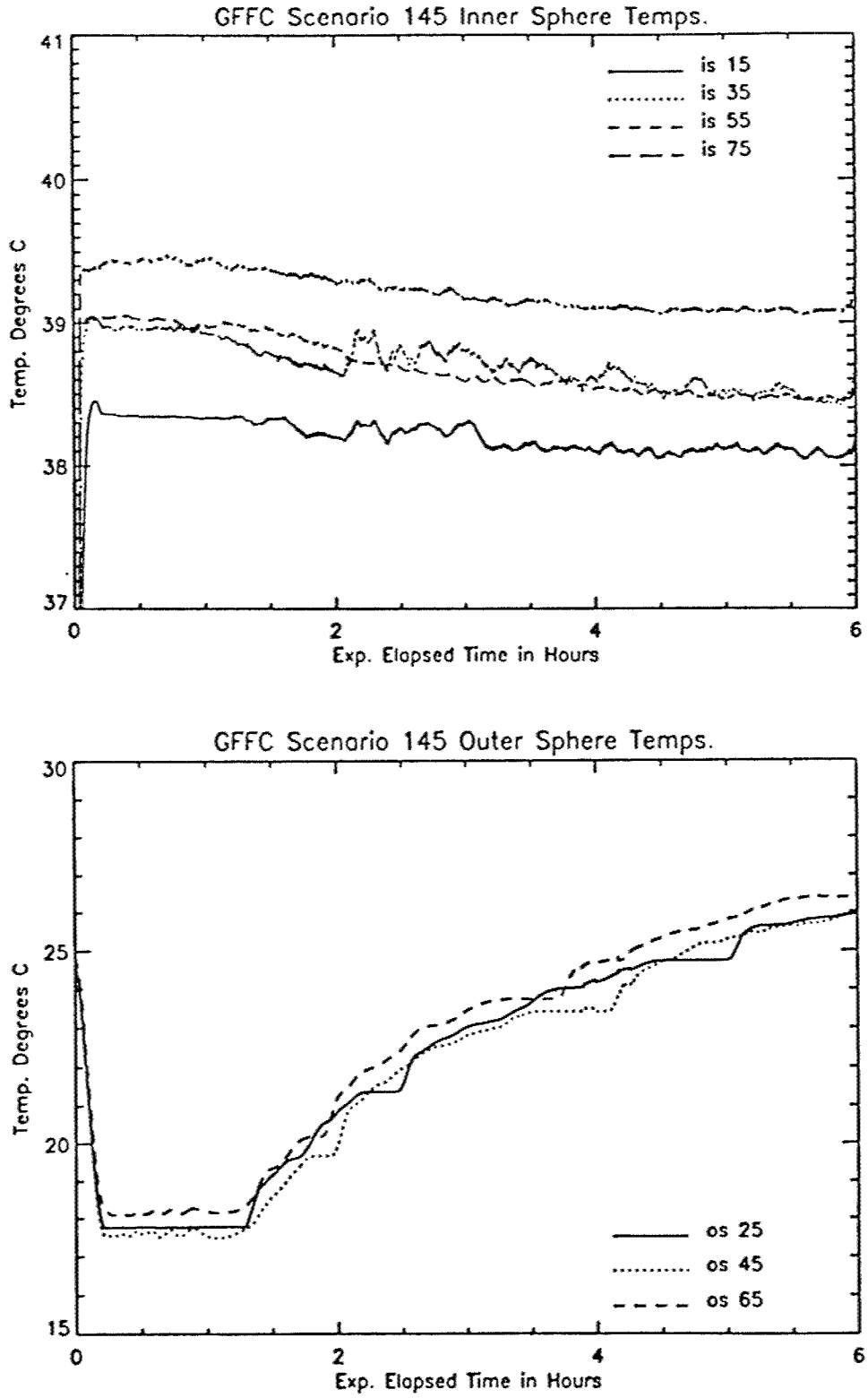

Figure 4. Thermal history at the walls for scenario 145 (4 second basic rotation period, high voltage ramping from 0 to 10 kiloVolts). The upper panel shows the inner sphere values at the latitudes shown, while the lower panel illustrates the behavior of the outer sphere at the latitudes shown.

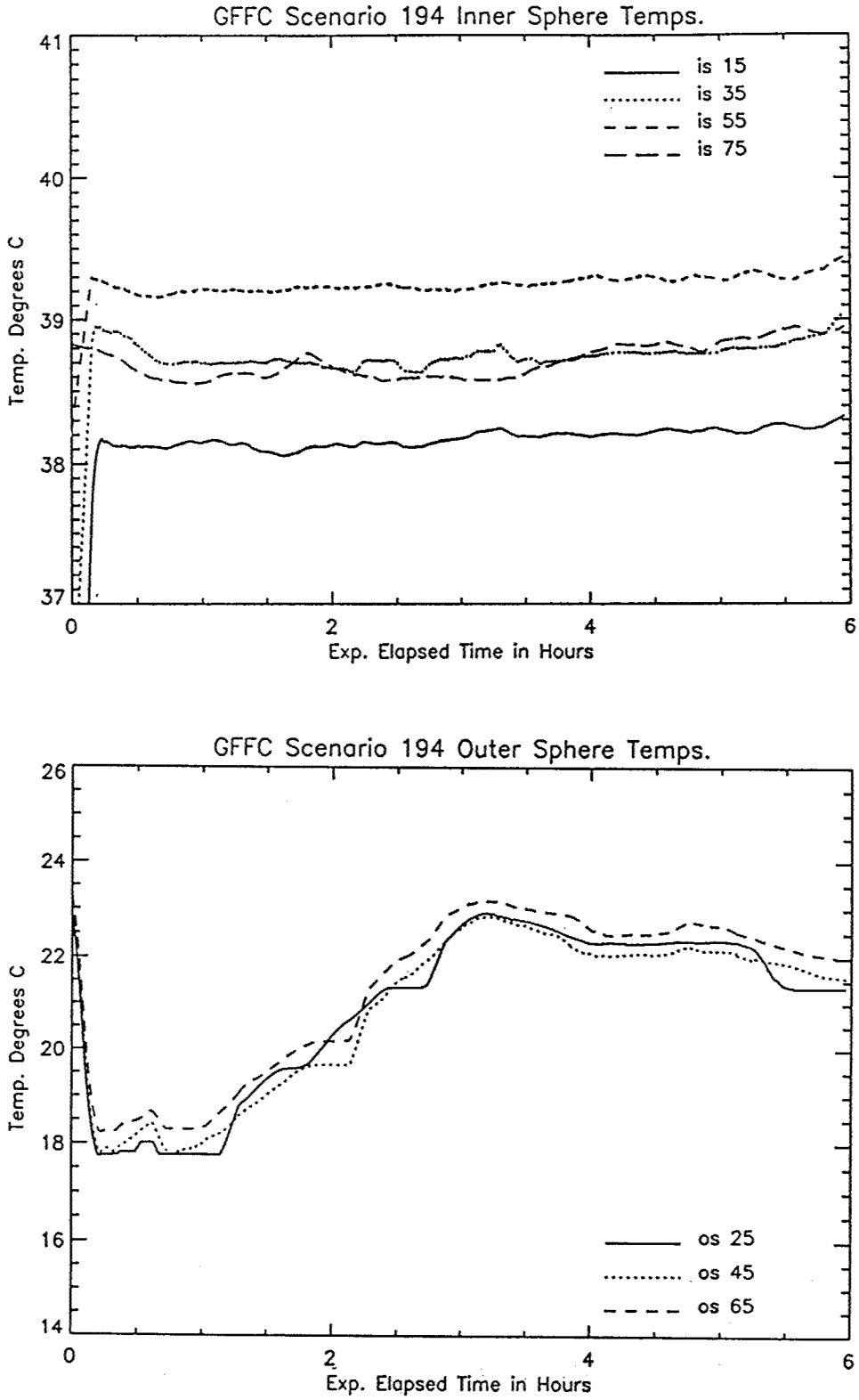

Figure 5. Thermal history at the walls for scenario 194 (48 second basic rotation period, high voltage ramping from 0 to 3 kV and back down again). The upper panel shows the inner sphere values at the latitudes shown, while the lower panel illustrates the behavior of the outer sphere at the latitudes shown.

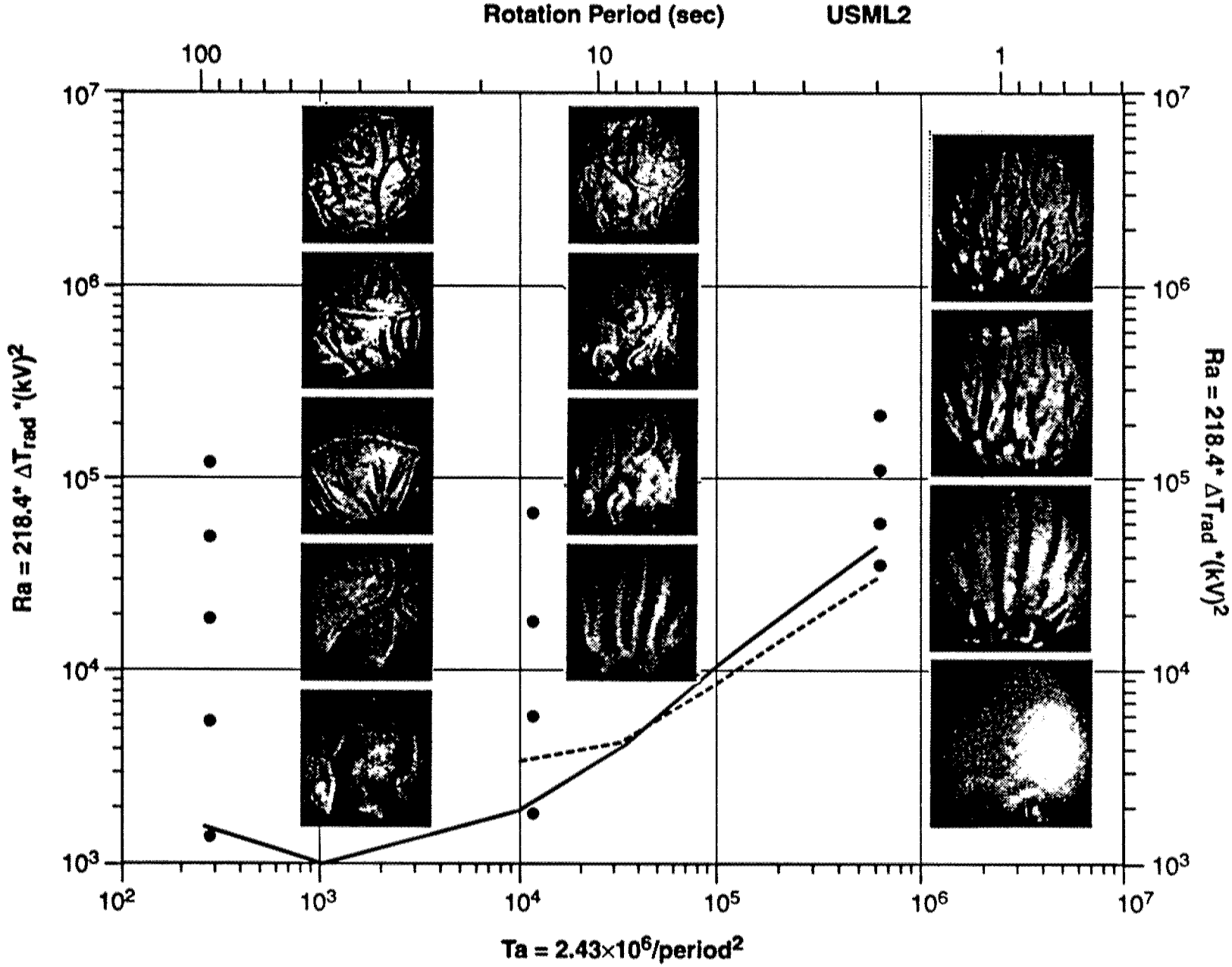

Figure 6. Regime diagram showing qualitative results for several Rayleigh number ramp up experiments with symmetric heating. Each image is a single snapshot with the south pole at the bottom and the equator at the top. The solid curve shows the onset of banana cell, the dashed the onset of polar wavy convection. Each image corresponds to the dot to its left, in vertical order.

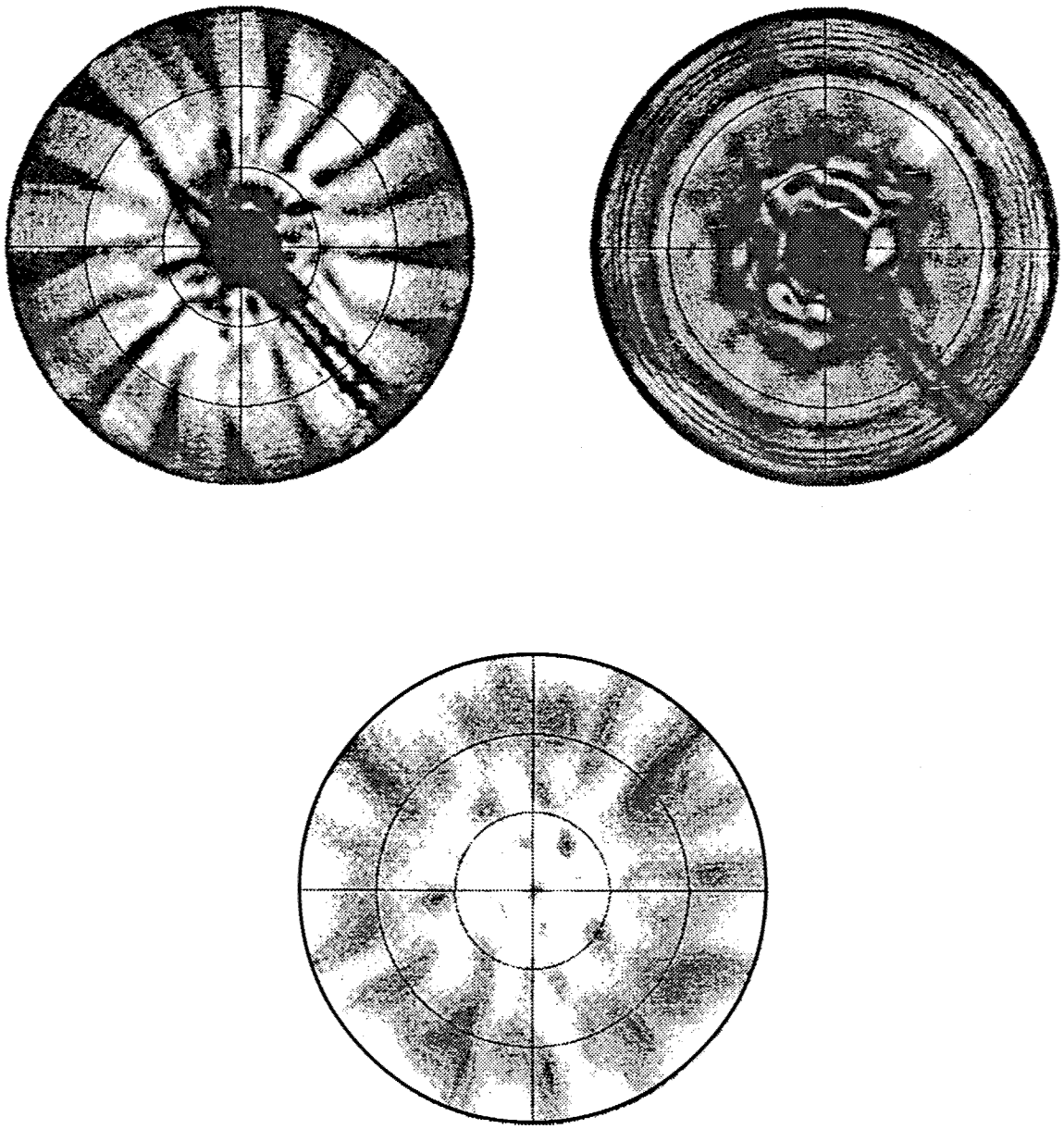

Figure 7a. Unwrapped convection planforms for scenario 145 (4 second rotation period, symmetric heating, 2.16 kilovolts). The top two panels show motions as viewed by E-W fringes (left) that are sensitive to longitudinal temperature gradients, and N-S fringes (right) that are sensitive to latitudinal gradients. The bottom panel shows radially averaged temperatures form the Miller-Leslie model. Note the general agreement on structure and equivalence of disturbance longitudinal wavenumber. In all frames the view is from pole (center) to equator (limb) with equal spacing of latitude lines.

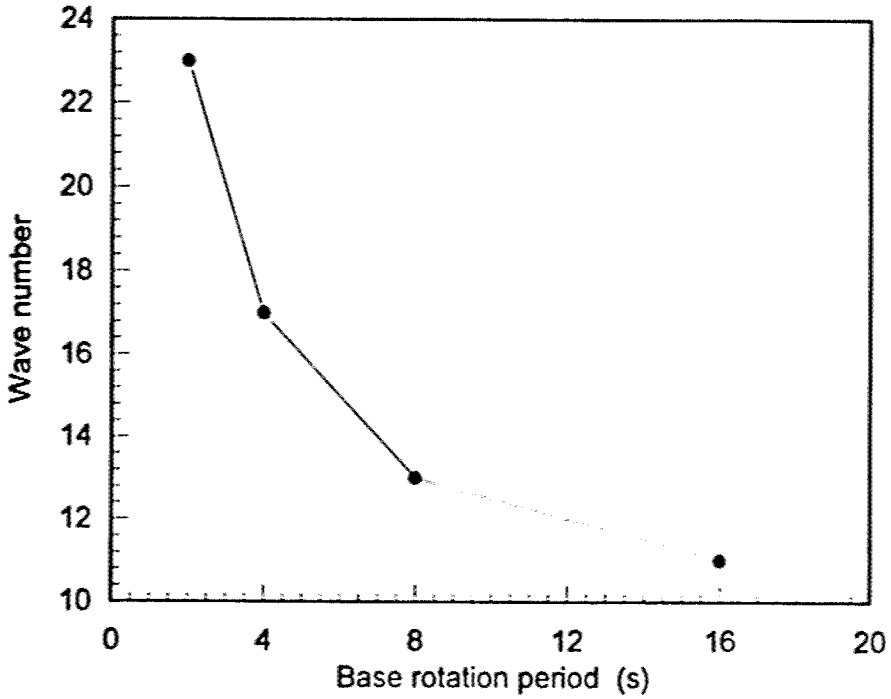

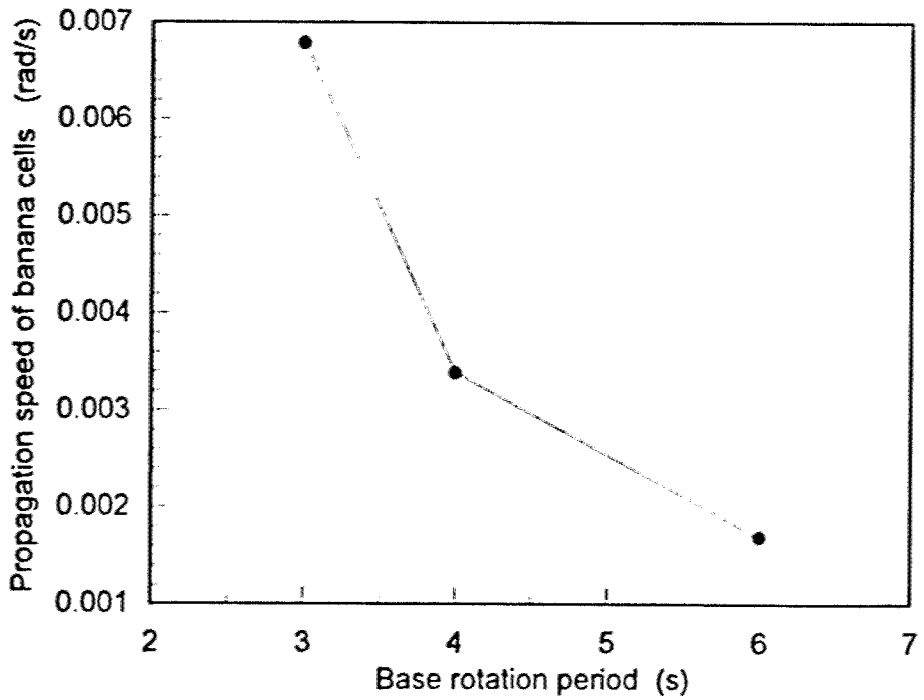

Figure 7b. Propagation characteristics near onset for spherically symmetric heating and the basic rotation rates (periods) as shown. Top panel shows the near-critical azimuthal wavenumber. Bottom panel shows near-critical (prograde) wave propagation speed in radians per second.

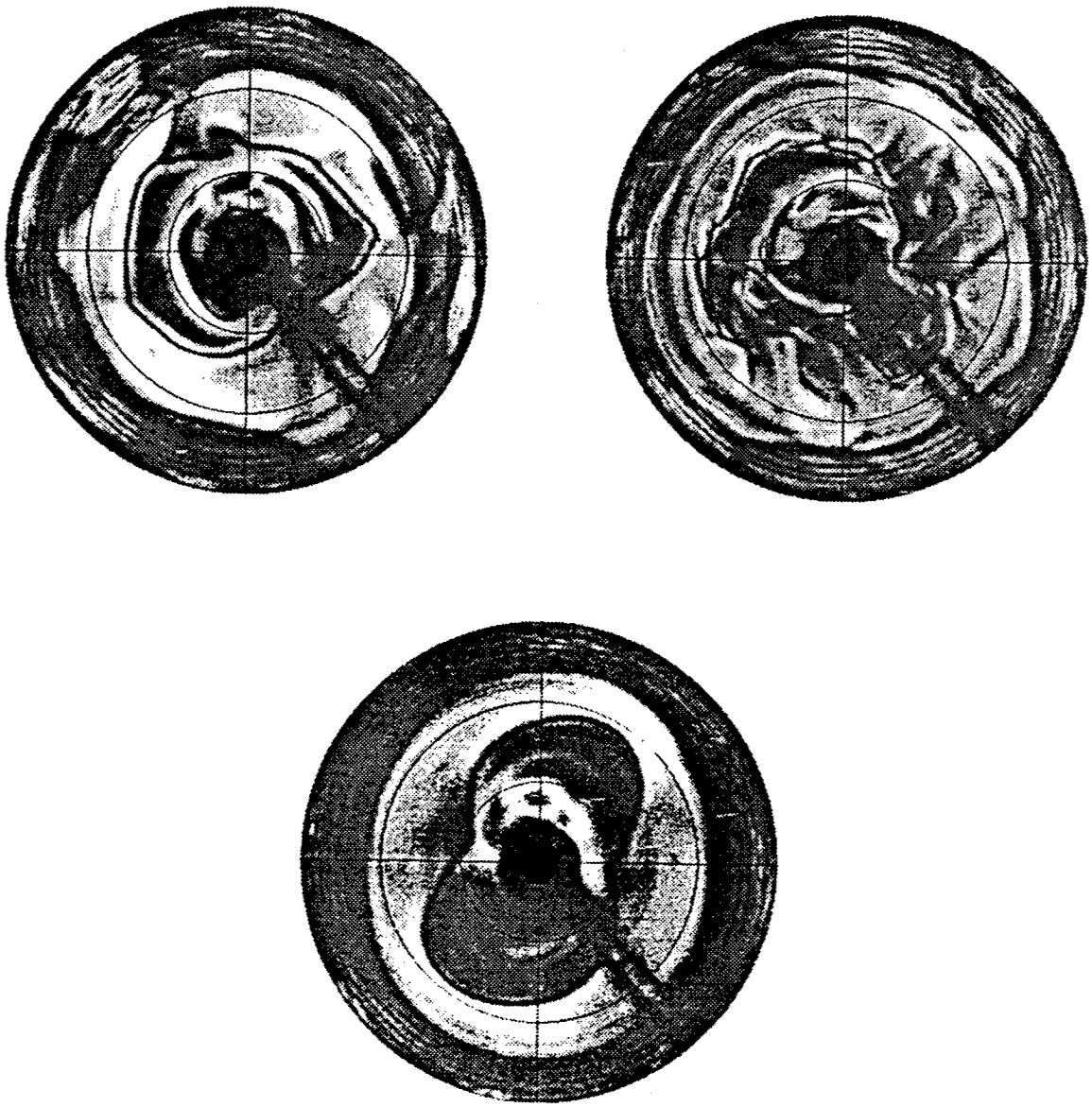

Figure 8. Unwrapped views (as in figure 7) of scenario 194 (48 second rotation, symmetric heating). N-S fringes 9 sensitive longitudinal thermal gradients) for values of voltage shown (1.46, 3.16, 1.5 kV). The first two images (top left and right) are during the first three hour ramp up, while the bottom image (the only stable pattern) is at about hour five. The first image is during the first voltage hold period, the second during the ramp up to 3.5 kV, and the third is just after the end of the second voltage hold period.

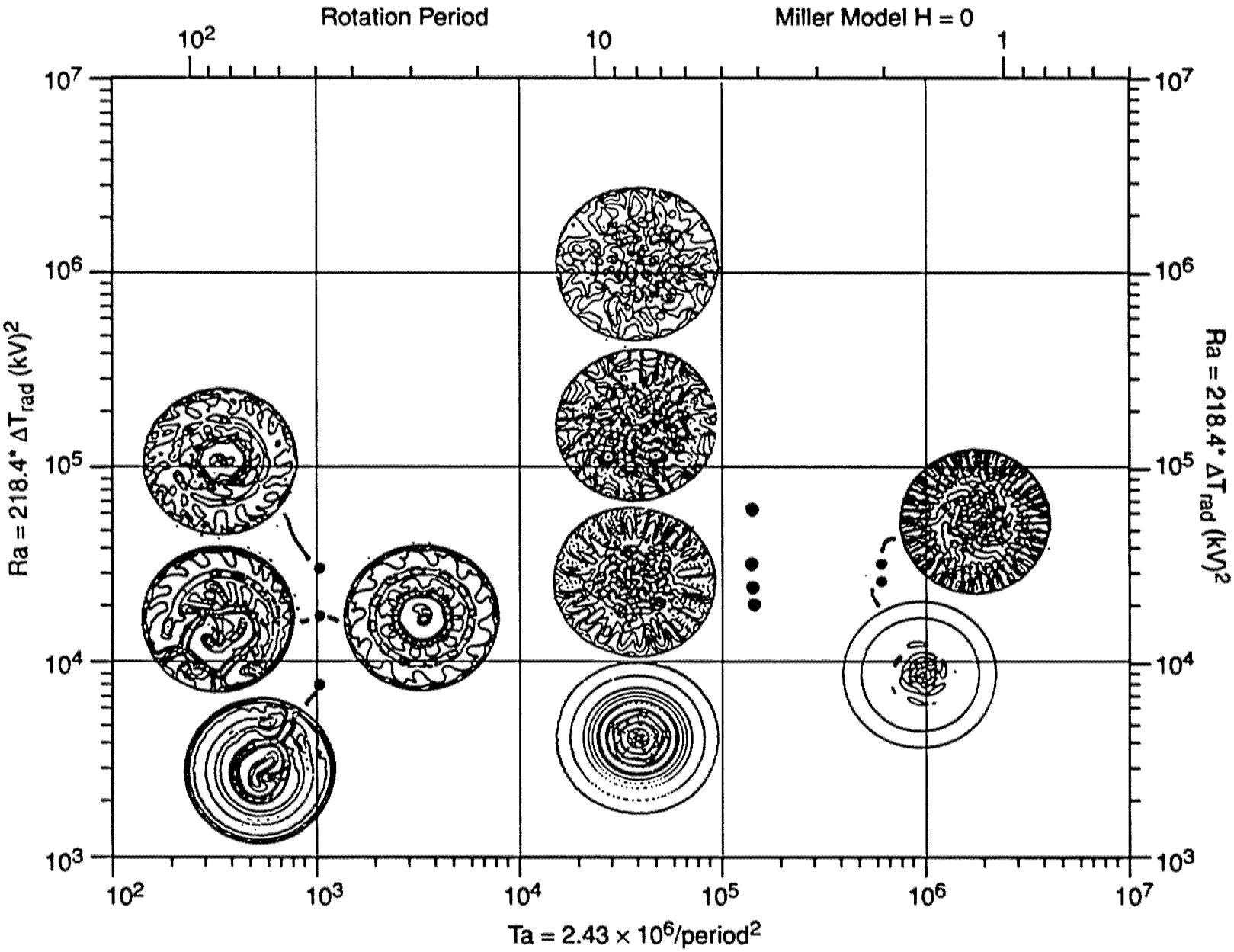

Figure 9. Regime diagram showing computed planforms in the Miller-Leslie model (Fourier decompostion in longitude, grid points in the meridional plane). Boundary conditions, r-dependent gravity, centrifugal acceleration, and geometry as in GFFC.

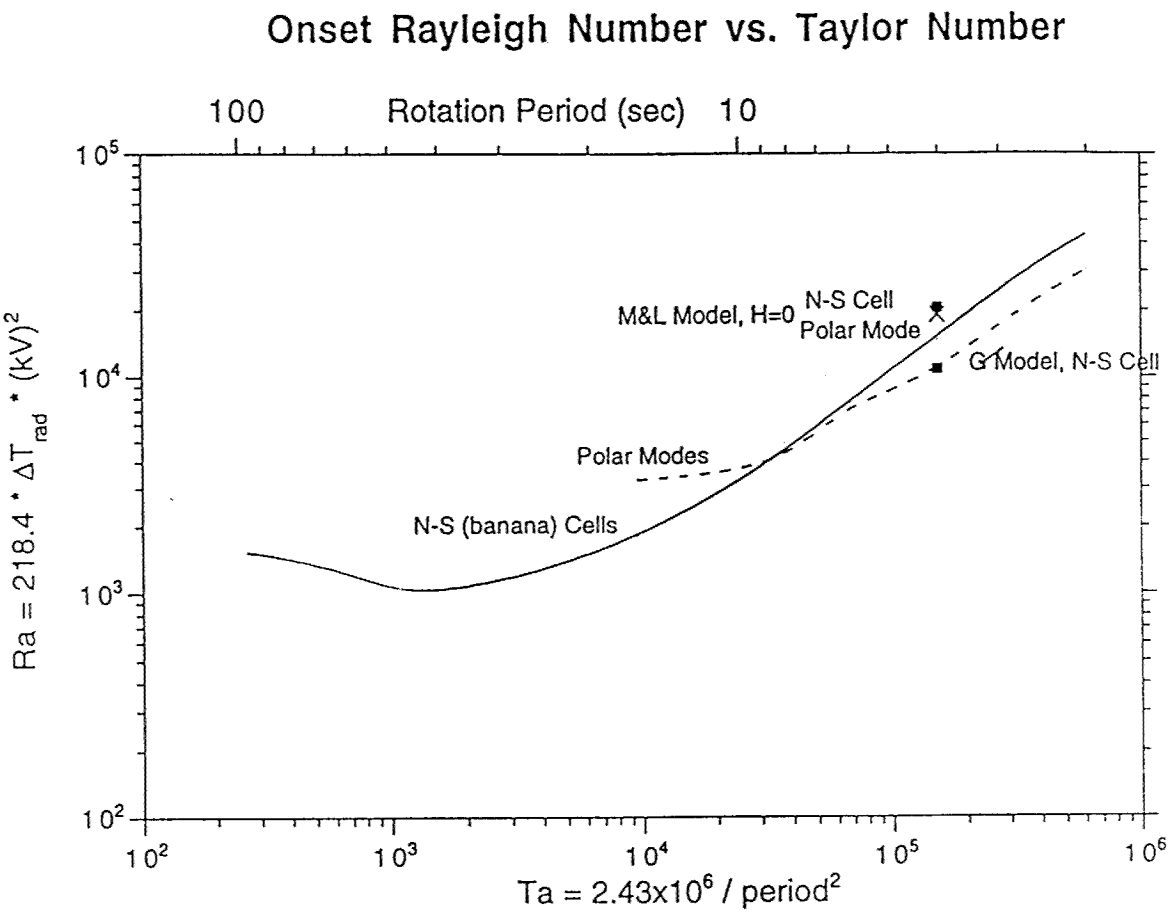

Figure 10. Critical curves from the GFFC experiments. Polar modes become the most unstable for Taylor numbers in excess of about 20,000. The results from computational simulations are shown as points on the figure.

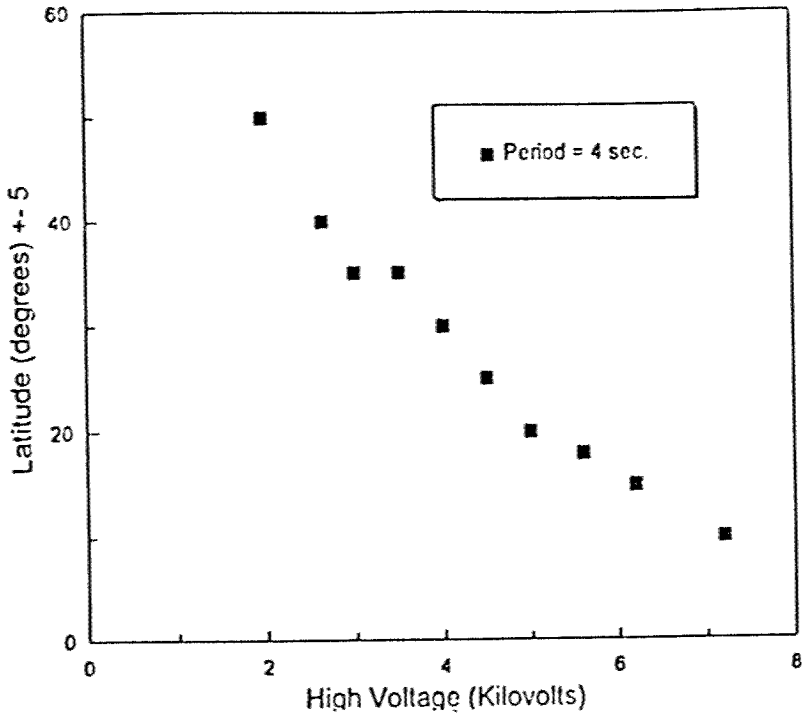

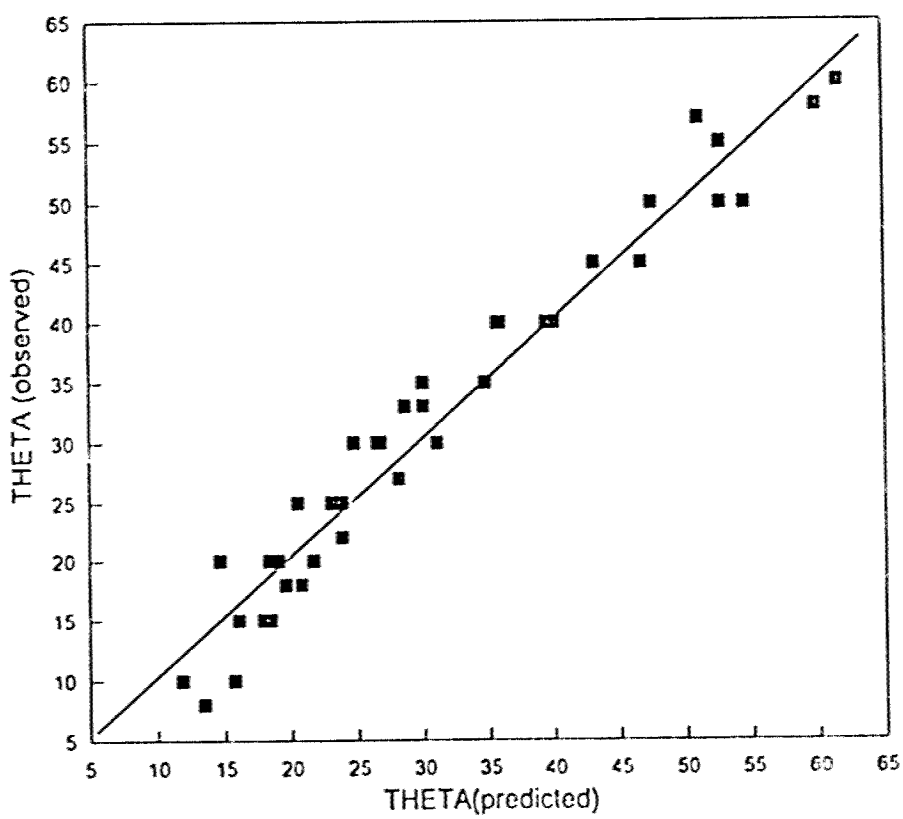

Figure 11. top) Transition latitudes vs. voltage for 4 second rotation

bottom) The model relation when rotation period and voltage are assumed to have the same exponent is shown. This is $\sin(\theta_{predicted}) = 270\ (\tau V)^{-.85}$, with an average error of 11% A similar fit to the relation $\sin(\theta_{predicted}) = 380\ (\tau V)^{-1}$ is nearly indistinguishable, with an average error of 12%. However the scaling in (4) can only collapse the data to within 35% of the identity line.

APPENDIX 1

DATA REDUCTION SYSTEM

TEMPERATURE AND HIGH VOLTAGE RECORDS FROM USML-2 MISSION 16mm FILMS

GFFC Data Reduction

The process of extracting data from the GFFC experiment film, and producing information easily read and viewed using a PC, required three networked computers, a state of the art high resolution video camera, 2 video capture boards, a laser videodisc recorder, a computer controlled film projector, along with device control and image analysis software developed at the University of Colorado.

USML2 and Spacelab 3 film of the Geophysical Fluid Flow Cell was converted to video on a modified stop action movie projector. Computer control of the movie projector allowed for accurate frame positioning and illumination level control of the experiment film to be viewed with a Kodak Megaplus model 4.2 black and white video camera. The Kodak video camera is state of the art equipment with a 2K X 2K square pixel aspect ratio and an anlog ouput signal with ten bits (1024 gray levels) of dynamic range. Film illumination control was required because of intensity variations between picture type 1 and picture type 2 images. Capture of the very high resolution video signal from the Kodak video camera was achieved with a Coreco Oculus 500 video frame grabber for PC compatible systems. The video capture card served two purposes. First the card was used to reformat the video signal to an RS-170 three component (RGB) video signal compatible with a Sony laser videodisc recorder (LVR-3000N). Each image of the 135,000 plus film frames was stored on laser videodisc. Second the film annotation for the USML2 mission was digitized and stored on computer hard disk for processing later. All elements of image acquisition, projector control ,data compression , and data storage were controlled by a C program written just for the GFFC image recording system.

After digitizing, compressing ,and storing USML2 annotation to computer hard disk the image files were passed via an Ethernet connection to an SGI Infinite Reality Power Onyx for conversion from image to ASCII data. Even with compression ratios of 10:1, the image data alone occupied over 10 gigabytes of disk space. To convert the experiment image annotation data to a more readable ASCII format, a program was developed using the IDL graphics language. This language was selected for it ease of use with image data. Annotation image quality variations required a program that would adapt to light level changes, image shifts, distortion, background noise, and misbehaving experiment LEDs. The interactive nature of the IDL programming environment made it easy to test program modules for proper operation. This reduced program development time and increase our confidence in accurate character recognition.

Annotation data came in two formats. Seven segment LED numeric characters were recognized by determining the on/off state of the segments. This proved to be faster, more adaptive, and easier than matching the numeric characters to templates (0 to 9). Dot Matrix data also was deciphered in a similar manner by checking the on/off state of the LED's and converting the binary data to an ASCII floating point value. Difficulties in the image recognition process occurred because of image variations across a frame, from frame to frame, and from scenario to scenario. Unfortunately the program was not always able to recognize the annotation. For this reason, the output data file contains an error code which indicates the confidence of the data recognition.

The complete and calibrated data set for the USML2 mission was converted from 10 gigabytes of compressed image data to approximate 10 megabytes of ASCII data. In addition to converting the image files to ASCII format, the IDL program also corrected the data using post flight calibration curves. The curves were developed by placing the experiment apparatus in a temperature controlled chamber and recording measured thermistor sensor outputs vs. actual values for the range of temperatures the experiment was operated at during the USML2 mission. Similar calibration curves were produced for the hemisphere voltage and turntable rotation period by comparing measured or command values to actual values.

In order to make viewing of the GFFC experiment images easy and accessible to anyone with a PC, the images were converted from laser videodisc to computer readable Video for Windows format. Using a Miro video DC30 capture card the GFFC experiment images on laser videodisc were digitized and written in the Motion Jpeg file format. Because this format is hardware specific, the Motion Jpeg scenario movie files were converted again to a more standard Video for Windows format using Adobe

Premiere 4.0. In addition, Adobe Premiere was used to add titles and remove the unwanted picture type 3 images from Spacelab 3 data. The 320 X 240 X 16bit .AVI movie files produced were compressed using the 'CRAM' compressor, resulting in a data set from both USML2 and Spacelab 3, which could be fit on six compact disks . Also included with the image data is the ASCII experiment annotation data set. Using the windows base aviplay.exe program both the scenario images and calibrated experiment parameter data can be viewed simultaneously.

GFFC Data Reduction Path

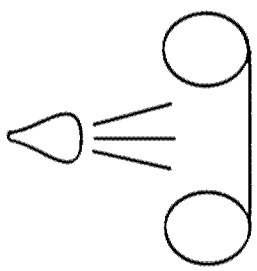

Stop Motion GFFC
Film Projector

Kodak MegaPlus
Video Camera

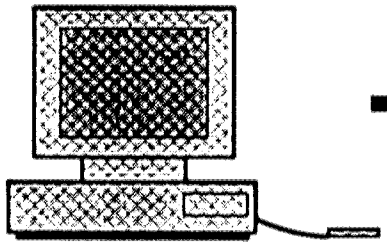

PC with Coreco
Video Frame Grabber

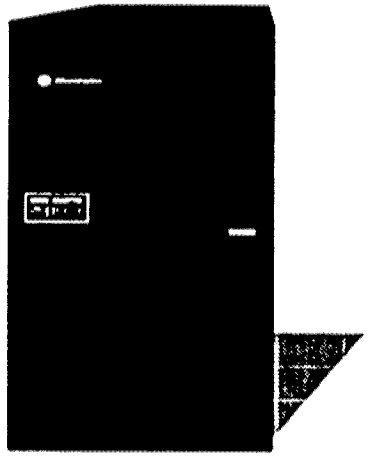

SGI Power Onyx

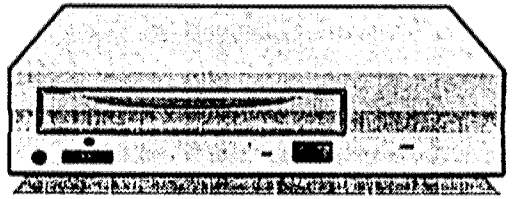

Sony Laser Videodisc Recorder

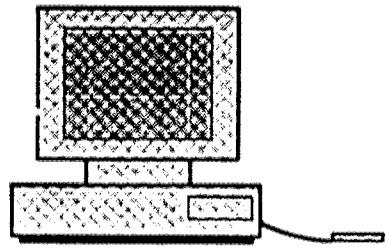

PC with Miro Video
Capture Card

GFFC Video Recording of 16mm Film Video Configuration and Data Nomenclature

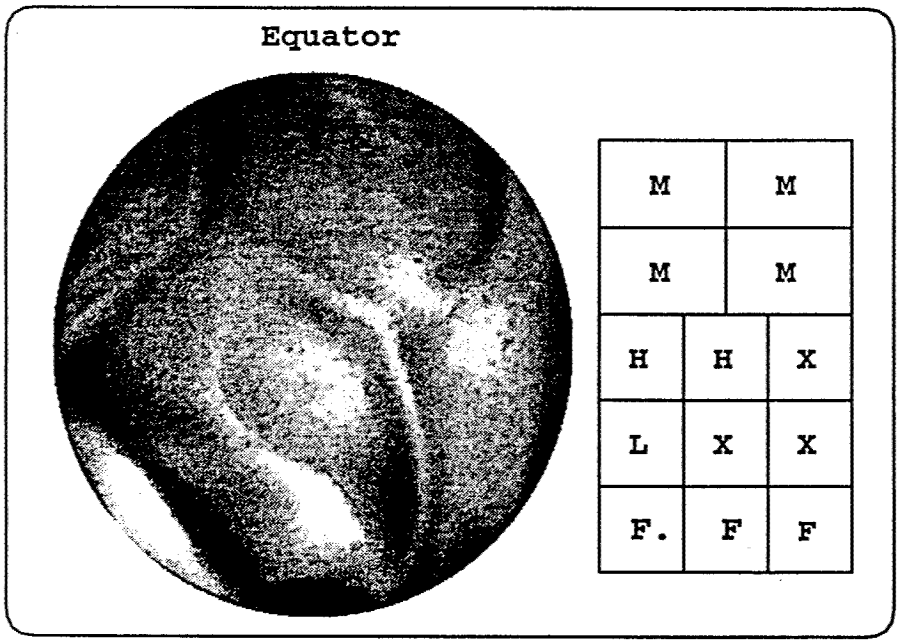

M = 5x7 LED Matrix Display

H = Scenario Number

L = Picture Type

F = High Voltage KV

X = Incomplete Data

Video Monitor View of Experiment and Annotation

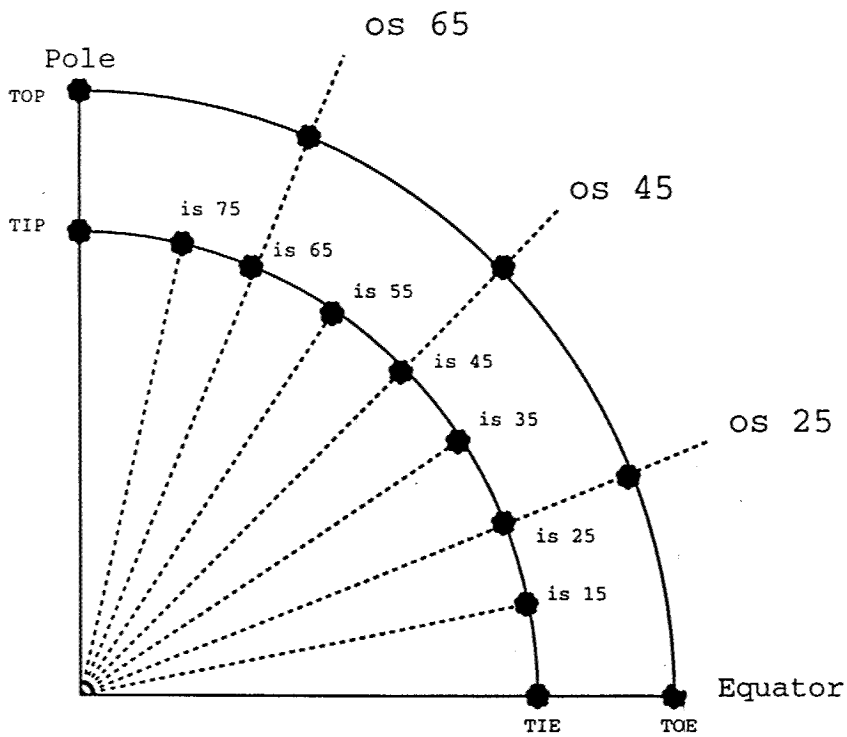

IS 15 = Inner Hemisphere 15 degrees
IS 25 = " " 25 degrees
IS 35 = " " 35 degrees
IS 45 = " " 45 degrees
IS 55 = " " 55 degrees
IS 65 = " " 65 degrees
IS 75 = " " 75 degrees
OS 25 = Outer Hemisphere 25 degrees
OS 45 = " " 45 degrees
OS 65 = " " 65 degrees
TIP = Temp. Inner Pole
TOP = Temp. Outer Pole
TIE = Temp. Inner Equator
TOE = Temp. Outer Equator

Thermistor Positions on Hemispherical Shells

DATA ANNOTATION FORMAT

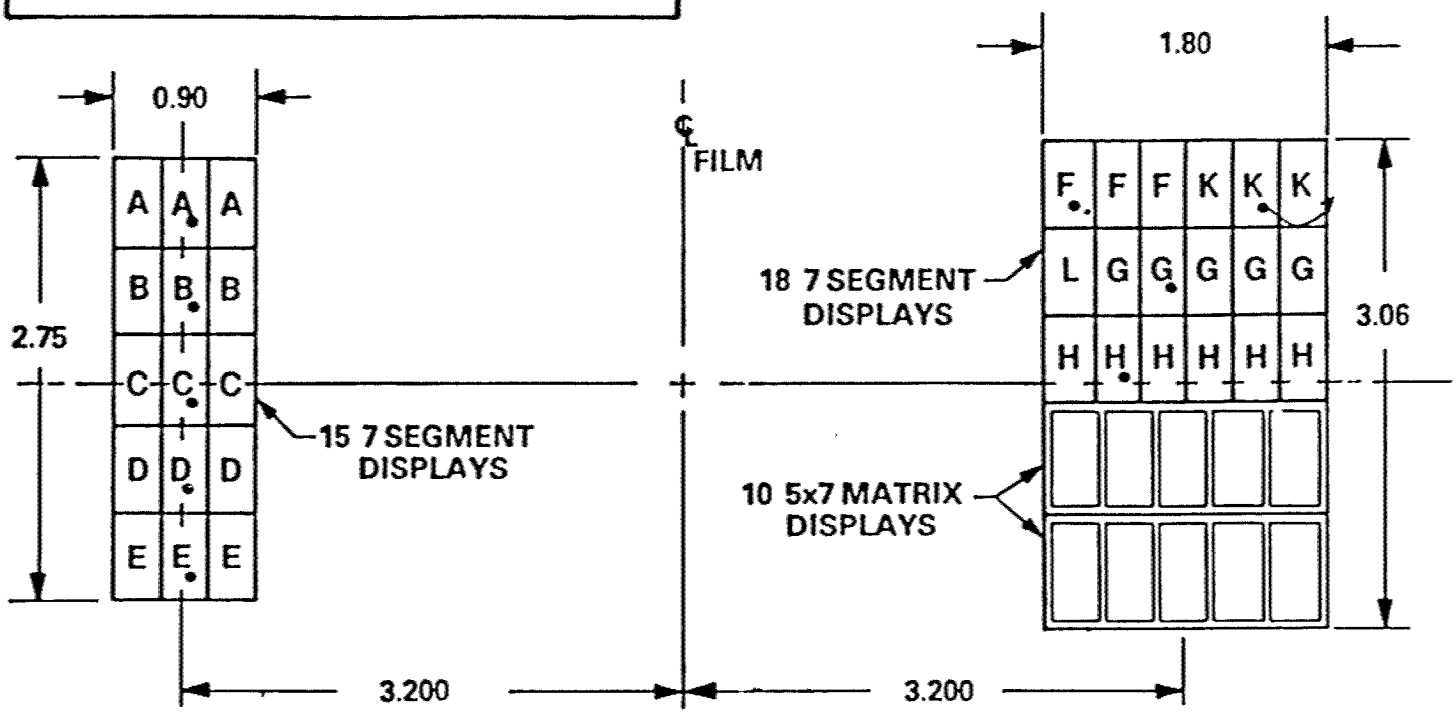

A = Heat Flux, Watts
B = T_{ie}, °C
C = T_{ip}, °C
D = T_{oe}, °C
E = T_{op}, °C
F = HV, KVolts
G = Time, Min. Sec
H = Scenario Frame No.
K = Turntable Rotation Period, Sec
L = Picture Type

GFFC Data Formats

- **Files in /data directories**

Data is in ASCII format and is readable using most word processors (e.g. Notepad).

IDL format descriptor used to write the data
format = I4 TR3 15(F5.2,TR2) I3 TR4 F5.3

Format description:
Four character integer, three spaces, fifteen floating point values with two spaces separating each value (Each number is five characters wide including the decimal point, and two characters follow the decimal point), three character integer, four spaces, five character floating point value with three characters following the decimal point.

All files in /data directories contain 120 lines of data.

Column labels for data file
FRAME #, TOP, TOE, TIP, TIE, HV, IS15, IS25, IS35, IS45, IS55, IS65, IS75, OS25, OS45, OS65, RPRD, ETIME

- **Files in /usml2 directory on disk 1**

Data is in ASCII format and is readable using a word processor capable of loading large documents (e.g. Word).

IDL format descriptor used to write the data
format = I4 TR3 15(F5.2,TR2) I3 TR4 I1

Format description:
Four character integer, three spaces, fifteen floating point values with two spaces separating each value (Each number is five characters wide including the decimal point, and two characters follow the decimal point), three character integer, four spaces, 1 character integer.

Column labels for data file
FRAME #, TOP, TOE, TIP, TIE, HV, IS15, IS25, IS35, IS45, IS55, IS65, IS75, OS25, OS45, OS65, RPRD, ECODE

FRAME#	= USML2 film frame number (frame numbers wrap around at 9999)
TOP	= Temperature at the outer pole
TOE	= Temperature at the outer equator
TIP	= Temperature at the inner pole
TIE	= Temperature at the inner equator
IS15	= Inner Hemisphere Temperature at 15 degrees
IS25	= Inner Hemisphere Temperature at 25 degrees
IS35	= Inner Hemisphere Temperature at 35 degrees
IS45	= Inner Hemisphere Temperature at 45 degrees
IS55	= Inner Hemisphere Temperature at 55 degrees
IS65	= Inner Hemisphere Temperature at 65 degrees
IS75	= Inner Hemisphere Temperature at 75 degrees
OS25	= Outer Hemisphere Temperature at 25 degrees
OS45	= Outer Hemisphere Temperature at 45 degrees
OS65	= Outer Hemisphere Temperature at 65 degrees
RPRD	= Commanded Turntable Rotation Period in seconds
ETIME	= Experiment Elapsed Time in hours
ECODE	= Error Code (0=data OK, 1= film annotation overlap-data suspect, 3= data corrupt)

- **Files in /movies directories**

Video for Windows compatible
Frame size = 320 X 240
Depth is 16bits
Compressor "CRAM" , Microsoft Video 1[32]
Keyframe every frame

THE FOLLOWING FIGURES SHOW THERMAL AND VOLTAGE HISTORIES FOR ALL USML-2 EXPERIMENTS WITH COMPLETE 16mm FILM RECORDS

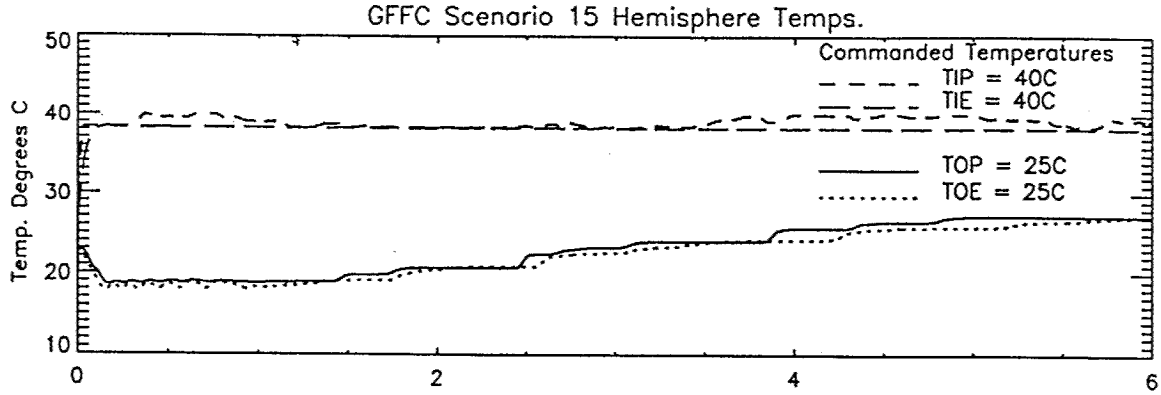

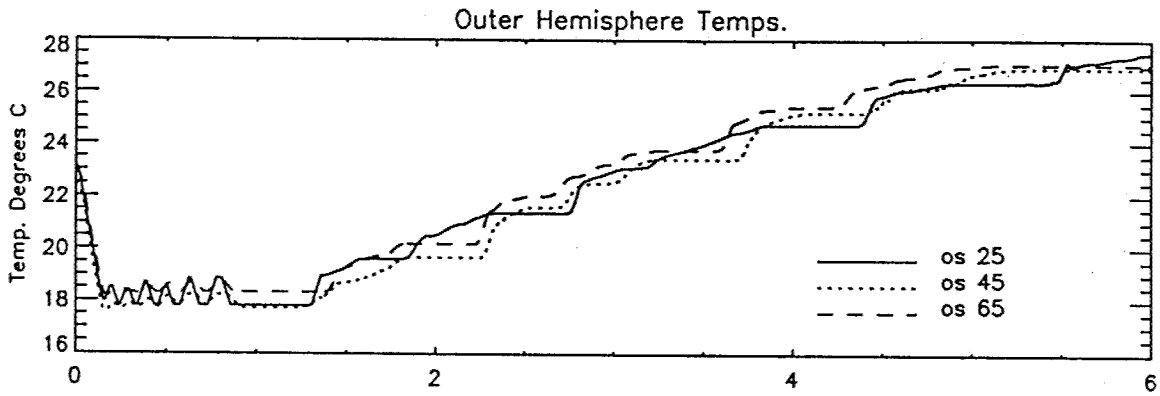

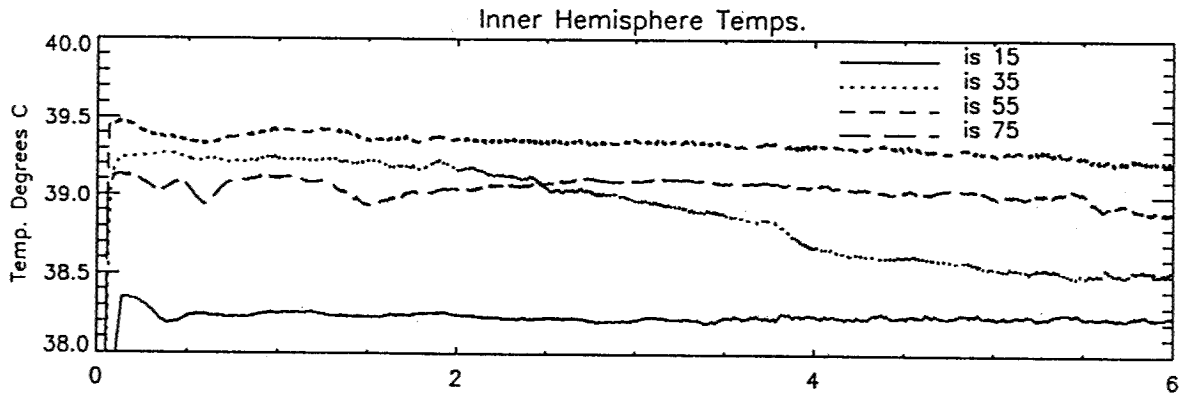

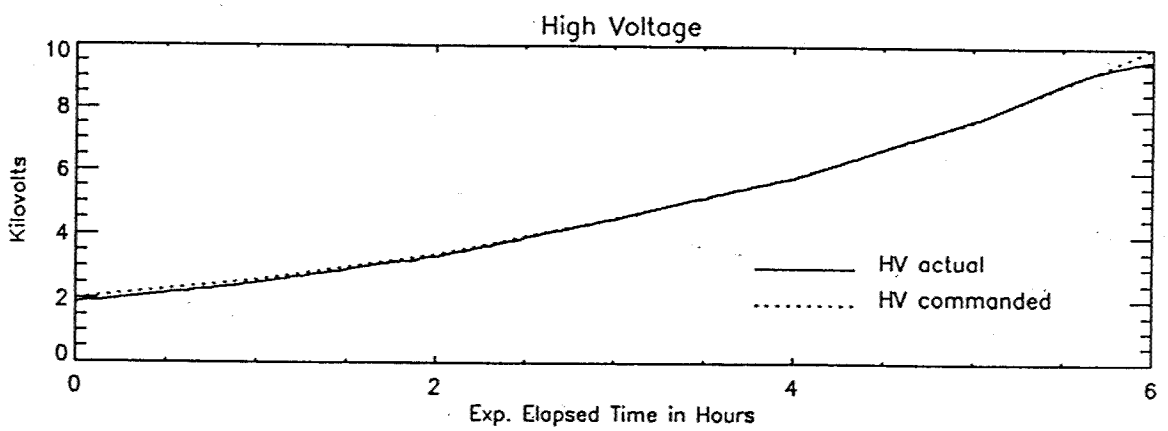

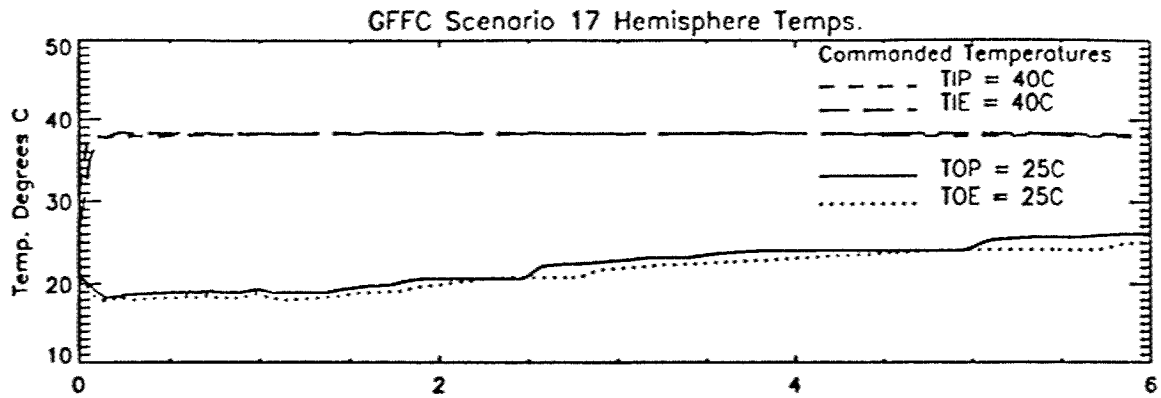
GFFC Scenorio 17 Hemisphere Temps.
Commanded Temperatures
TIP = 40C
TIE = 40C
TOP = 25C
TOE = 25C
Temp. Degrees C
50
40
30
20
10
0
2
4
6

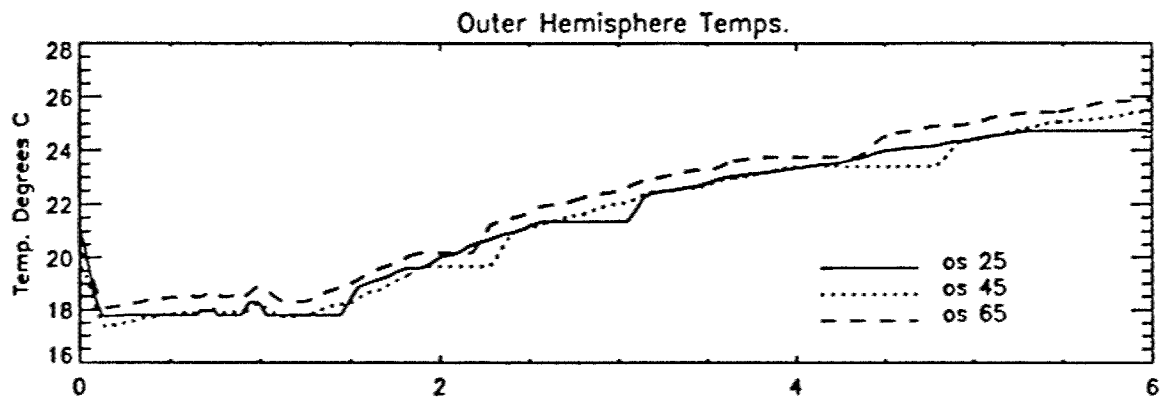
Outer Hemisphere Temps.
os 25
os 45
os 65
Temp. Degrees C
28
26
24
22
20
18
16
0
2
4
6

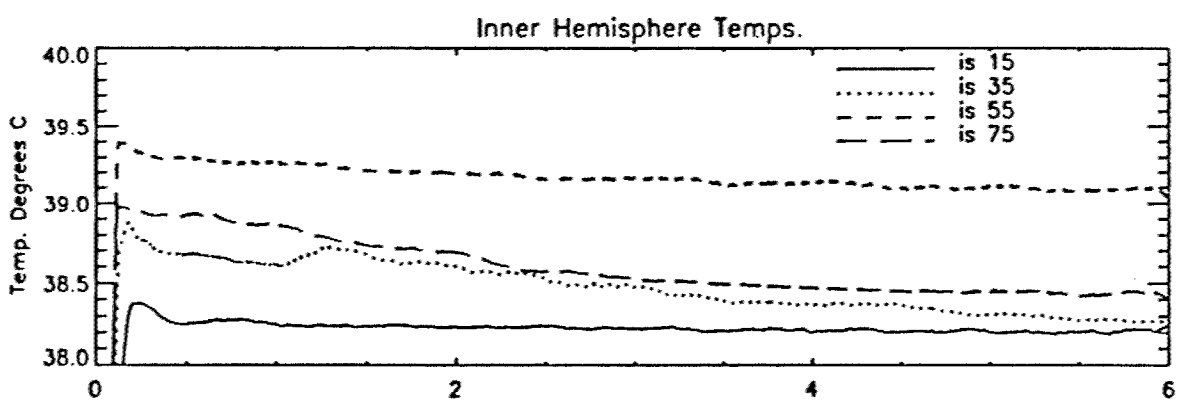
Inner Hemisphere Temps.
is 15
is 35
is 55
is 75
Temp. Degrees C
40.0
39.5
39.0
38.5
38.0
0
2
4
6

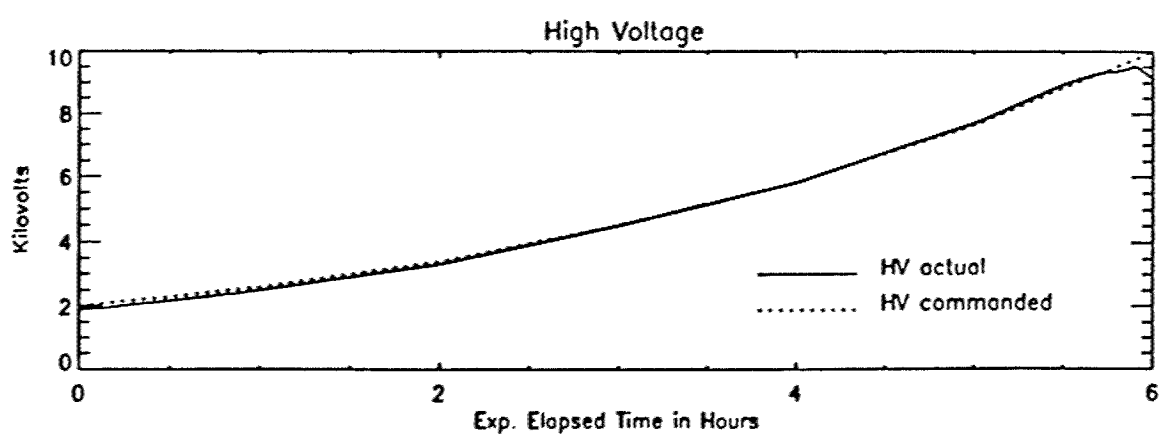
High Voltage
HV actual
HV commanded
Kilovolts
10
8
6
4
2
0
0
2
4
6
Exp. Elapsed Time in Hours

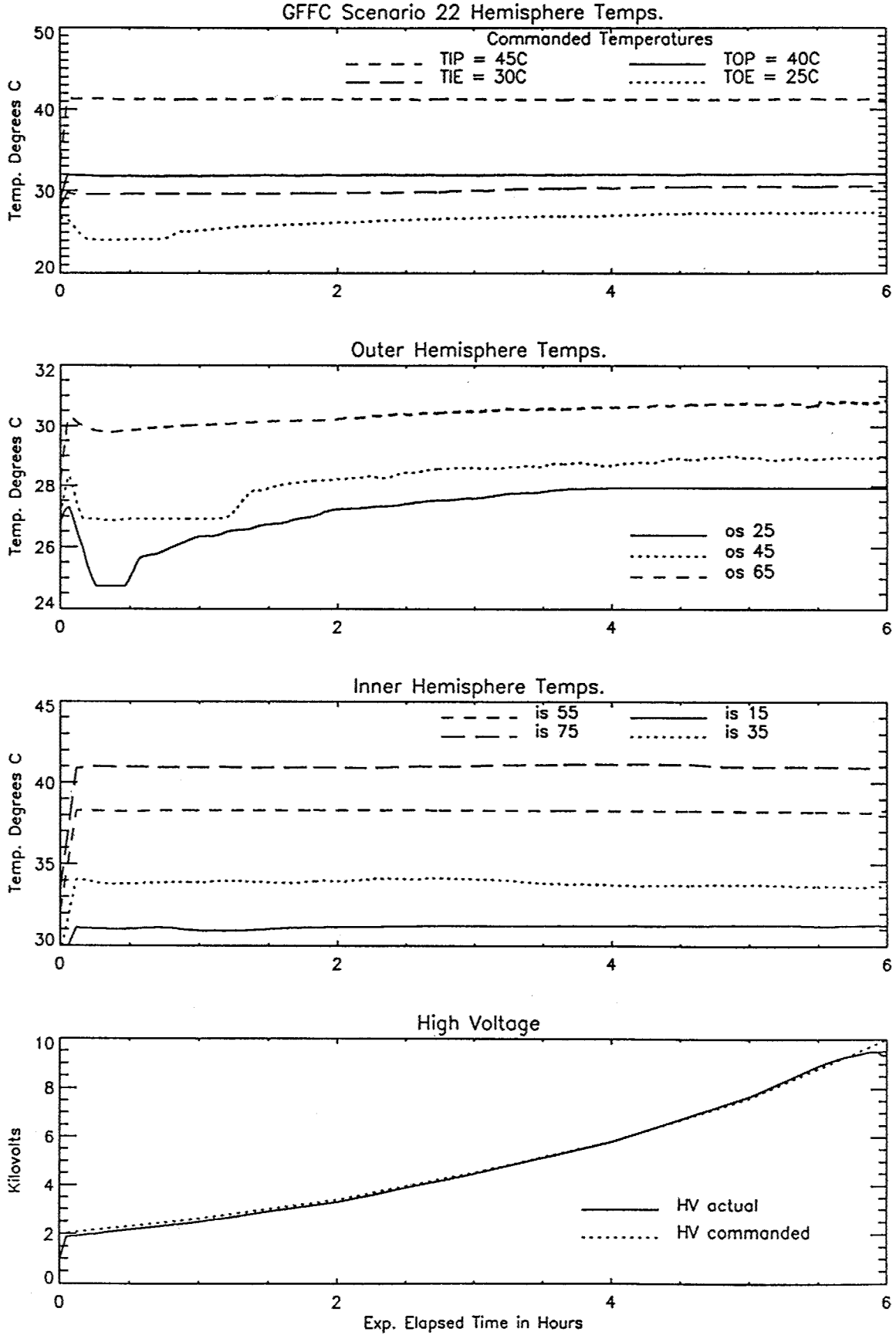
GFFC Scenario 22 Hemisphere Temps.
Commanded Temperatures
TIP = 45C
TIE = 30C
TOP = 40C
TOE = 25C
Temp. Degrees C
50
40
30
20
0
2
4
6
Outer Hemisphere Temps.
os 25
os 45
os 65
32
30
28
26
24
Inner Hemisphere Temps.
is 55
is 75
is 15
is 35
45
40
35
30
High Voltage
HV actual
HV commanded
Kilovolts
10
8
6
4
2
0
Exp. Elapsed Time in Hours

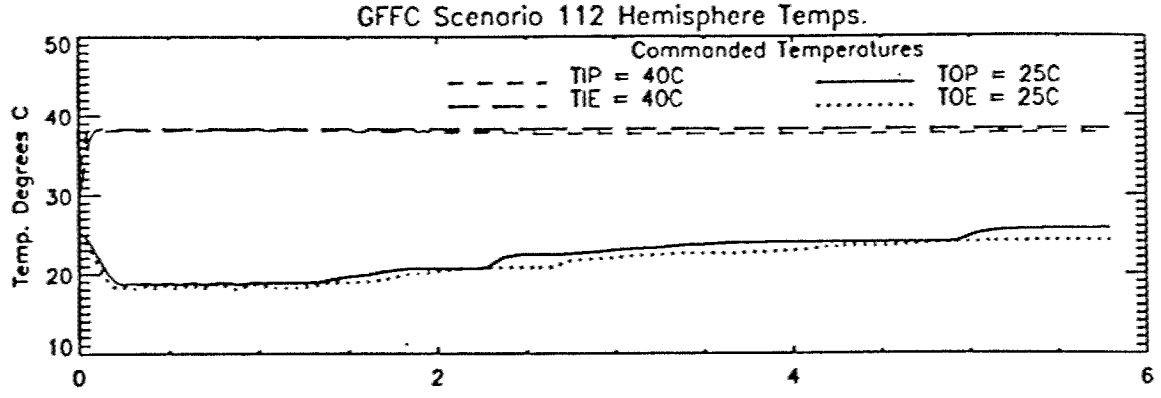
GFFC Scenario 112 Hemisphere Temps.
Commanded Temperatures
TIP = 40C
TIE = 40C
TOP = 25C
TOE = 25C
Temp. Degrees C
50
40
30
20
10
0
2
4
6

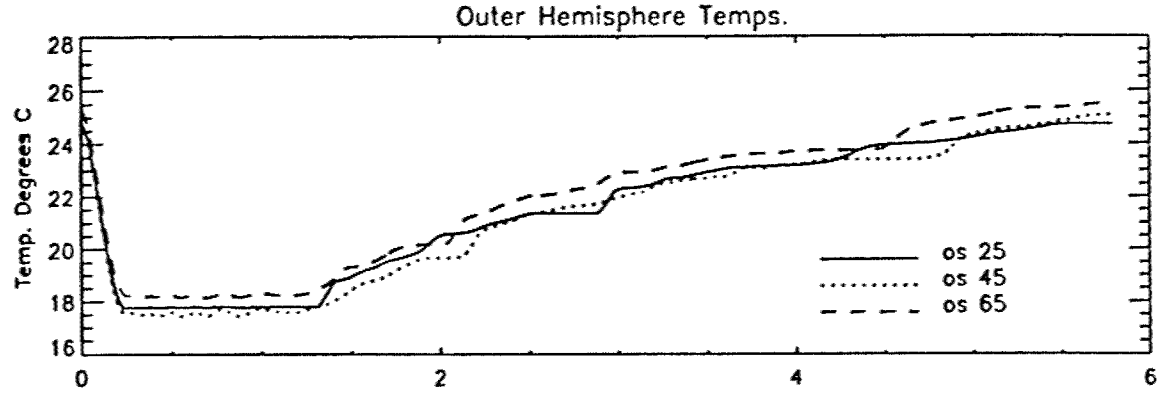
Outer Hemisphere Temps.
Temp. Degrees C
28
26
24
22
20
18
16
os 25
os 45
os 65
0
2
4
6

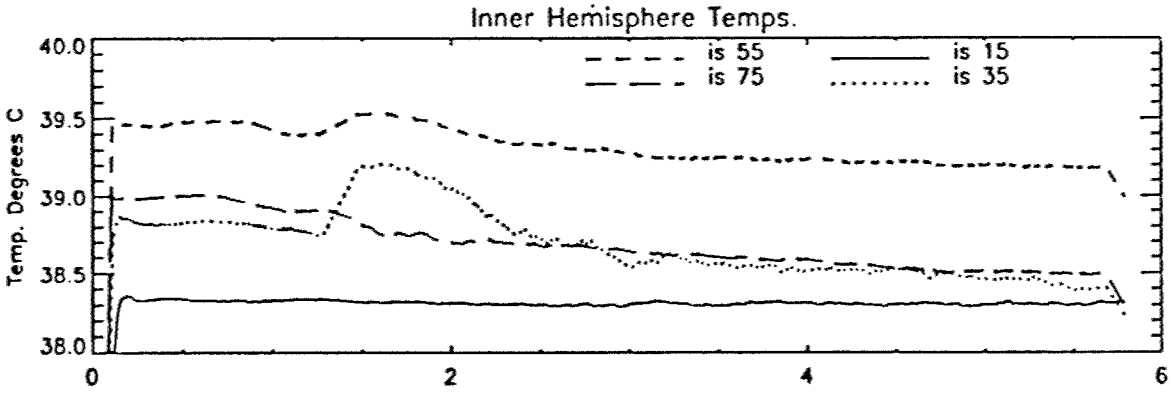
Inner Hemisphere Temps.
is 55
is 75
is 15
is 35
Temp. Degrees C
40.0
39.5
39.0
38.5
38.0
0
2
4
6

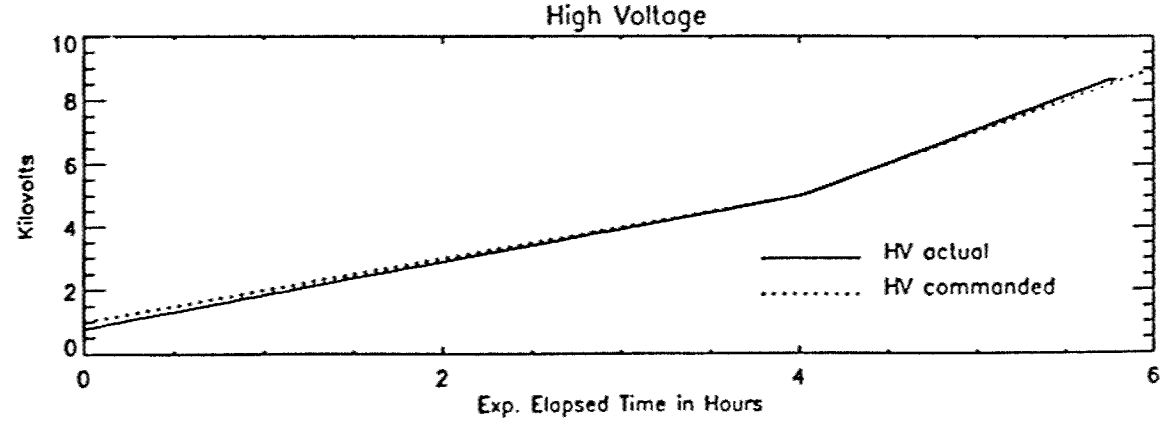
High Voltage
Kilovolts
10
8
6
4
2
0
HV actual
HV commanded
0
2
4
6
Exp. Elapsed Time in Hours

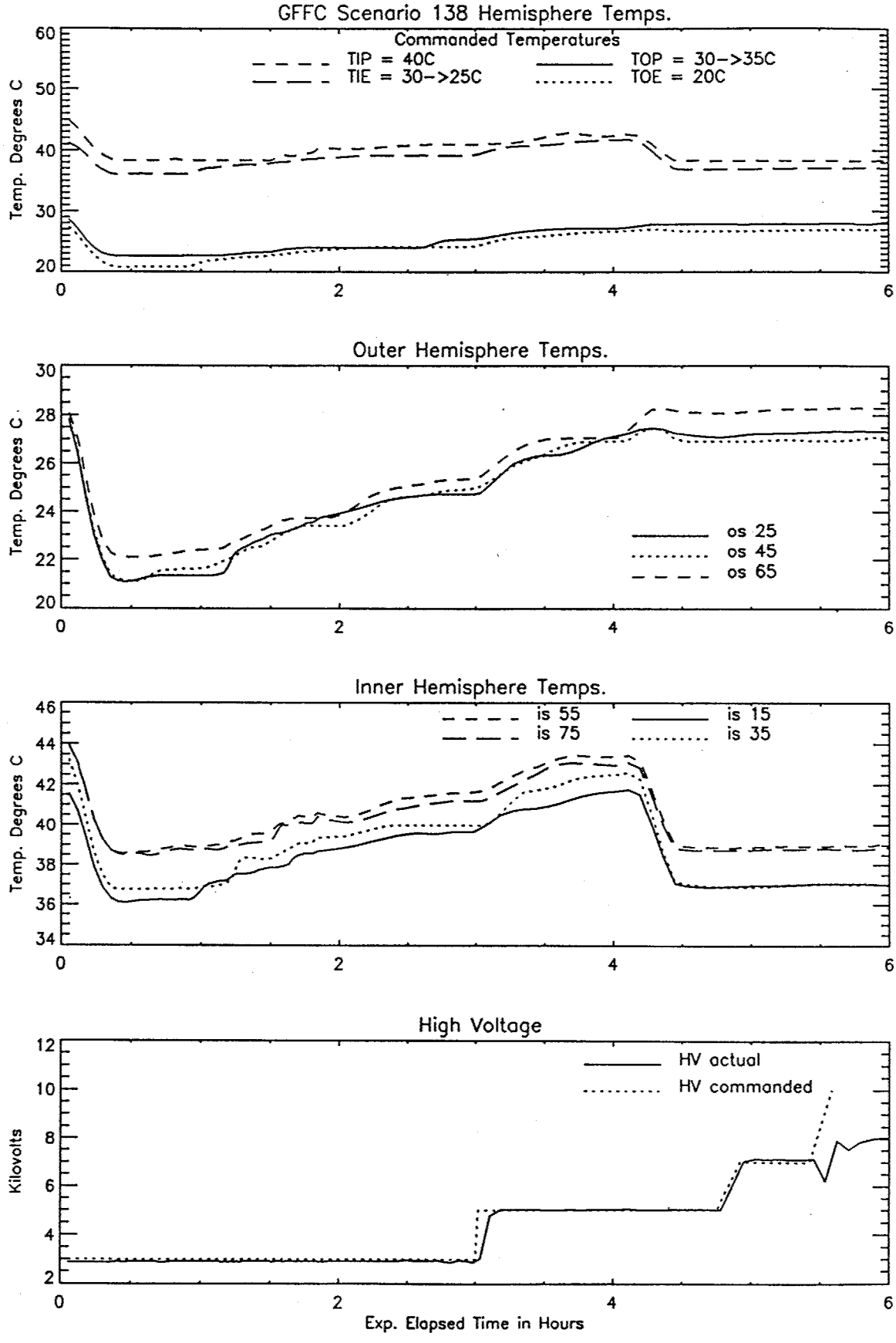
GFFC Scenario 138 Hemisphere Temps.
Commanded Temperatures
TIP = 40C
TIE = 30->25C
TOP = 30->35C
TOE = 20C
Temp. Degrees C
60
50
40
30
20
0
2
4
6
Outer Hemisphere Temps.
os 25
os 45
os 65
30
28
26
24
22
20
Inner Hemisphere Temps.
is 55
is 75
is 15
is 35
46
44
42
40
38
36
34
High Voltage
HV actual
HV commanded
Kilovolts
12
10
8
6
4
2
Exp. Elapsed Time in Hours

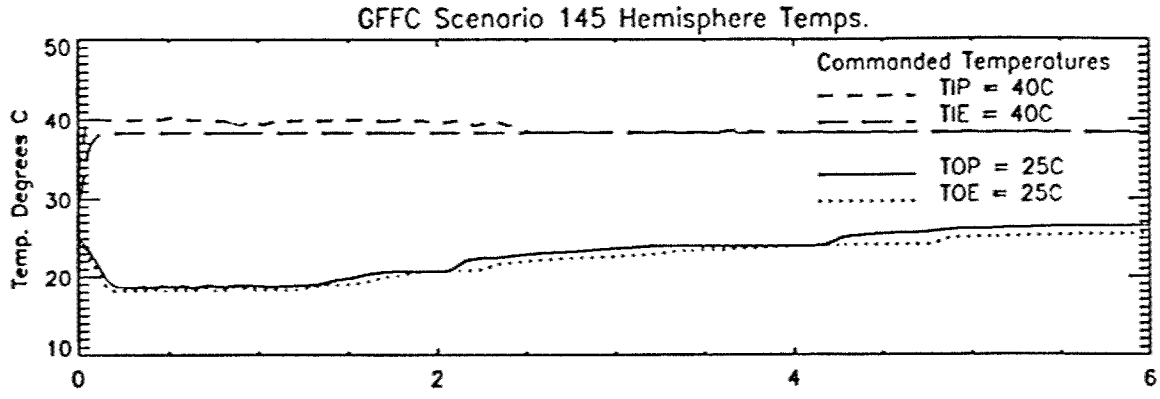
GFFC Scenario 145 Hemisphere Temps.
Temp. Degrees C
Commanded Temperatures
TIP = 40C
TIE = 40C
TOP = 25C
TOE = 25C

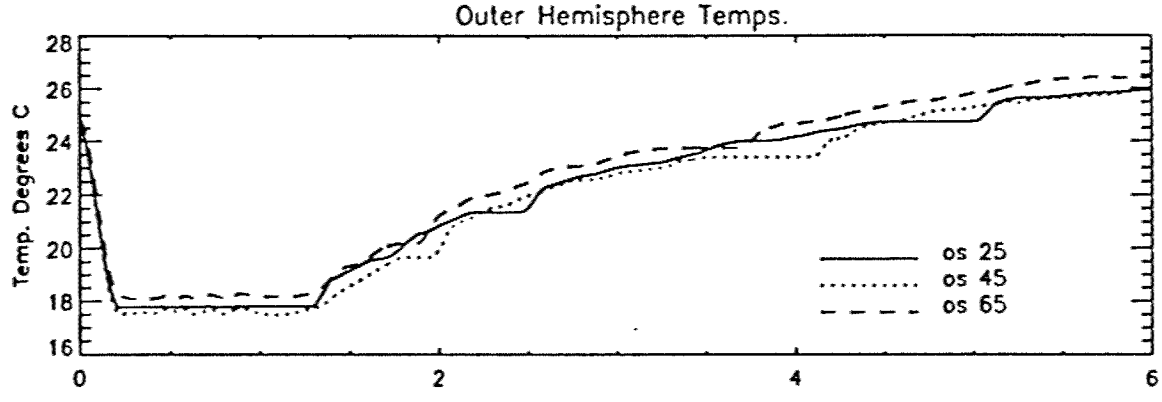
Outer Hemisphere Temps.
Temp. Degrees C
os 25
os 45
os 65

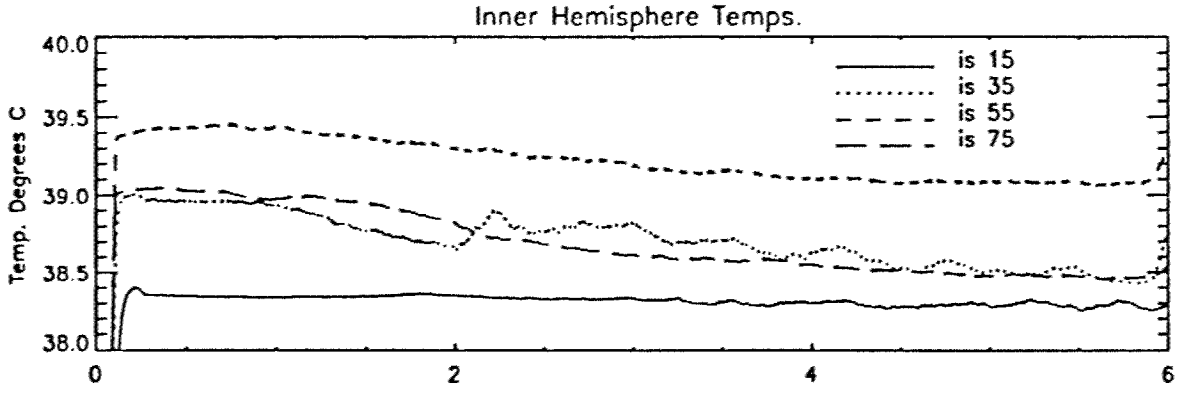
Inner Hemisphere Temps.
Temp. Degrees C
is 15
is 35
is 55
is 75

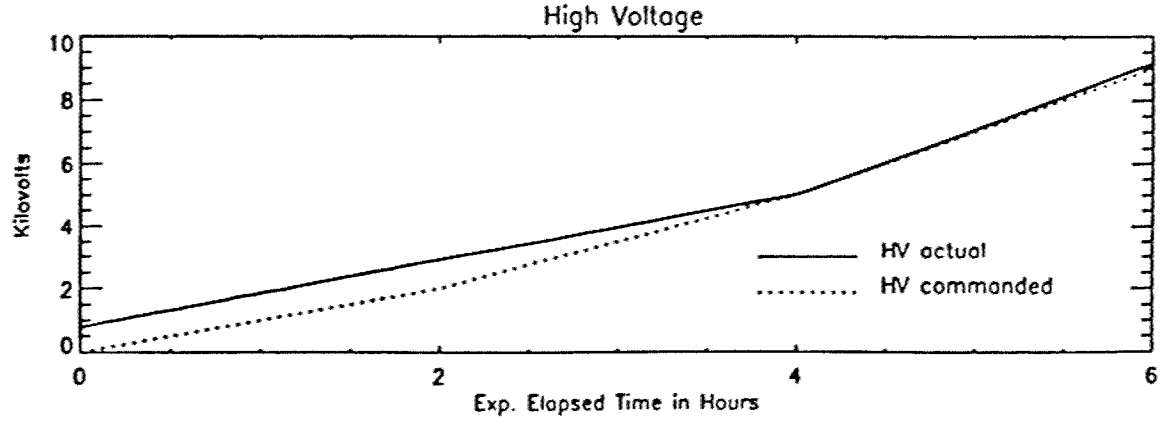
High Voltage
Kilovolts
HV actual
HV commanded
Exp. Elapsed Time in Hours

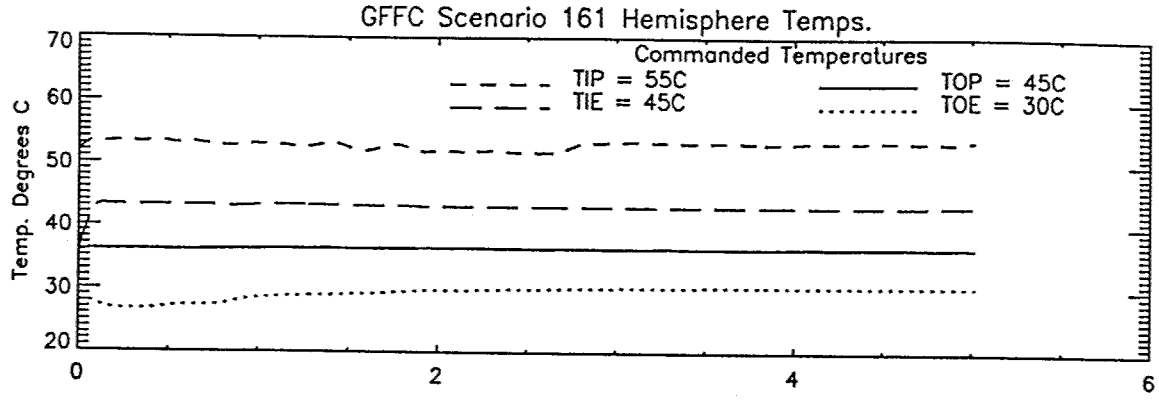
GFFC Scenario 161 Hemisphere Temps.
Commanded Temperatures
TIP = 55C
TIE = 45C
TOP = 45C
TOE = 30C
Temp. Degrees C
70
60
50
40
30
20
0
2
4
6

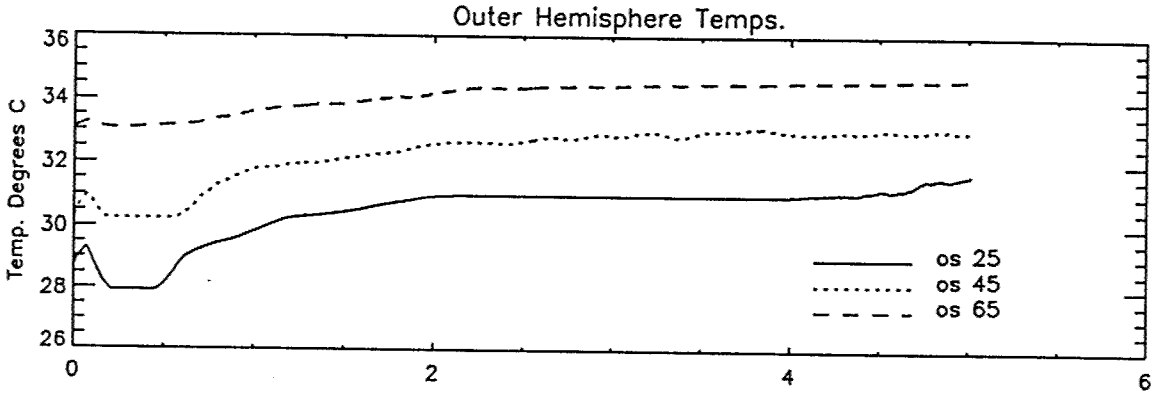
Outer Hemisphere Temps.
Temp. Degrees C
36
34
32
30
28
26
os 25
os 45
os 65
0
2
4
6

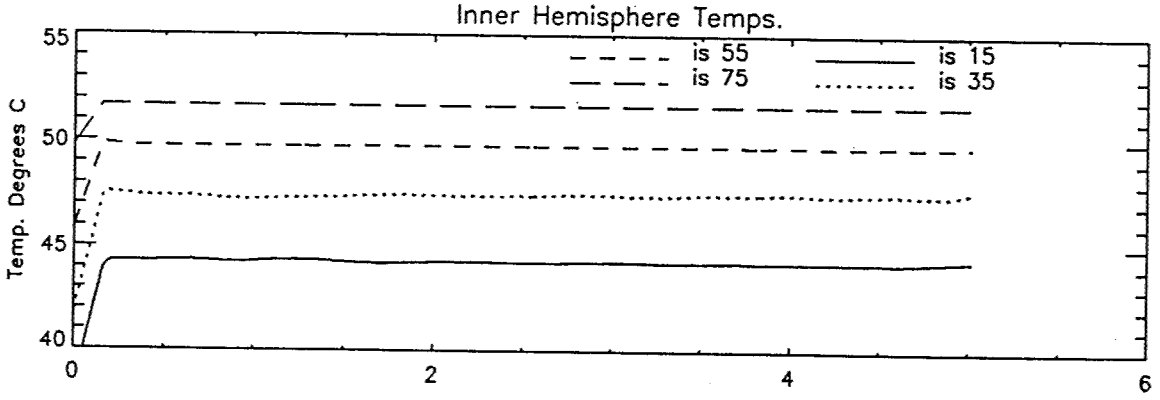
Inner Hemisphere Temps.
Temp. Degrees C
55
50
45
40
is 55
is 75
is 15
is 35
0
2
4
6

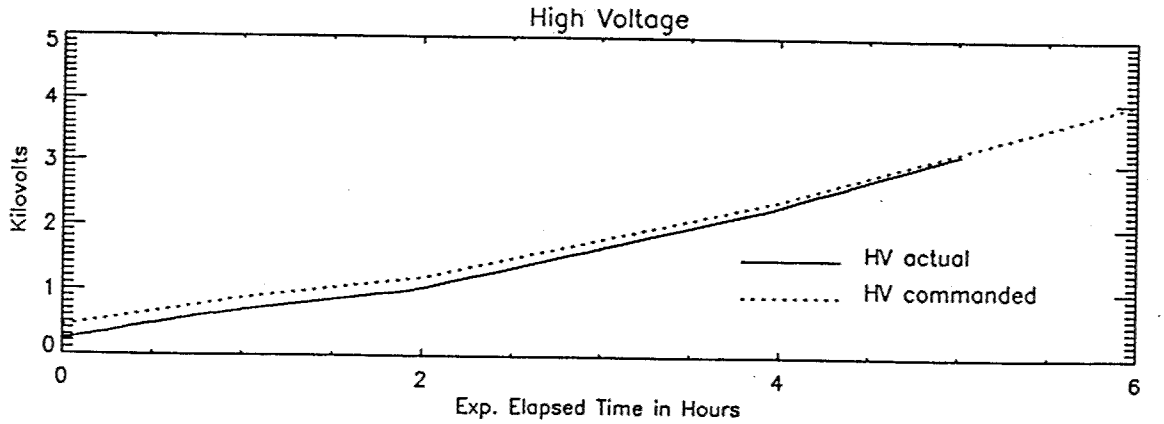
High Voltage
Kilovolts
5
4
3
2
1
0
HV actual
HV commanded
0
2
4
6
Exp. Elapsed Time in Hours

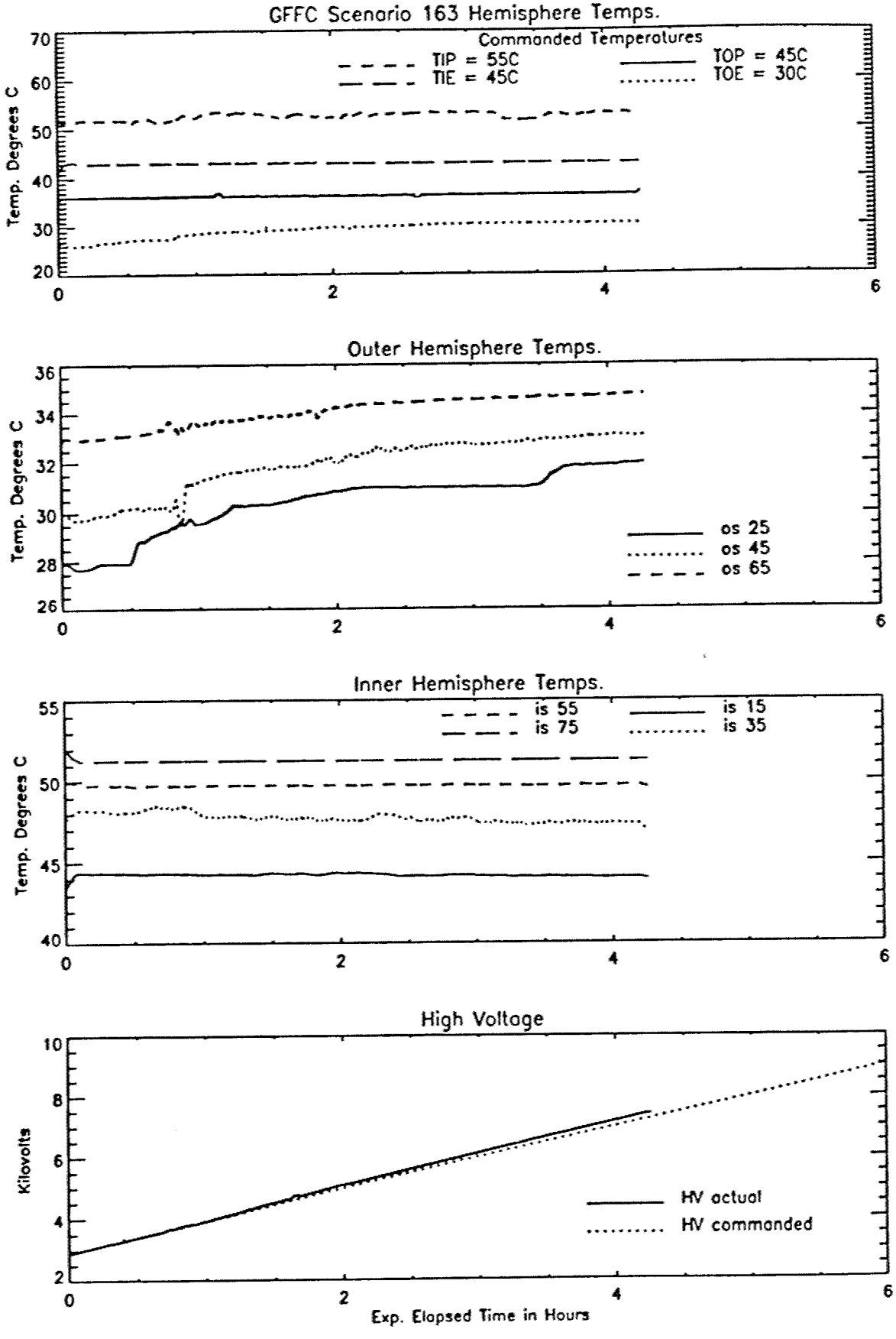
GFFC Scenario 163 Hemisphere Temps.
Commanded Temperatures
TIP = 55C
TIE = 45C
TOP = 45C
TOE = 30C
Temp. Degrees C
70
60
50
40
30
20
0
2
4
6
Outer Hemisphere Temps.
os 25
os 45
os 65
Temp. Degrees C
36
34
32
30
28
26
Inner Hemisphere Temps.
is 55
is 75
is 15
is 35
Temp. Degrees C
55
50
45
40
High Voltage
HV actual
HV commanded
Kilovolts
10
8
6
4
2
Exp. Elapsed Time in Hours

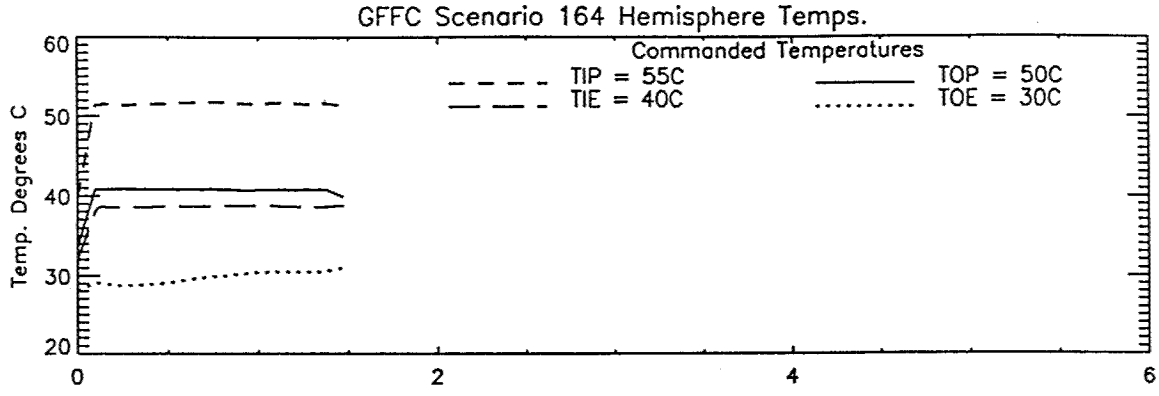
GFFC Scenario 164 Hemisphere Temps.
Commanded Temperatures
TIP = 55C
TIE = 40C
TOP = 50C
TOE = 30C
Temp. Degrees C
60
50
40
30
20
0
2
4
6

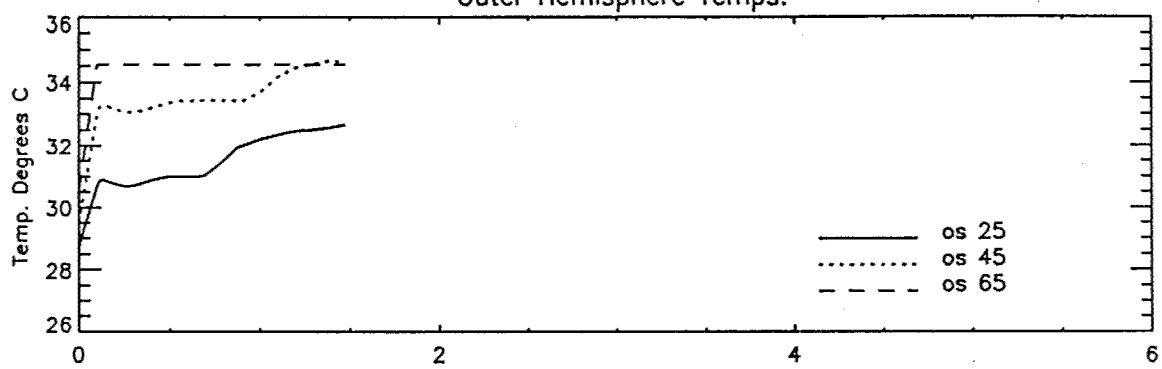
Outer Hemisphere Temps.
os 25
os 45
os 65
Temp. Degrees C
36
34
32
30
28
26
0
2
4
6

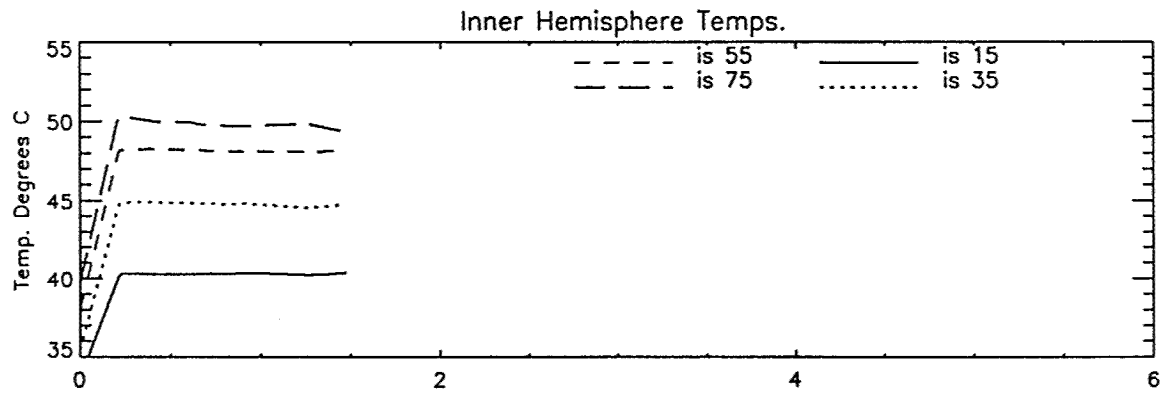
Inner Hemisphere Temps.
is 55
is 75
is 15
is 35
Temp. Degrees C
55
50
45
40
35
0
2
4
6

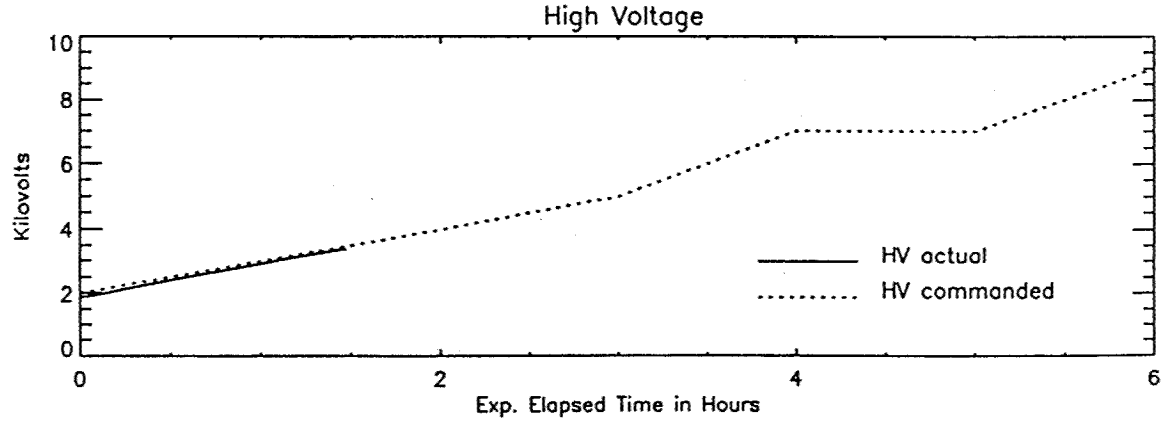
High Voltage
HV actual
HV commanded
Kilovolts
10
8
6
4
2
0
0
2
4
6
Exp. Elapsed Time in Hours

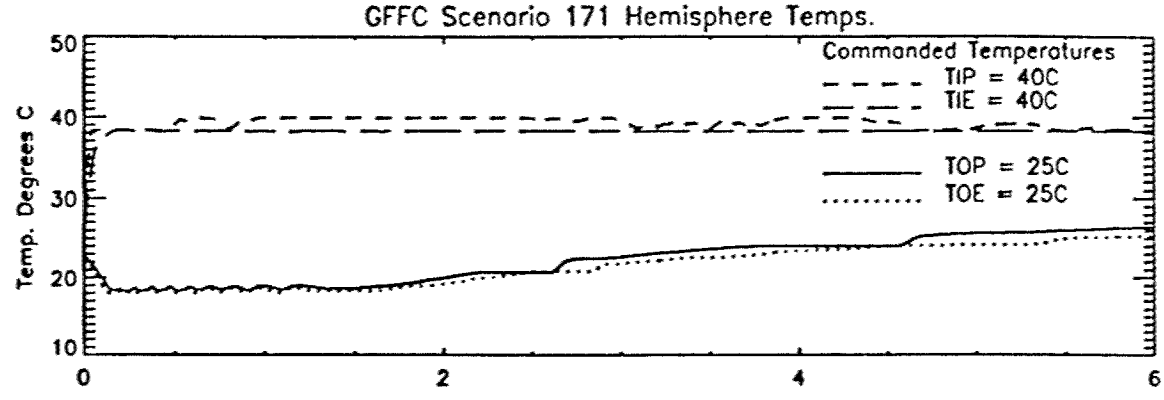
GFFC Scenario 171 Hemisphere Temps.
Commanded Temperatures
TIP = 40C
TIE = 40C
TOP = 25C
TOE = 25C
Temp. Degrees C
50
40
30
20
10
0
2
4
6

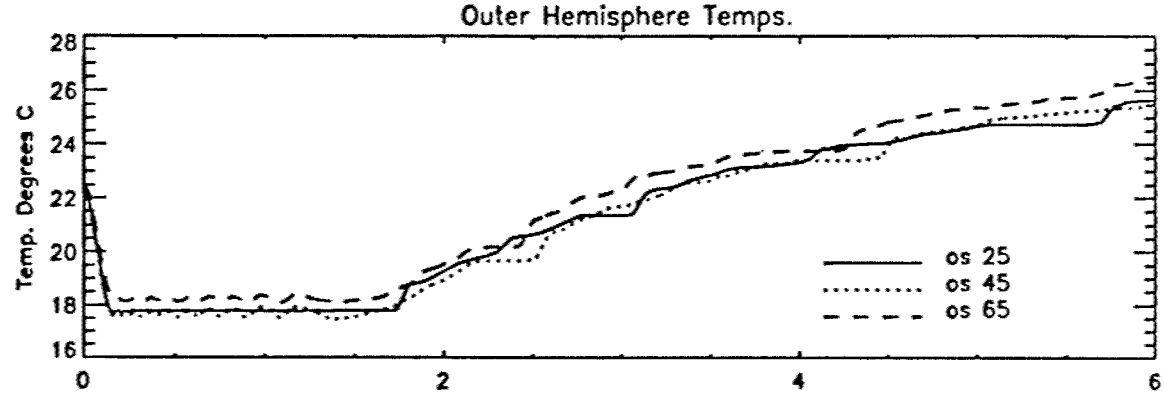
Outer Hemisphere Temps.
os 25
os 45
os 65
Temp. Degrees C
28
26
24
22
20
18
16
0
2
4
6

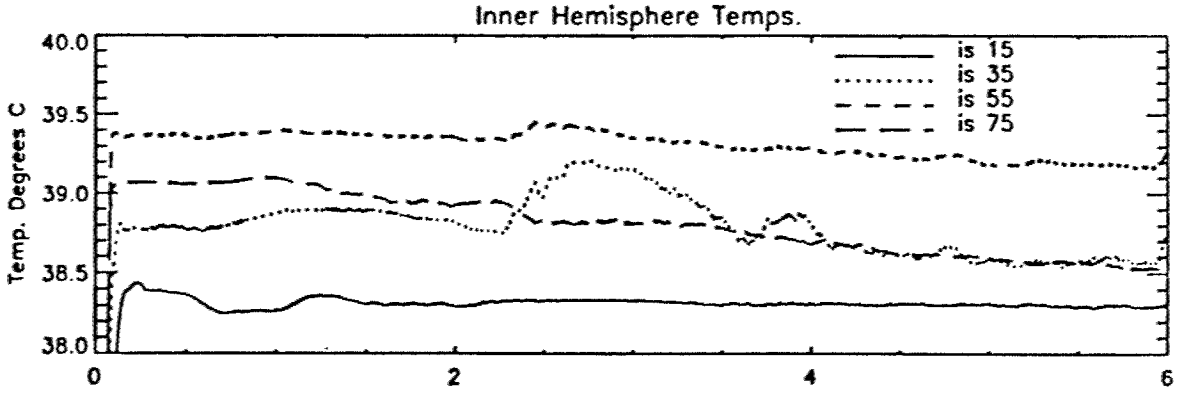
Inner Hemisphere Temps.
is 15
is 35
is 55
is 75
Temp. Degrees C
40.0
39.5
39.0
38.5
38.0
0
2
4
6

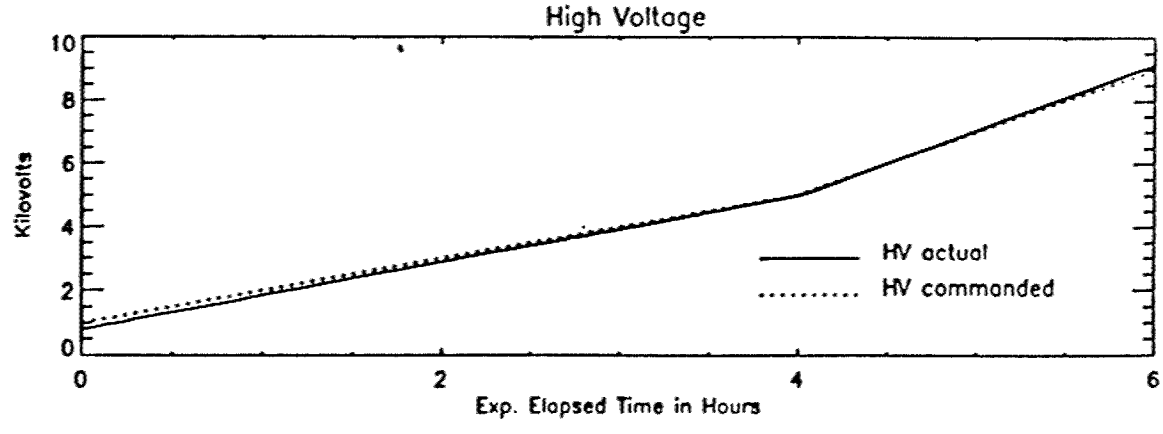
High Voltage
HV actual
HV commanded
Kilovolts
10
8
6
4
2
0
0
2
4
6
Exp. Elapsed Time in Hours

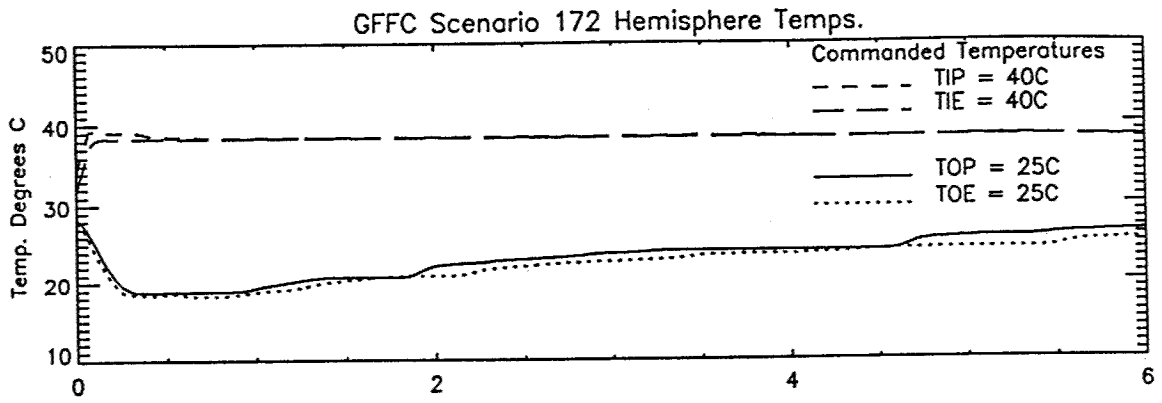
GFFC Scenario 172 Hemisphere Temps.
Commanded Temperatures
TIP = 40C
TIE = 40C
TOP = 25C
TOE = 25C
Temp. Degrees C
50
40
30
20
10
0
2
4
6

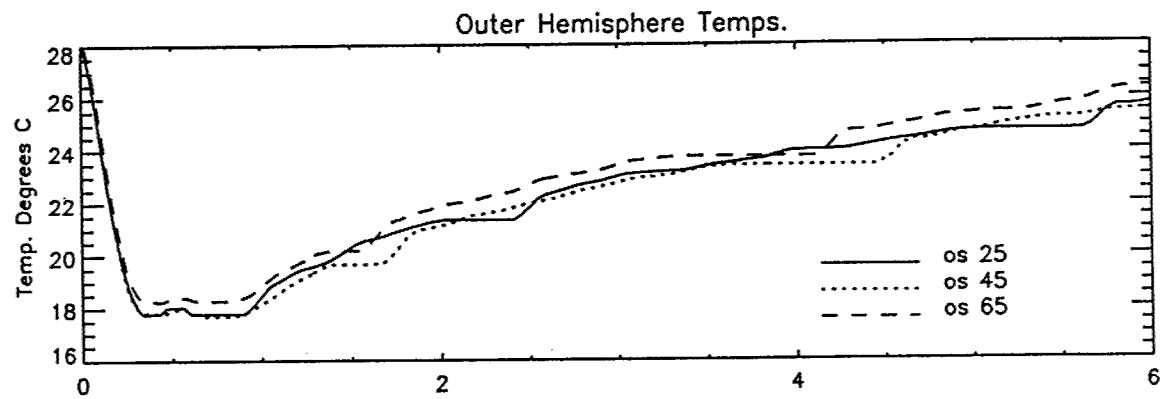
Outer Hemisphere Temps.
os 25
os 45
os 65
Temp. Degrees C
28
26
24
22
20
18
16
0
2
4
6

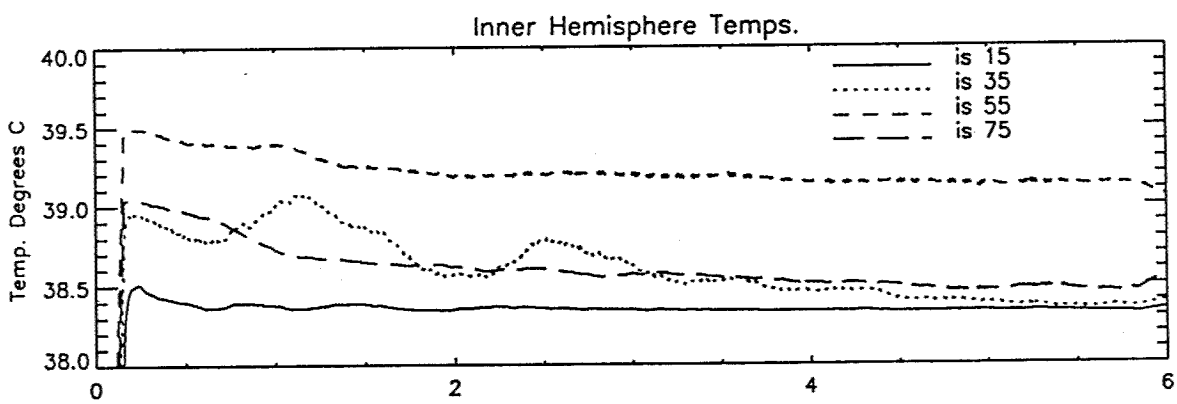
Inner Hemisphere Temps.
is 15
is 35
is 55
is 75
Temp. Degrees C
40.0
39.5
39.0
38.5
38.0
0
2
4
6

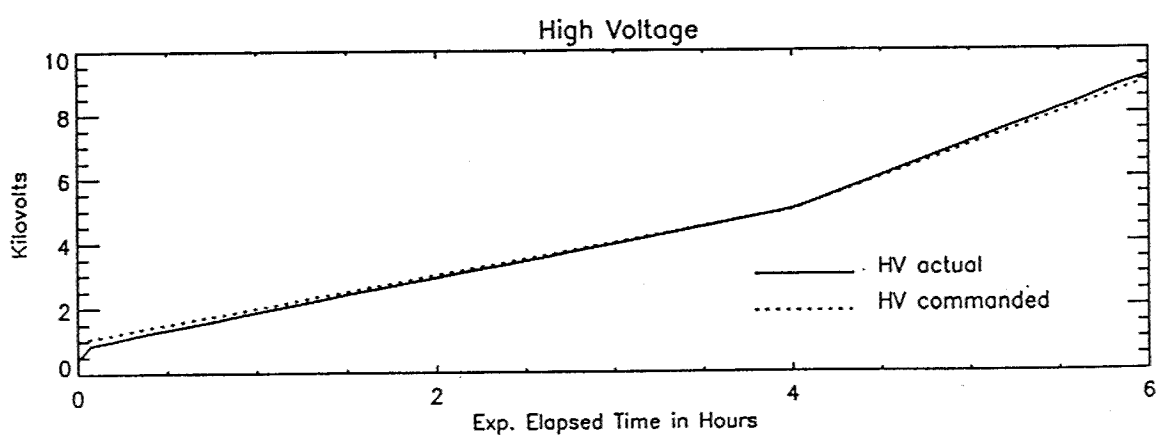
High Voltage
HV actual
HV commanded
Kilovolts
10
8
6
4
2
0
0
2
4
6
Exp. Elapsed Time in Hours

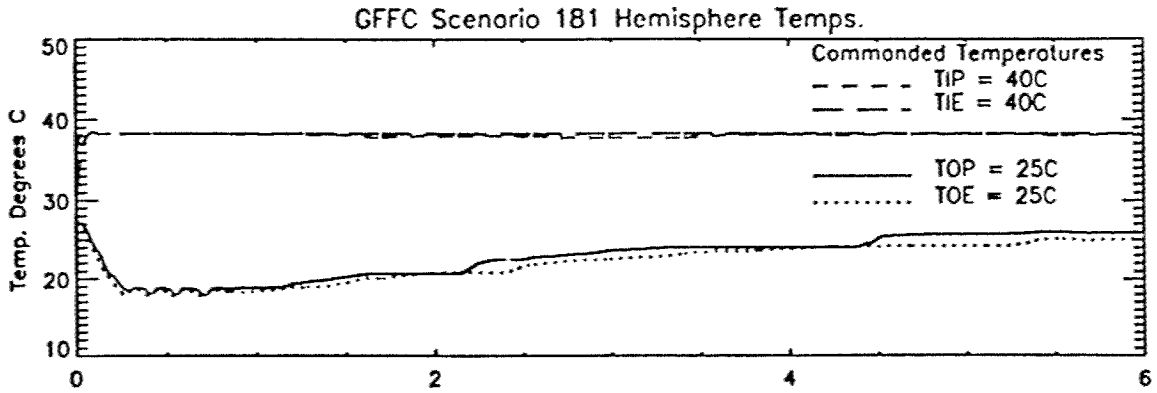
GFFC Scenario 181 Hemisphere Temps.
Commanded Temperatures
TIP = 40C
TIE = 40C
TOP = 25C
TOE = 25C
Temp. Degrees C
50
40
30
20
10
0
2
4
6

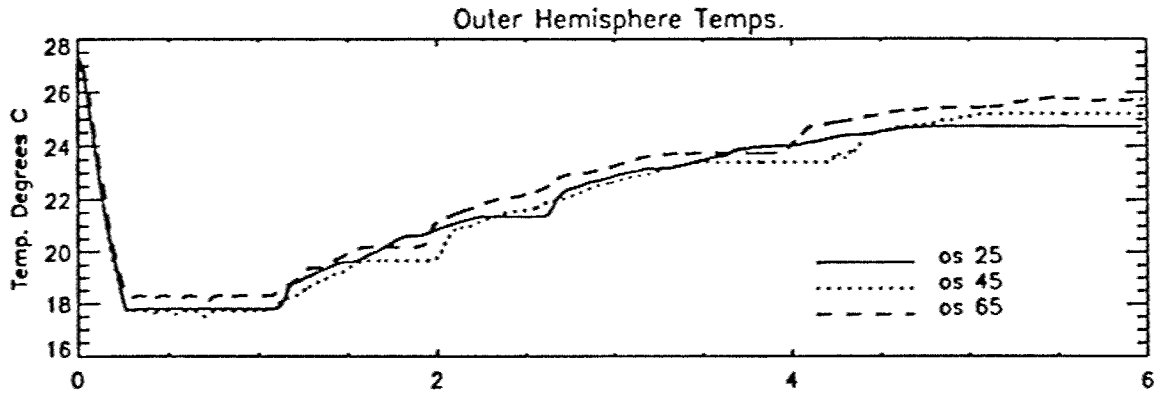
Outer Hemisphere Temps.
os 25
os 45
os 65
Temp. Degrees C
28
26
24
22
20
18
16
0
2
4
6

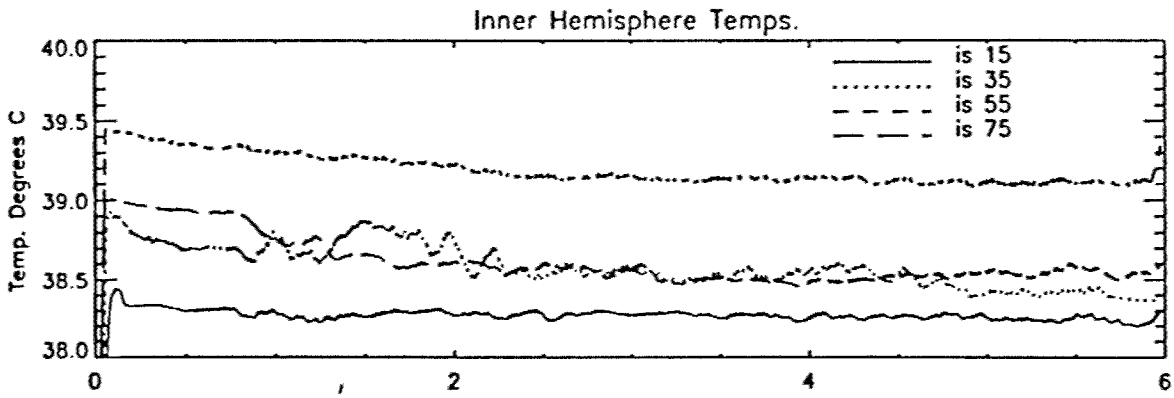
Inner Hemisphere Temps.
is 15
is 35
is 55
is 75
Temp. Degrees C
40.0
39.5
39.0
38.5
38.0
0
2
4
6

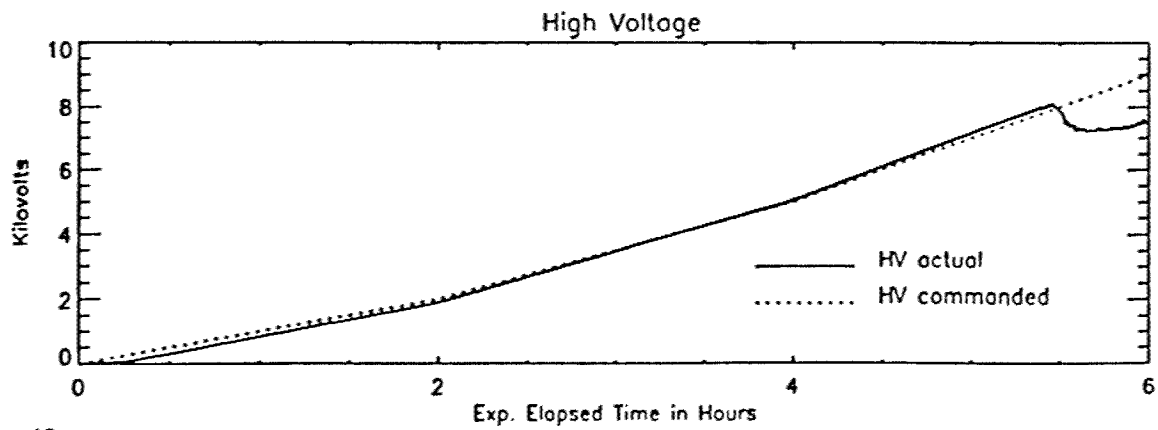
High Voltage
HV actual
HV commanded
Kilovolts
10
8
6
4
2
0
0
2
4
6
Exp. Elapsed Time in Hours

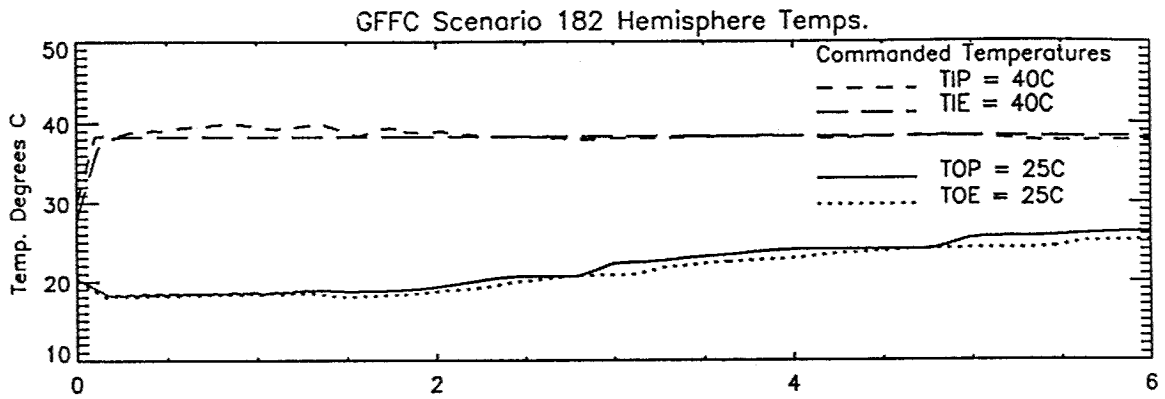
GFFC Scenario 182 Hemisphere Temps.
Commanded Temperatures
TIP = 40C
TIE = 40C
TOP = 25C
TOE = 25C
Temp. Degrees C
50
40
30
20
10
0
2
4
6

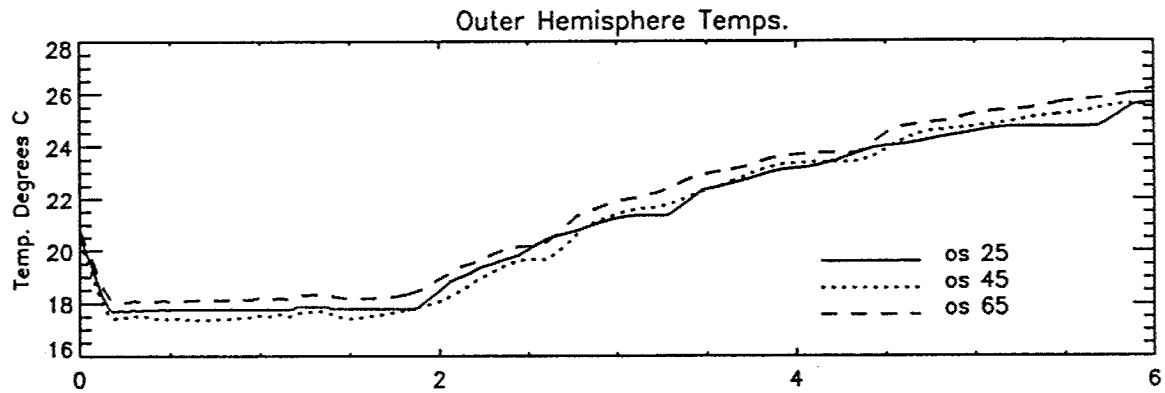
Outer Hemisphere Temps.
os 25
os 45
os 65
Temp. Degrees C
28
26
24
22
20
18
16
0
2
4
6

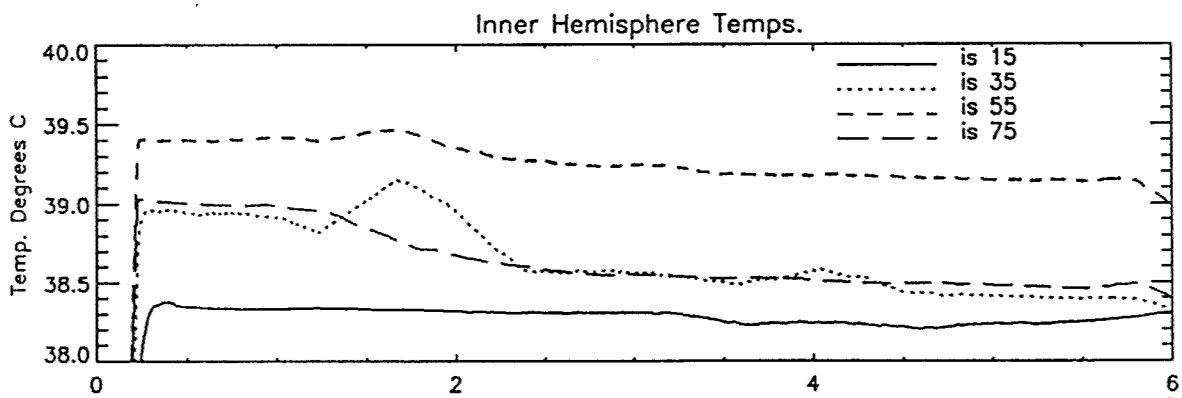
Inner Hemisphere Temps.
is 15
is 35
is 55
is 75
Temp. Degrees C
40.0
39.5
39.0
38.5
38.0
0
2
4
6

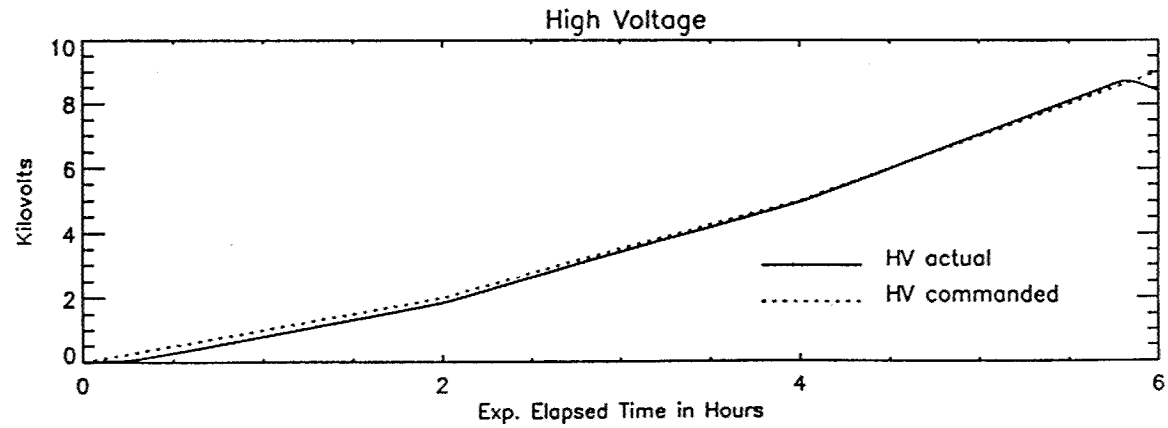
High Voltage
HV actual
HV commanded
Kilovolts
10
8
6
4
2
0
0
2
4
6
Exp. Elapsed Time in Hours

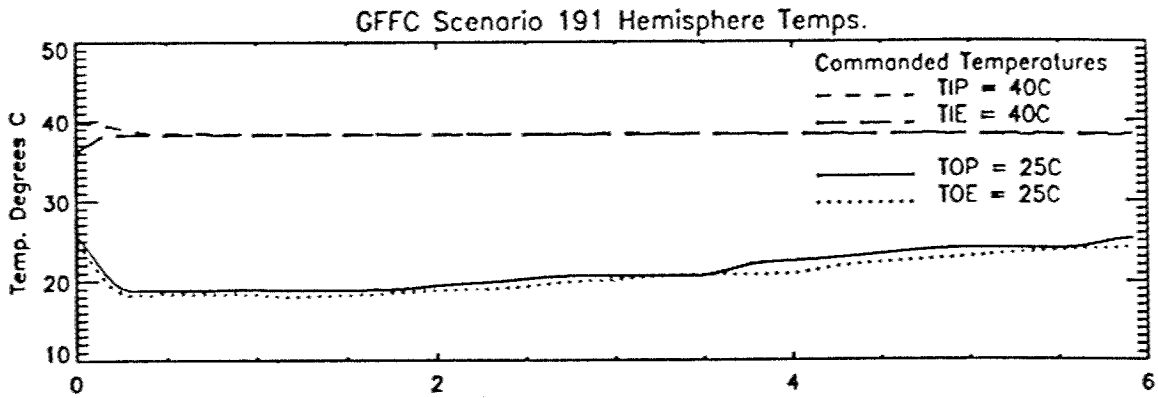
GFFC Scenario 191 Hemisphere Temps.
Temp. Degrees C
50
40
30
20
10
0
2
4
6
Commanded Temperatures
TIP = 40C
TIE = 40C
TOP = 25C
TOE = 25C

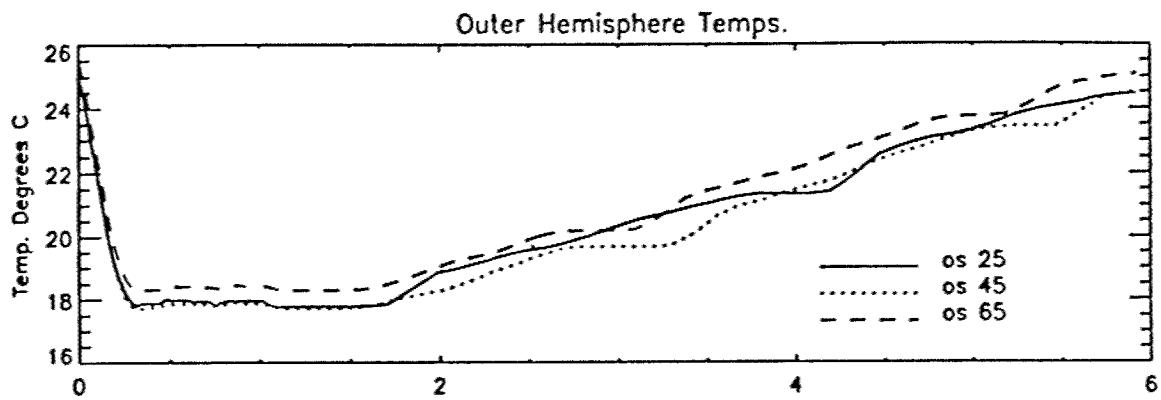
Outer Hemisphere Temps.
Temp. Degrees C
26
24
22
20
18
16
0
2
4
6
os 25
os 45
os 65

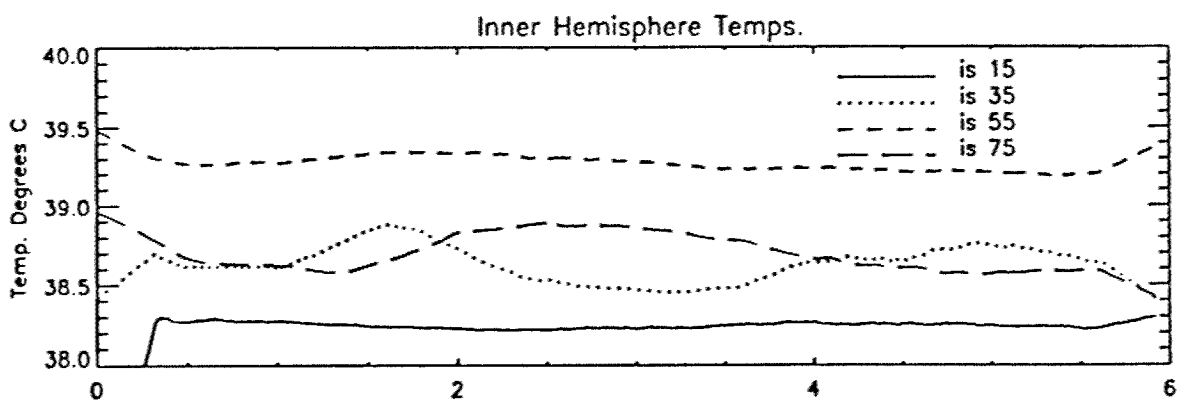
Inner Hemisphere Temps.
Temp. Degrees C
40.0
39.5
39.0
38.5
38.0
0
2
4
6
is 15
is 35
is 55
is 75

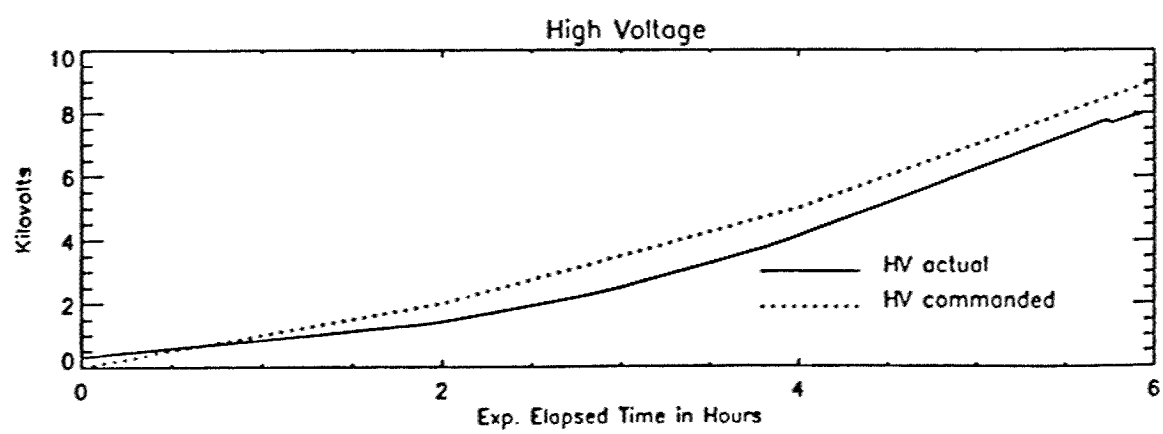
High Voltage
Kilovolts
10
8
6
4
2
0
0
2
4
6
HV actual
HV commanded
Exp. Elapsed Time in Hours

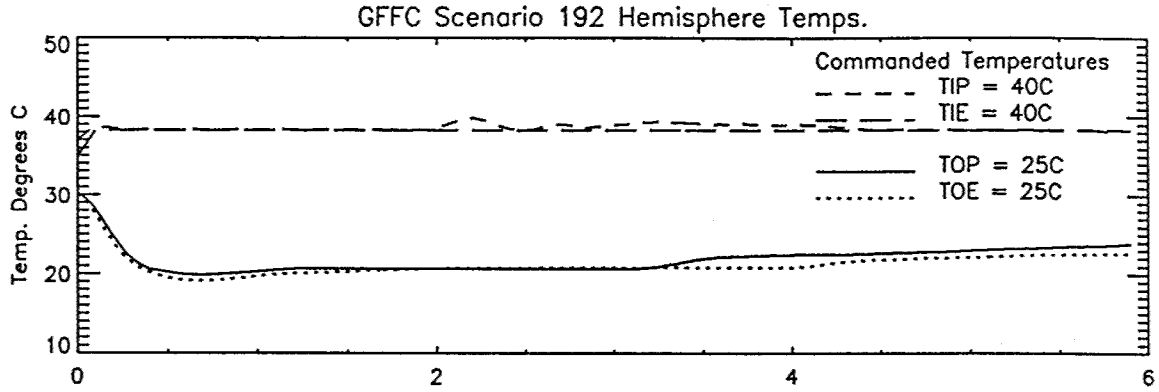
GFFC Scenario 192 Hemisphere Temps.
Temp. Degrees C
50
40
30
20
10
0
2
4
6
Commanded Temperatures
TIP = 40C
TIE = 40C
TOP = 25C
TOE = 25C

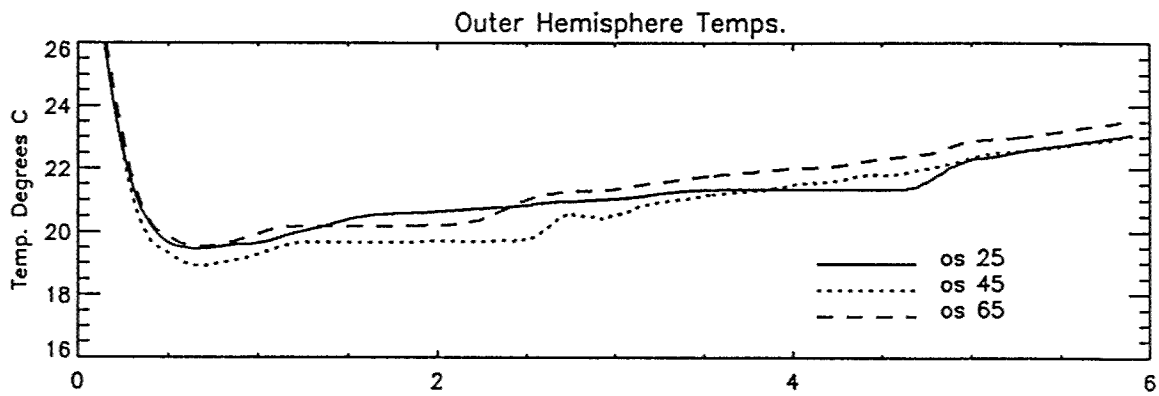
Outer Hemisphere Temps.
Temp. Degrees C
26
24
22
20
18
16
0
2
4
6
os 25
os 45
os 65

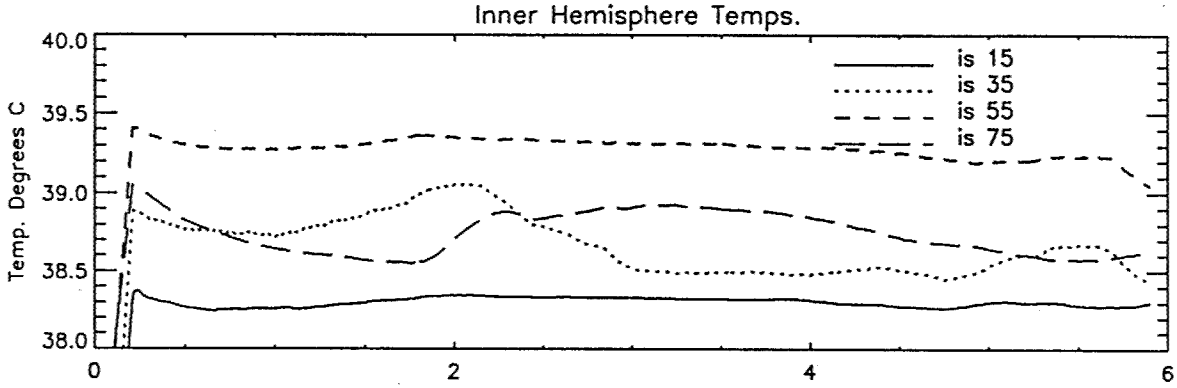
Inner Hemisphere Temps.
Temp. Degrees C
40.0
39.5
39.0
38.5
38.0
0
2
4
6
is 15
is 35
is 55
is 75

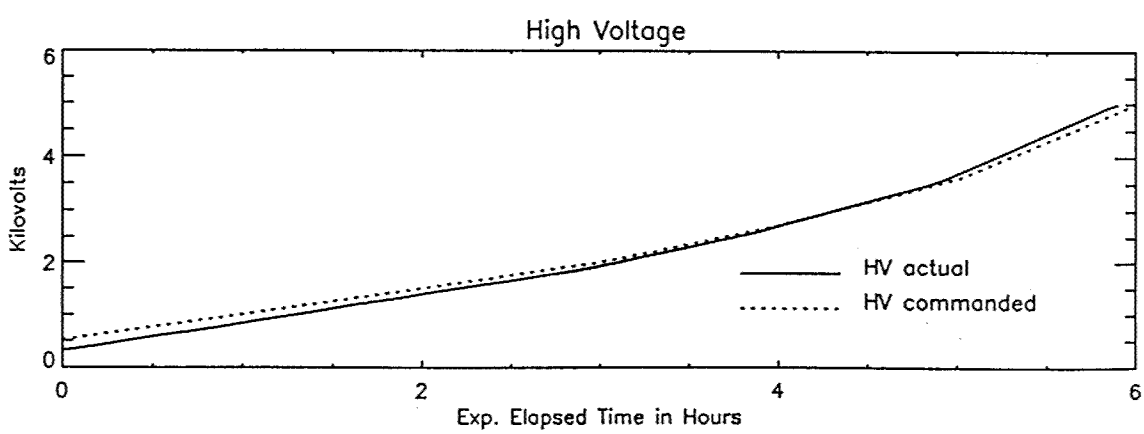
High Voltage
Kilovolts
6
4
2
0
0
2
4
6
HV actual
HV commanded
Exp. Elapsed Time in Hours

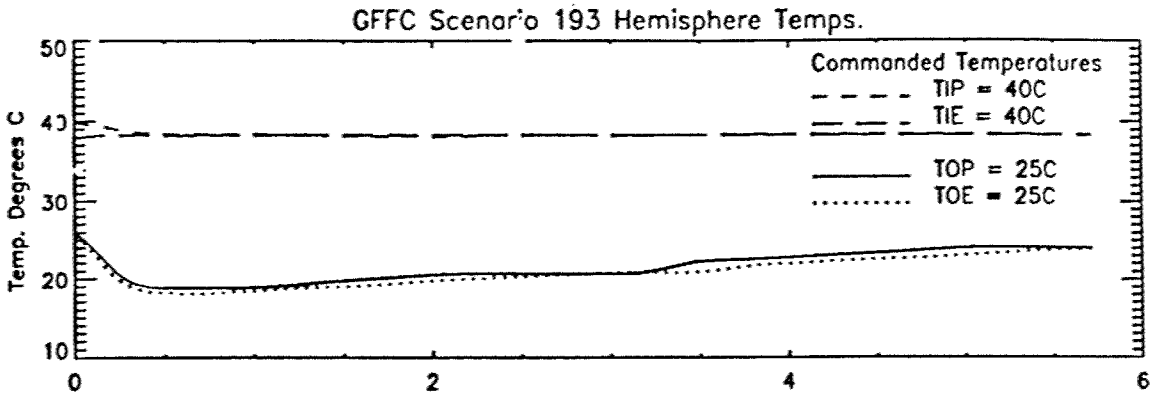
GFFC Scenario 193 Hemisphere Temps.
Commanded Temperatures
TIP = 40C
TIE = 40C
TOP = 25C
TOE = 25C
Temp. Degrees C
50
40
30
20
10
0
2
4
6

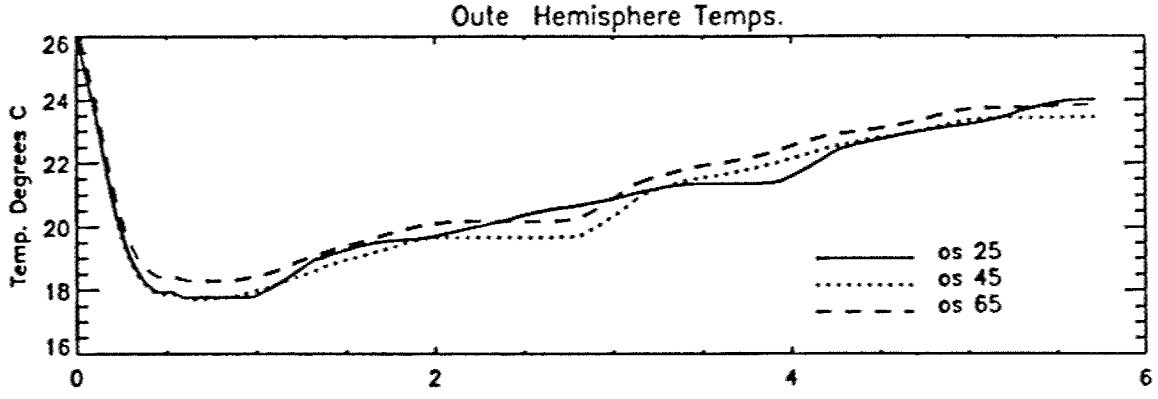
Oute Hemisphere Temps.
os 25
os 45
os 65
Temp. Degrees C
26
24
22
20
18
16
0
2
4
6

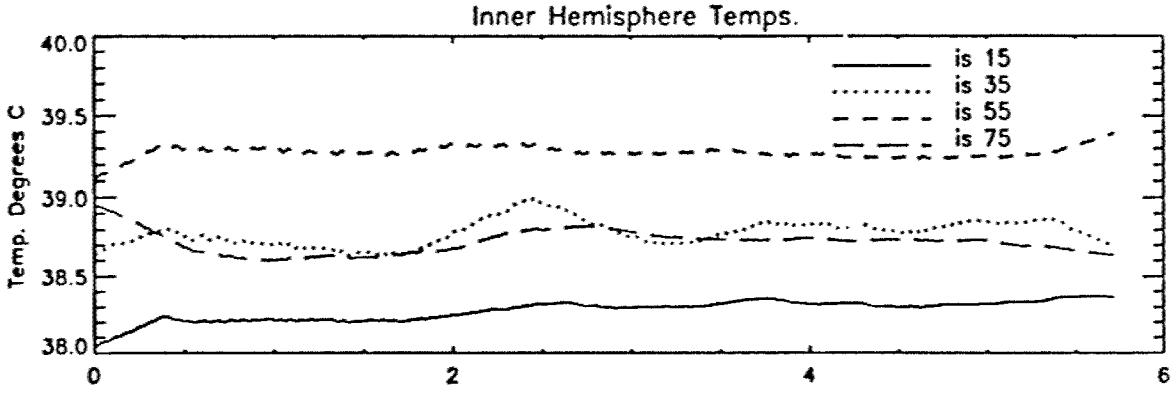
Inner Hemisphere Temps.
is 15
is 35
is 55
is 75
Temp. Degrees C
40.0
39.5
39.0
38.5
38.0
0
2
4
6

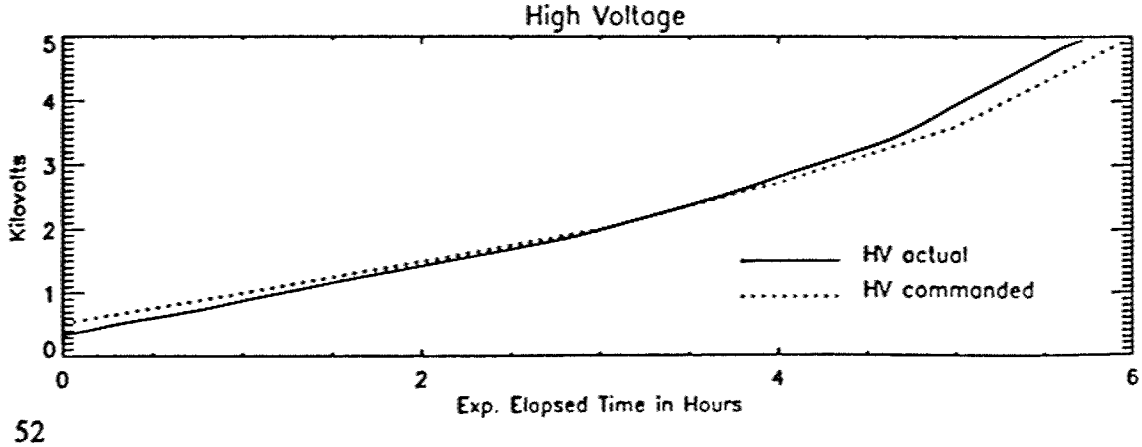
High Voltage
HV actual
HV commanded
Kilovolts
5
4
3
2
1
0
0
2
4
6
Exp. Elapsed Time in Hours

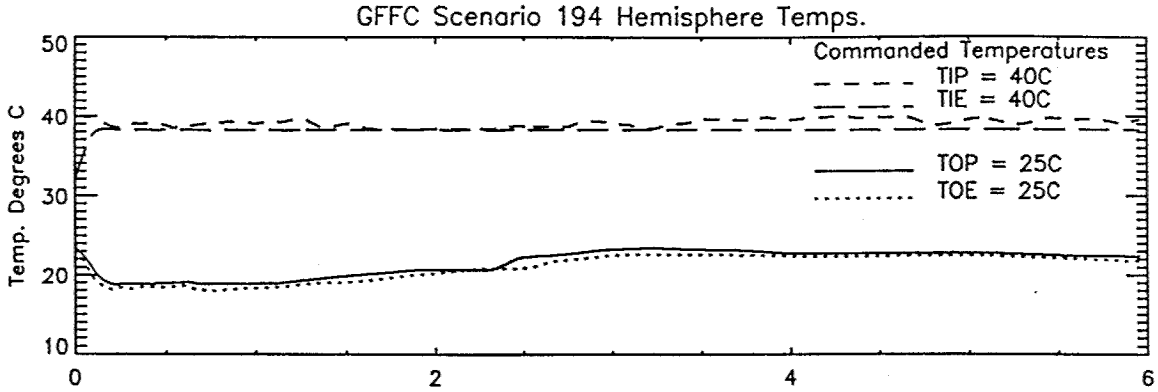
GFFC Scenario 194 Hemisphere Temps.
Commanded Temperatures
TIP = 40C
TIE = 40C
TOP = 25C
TOE = 25C
Temp. Degrees C
50
40
30
20
10
0
2
4
6

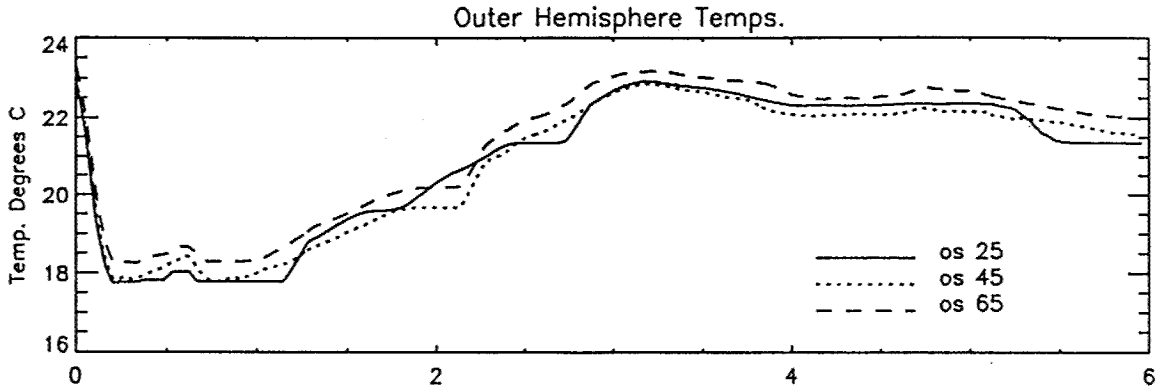
Outer Hemisphere Temps.
os 25
os 45
os 65
Temp. Degrees C
24
22
20
18
16
0
2
4
6

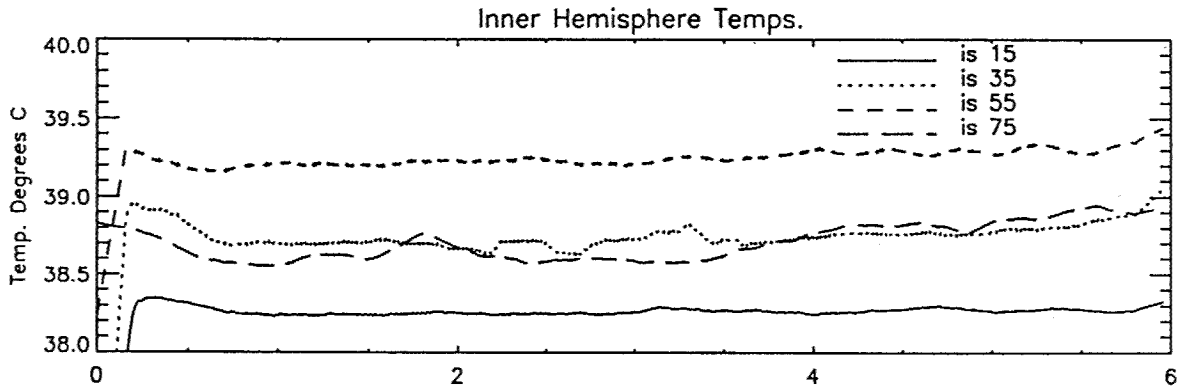
Inner Hemisphere Temps.
is 15
is 35
is 55
is 75
Temp. Degrees C
40.0
39.5
39.0
38.5
38.0
0
2
4
6

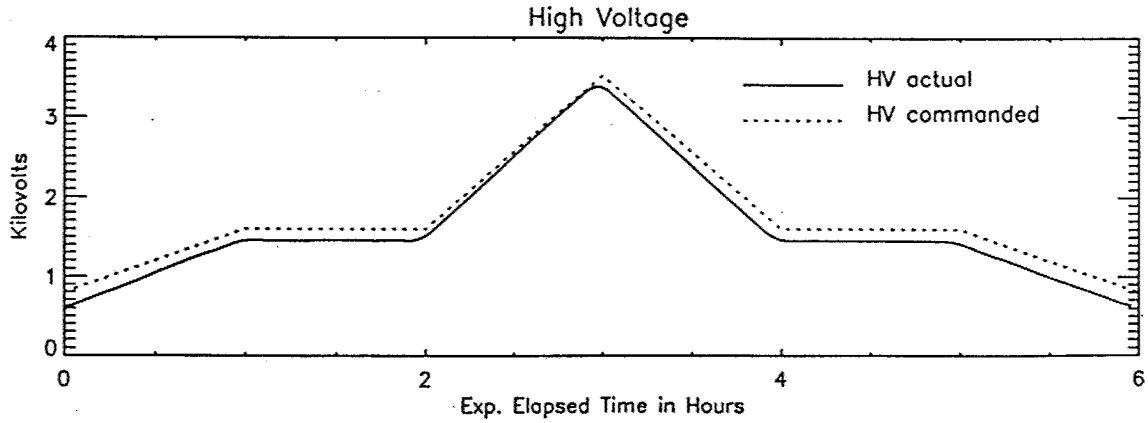
High Voltage
HV actual
HV commanded
Kilovolts
4
3
2
1
0
0
2
4
6
Exp. Elapsed Time in Hours

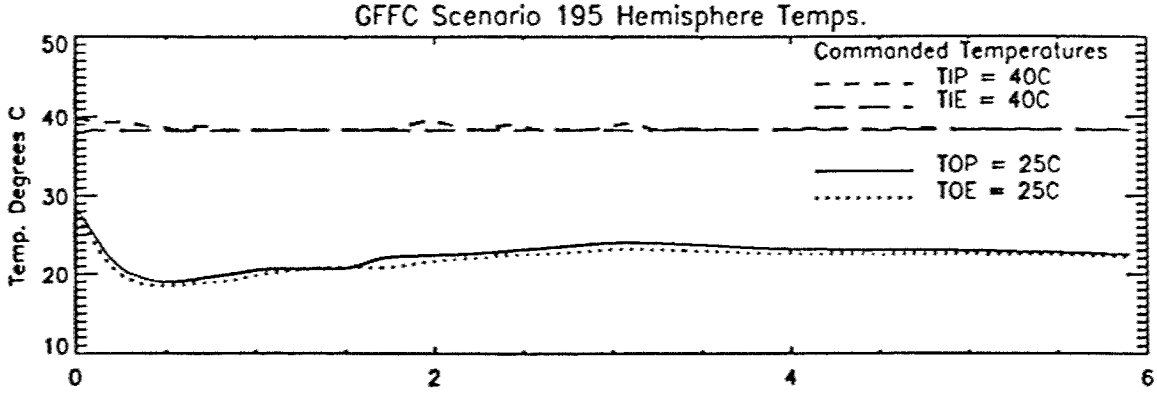
GFFC Scenario 195 Hemisphere Temps.
Commanded Temperatures
TIP = 40C
TIE = 40C
TOP = 25C
TOE = 25C
Temp. Degrees C
50
40
30
20
10
0
2
4
6

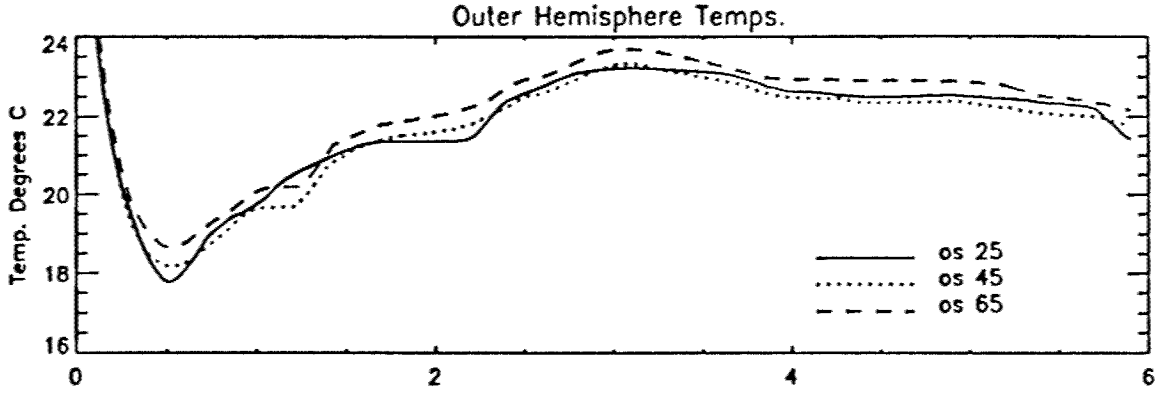
Outer Hemisphere Temps.
os 25
os 45
os 65
Temp. Degrees C
24
22
20
18
16
0
2
4
6

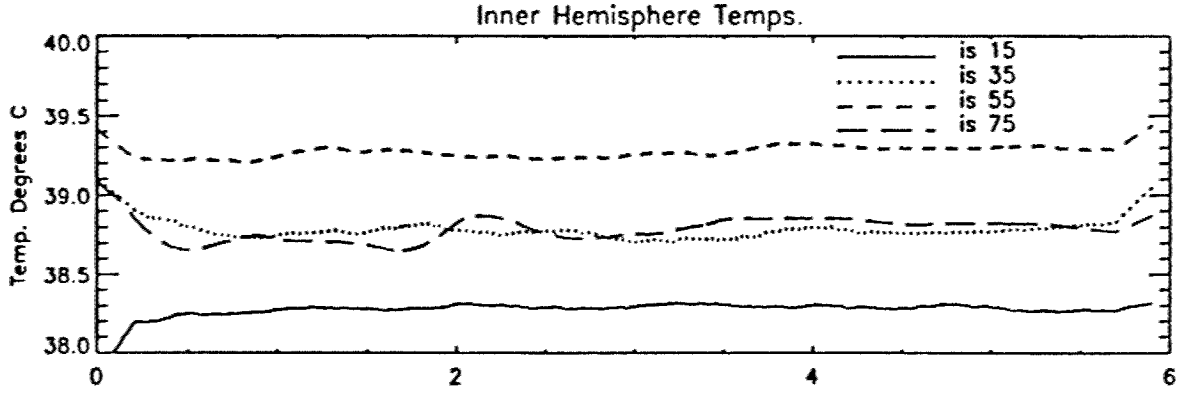
Inner Hemisphere Temps.
is 15
is 35
is 55
is 75
Temp. Degrees C
40.0
39.5
39.0
38.5
38.0
0
2
4
6

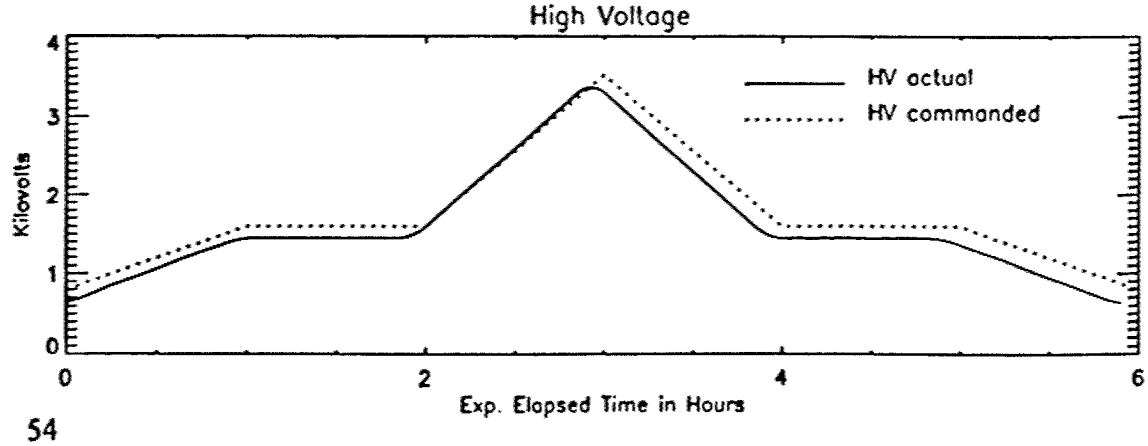
High Voltage
HV actual
HV commanded
Kilovolts
4
3
2
1
0
0
2
4
6
Exp. Elapsed Time in Hours

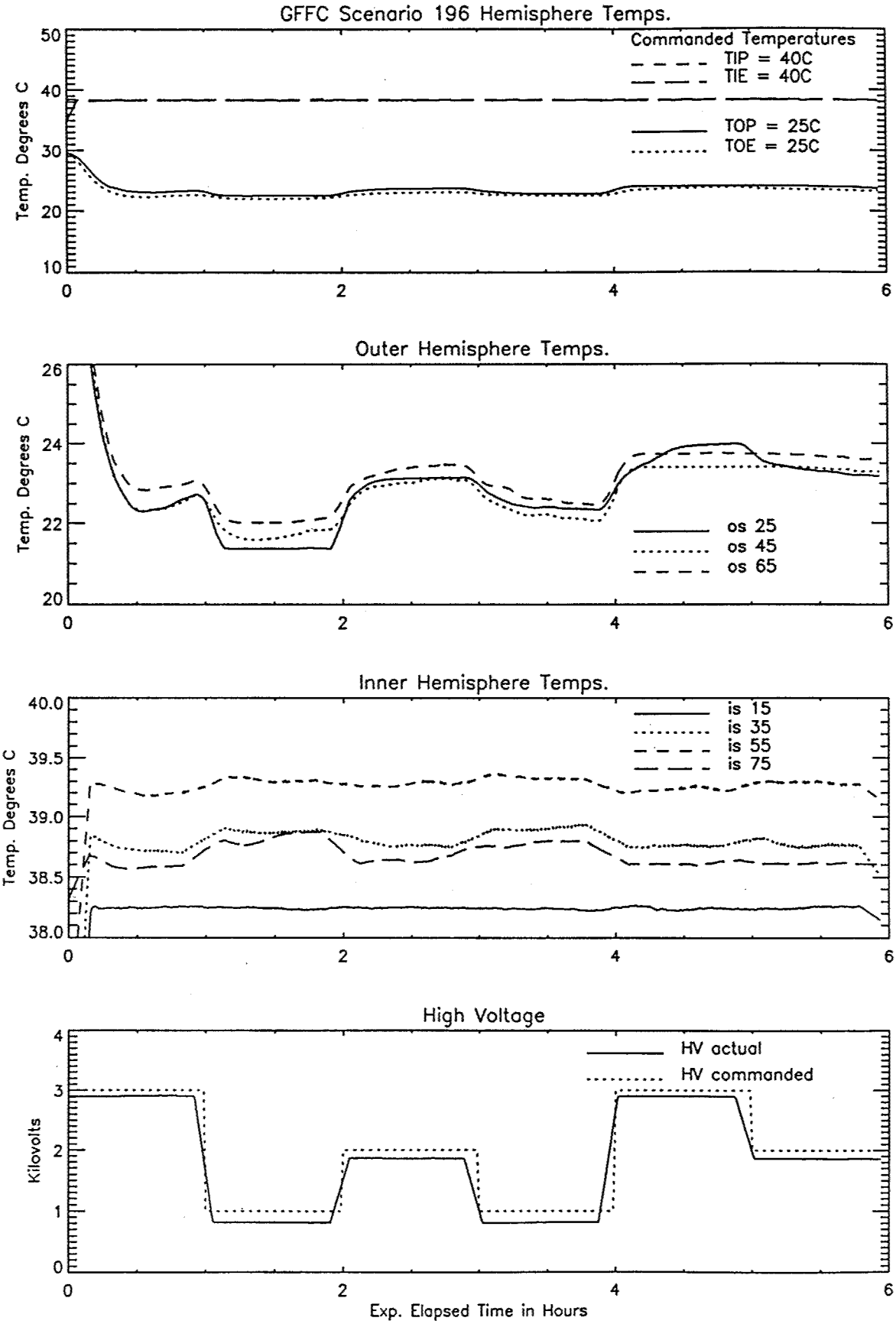
GFFC Scenario 196 Hemisphere Temps.
Commanded Temperatures
TIP = 40C
TIE = 40C
TOP = 25C
TOE = 25C
Temp. Degrees C
50
40
30
20
10
0
2
4
6
Outer Hemisphere Temps.
os 25
os 45
os 65
Temp. Degrees C
26
24
22
20
Inner Hemisphere Temps.
is 15
is 35
is 55
is 75
Temp. Degrees C
40.0
39.5
39.0
38.5
38.0
High Voltage
HV actual
HV commanded
Kilovolts
4
3
2
1
0
Exp. Elapsed Time in Hours

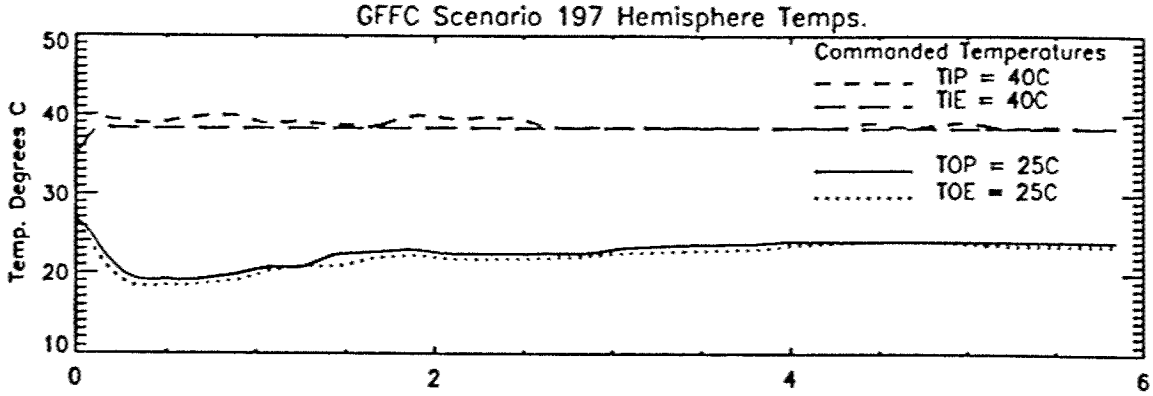
GFFC Scenario 197 Hemisphere Temps.
Commanded Temperatures
TIP = 40C
TIE = 40C
TOP = 25C
TOE = 25C
Temp. Degrees C
50
40
30
20
10
0
2
4
6

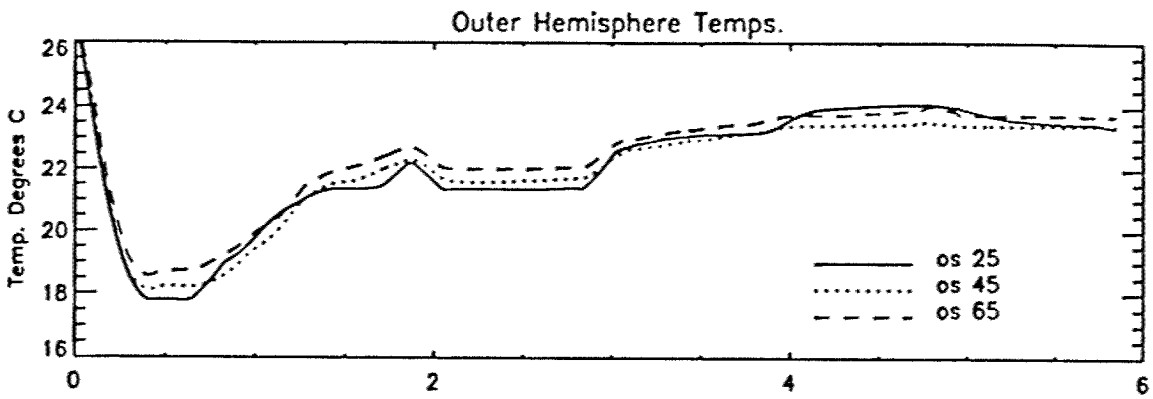
Outer Hemisphere Temps.
os 25
os 45
os 65
Temp. Degrees C
26
24
22
20
18
16
0
2
4
6

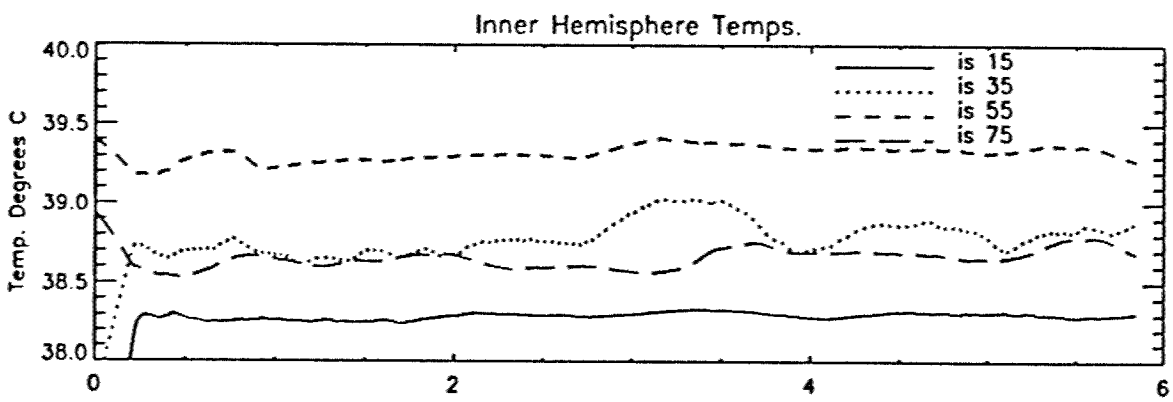
Inner Hemisphere Temps.
is 15
is 35
is 55
is 75
Temp. Degrees C
40.0
39.5
39.0
38.5
38.0
0
2
4
6

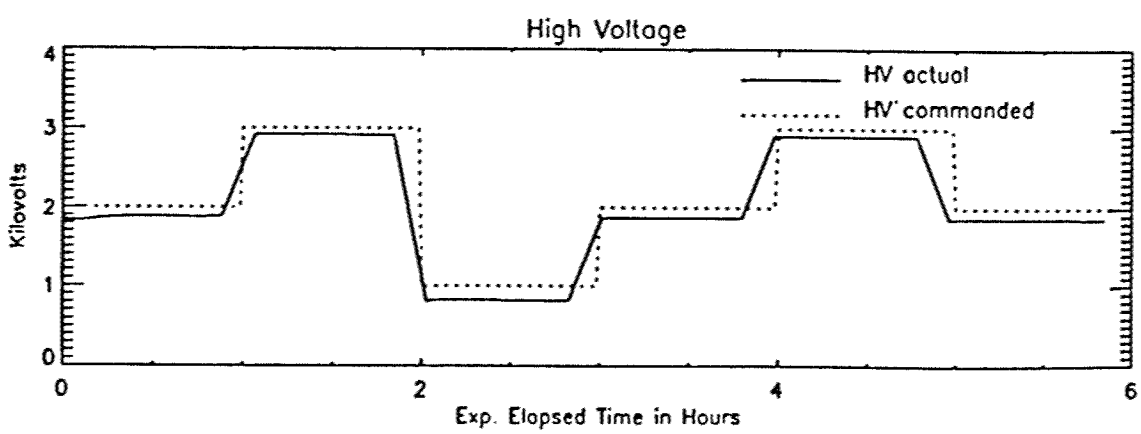
High Voltage
HV actual
HV commanded
Kilovolts
4
3
2
1
0
0
2
4
6
Exp. Elapsed Time in Hours

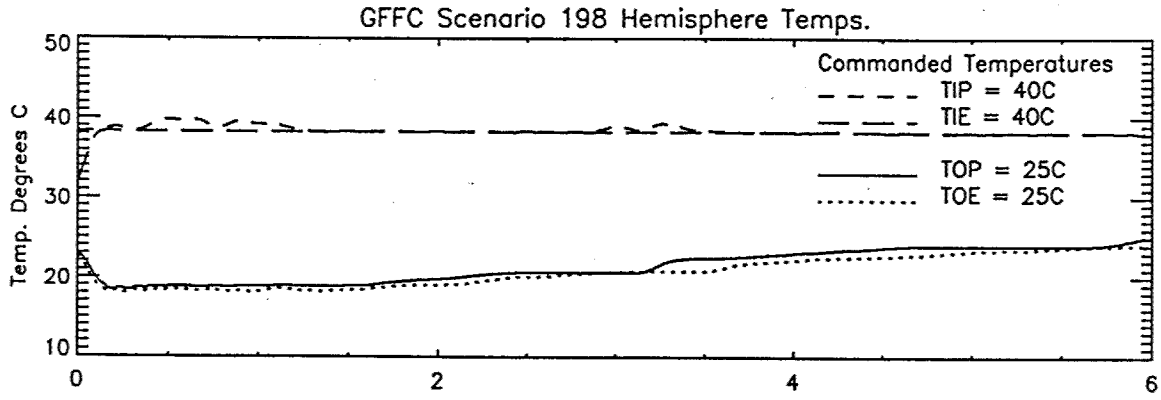
GFFC Scenario 198 Hemisphere Temps.
Commanded Temperatures
TIP = 40C
TIE = 40C
TOP = 25C
TOE = 25C
Temp. Degrees C
50
40
30
20
10
0
2
4
6

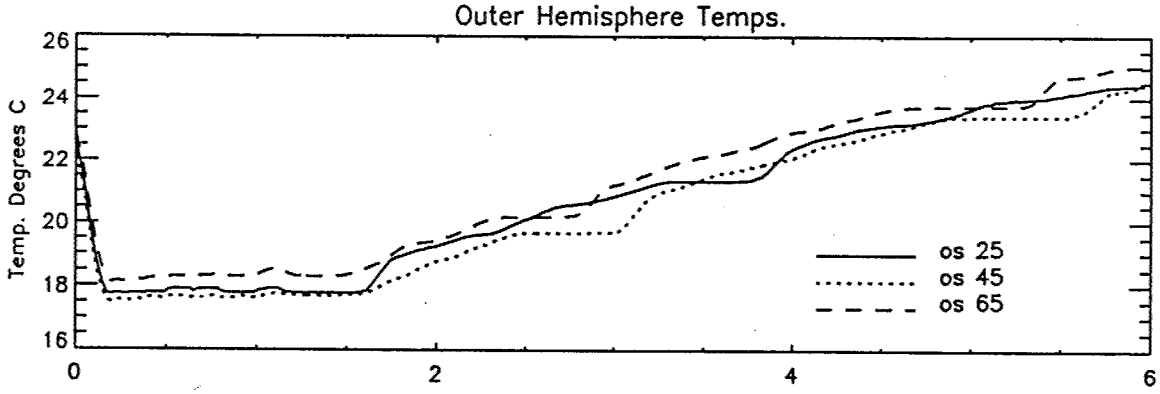
Outer Hemisphere Temps.
os 25
os 45
os 65
Temp. Degrees C
26
24
22
20
18
16
0
2
4
6

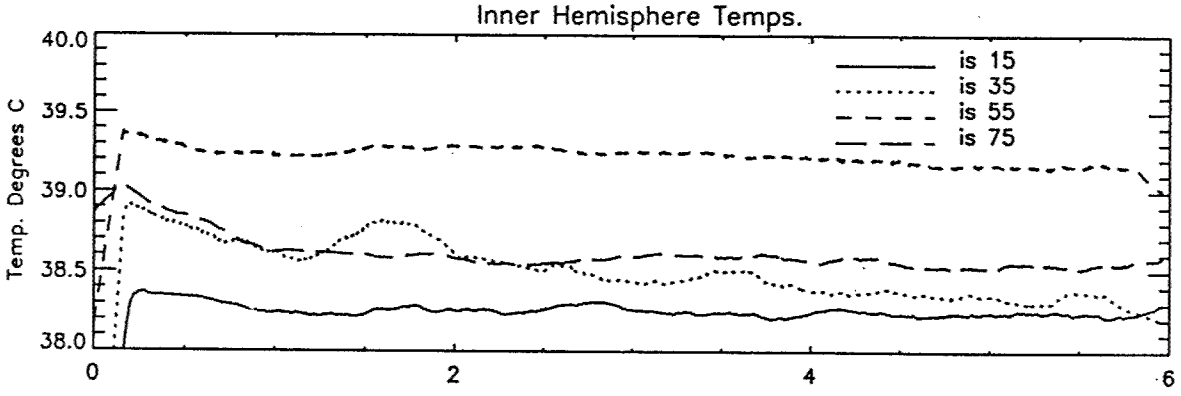
Inner Hemisphere Temps.
is 15
is 35
is 55
is 75
Temp. Degrees C
40.0
39.5
39.0
38.5
38.0
0
2
4
6

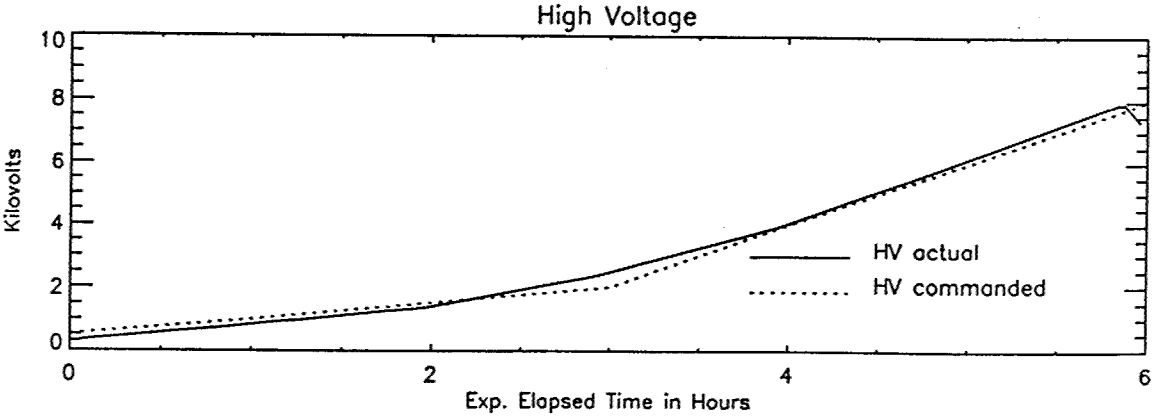
High Voltage
HV actual
HV commanded
Kilovolts
10
8
6
4
2
0
0
2
4
6
Exp. Elapsed Time in Hours

APPENDIX 2

UNWRAPPING USML-2 IMAGES ONTO A FULL HEMISPHERE

APPENDIX - 2: GENERATION OF 360 DEGREE LONGITUDE VISUALIZATIONS FROM THE GFFC IMAGERY.

An outline of the mapping routine used to generate the full hemispherical flowfields:

For certain camera actions it is possible to extract a sequence of eight images separated longitudinally by 45° on the spherical convection cell. If the temporal evolution of the observed flow structures is not too rapid during the sampling period for this sequence, then the images may be used to produce a composite image depicting the flowfield across the entire hemisphere as seen from the pole.

The developed image mapping scheme consists of three stages. In the first stage each recorded image is projected back onto the surface of the sphere, thereby defining the flow structures as a function of longitude and latitude at that radial location. This process utilises the nature of the wrap around optics used to record the images. These optics cause the paths of all the observed radially propagating rays to become refracted on emerging from the convection cell, so that they are parallel to the optical axis of the camera. Then in the second stage, the above results are used to map each image in order to attain its view as seen from the pole. Since orthographic projections cause an excessive amount of image distortion near the equator, a mapping routine that generated polar plots in which radial distance was proportional to latitude was implemented. An example of one such transformation is given in Fig. 1 b. Lastly, in the third stage the eight mapped images within the sequence are overlaid to produce the final composite. In order to produce a smooth transition between images at successive longitudinal locations a weighted mask was applied to each. The effect of this mask is to smoothly vary the intensity of the image azimuthally from a maximum at its centre to zero at a position of $\pm 45°$. The weighting function was chosen such that the total weight of all the individual contributions at any location was equal to 1.0, thus ensuring a uniform illumination across the composite. An example of one such masked image together with the final resulting composite are shown in Fig. 1 c+d respectively.

The operation of the above scheme was validated by observing its effect on the lines of equal latitude etched onto the surface of the glass convection cell. As can be seen from the results, especially in cases highlighting north to south intensity gradients, these marks are faithfully mapped onto circles of corresponding latitudes.

Figures 2 - 7, following, illustrate full-view maps obtained for several of the runs in table 2 of the summary section.

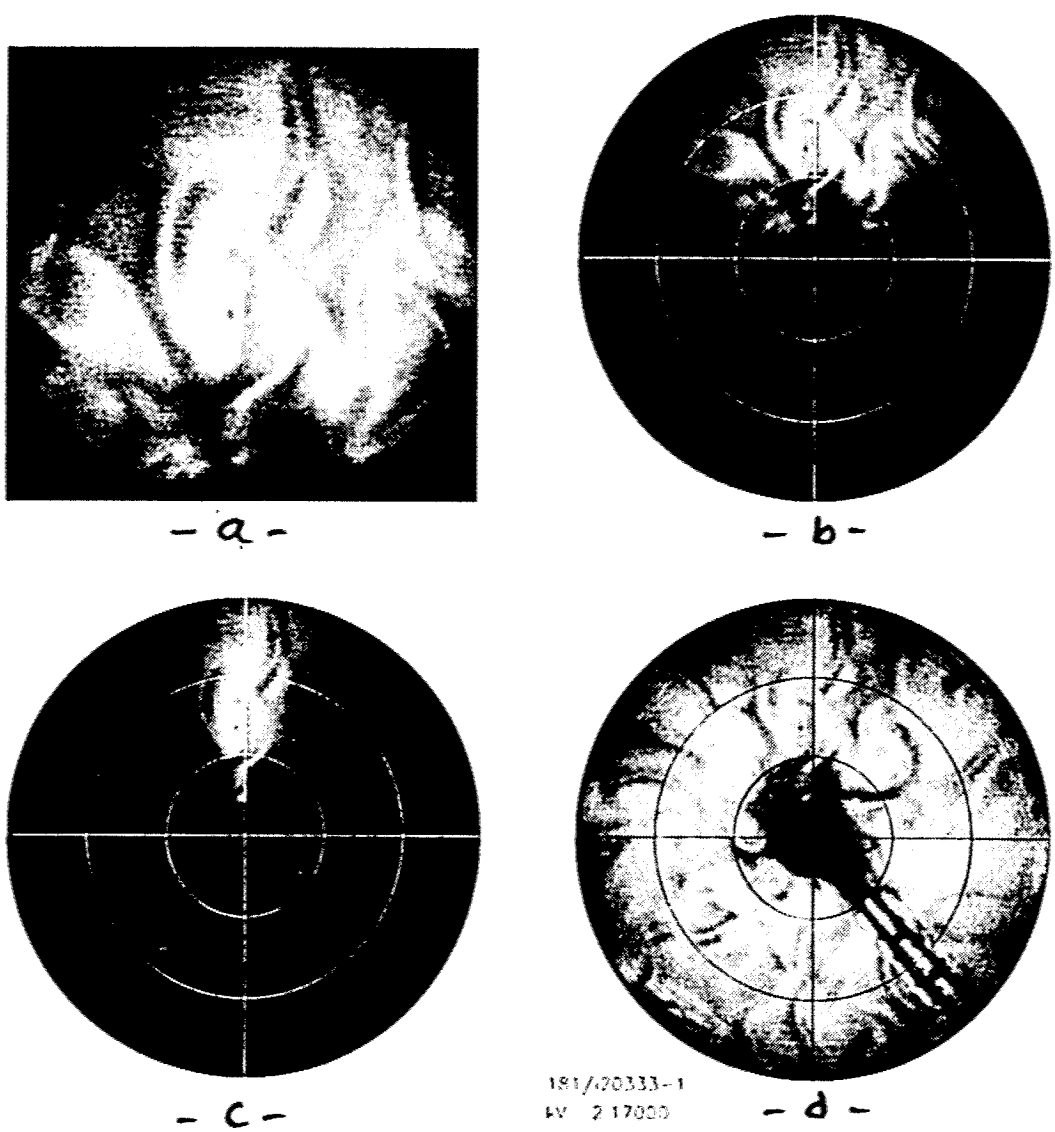

Figure 1. a) Recorded image; b) Mapped image; c, Masked image; d, Final Composite.

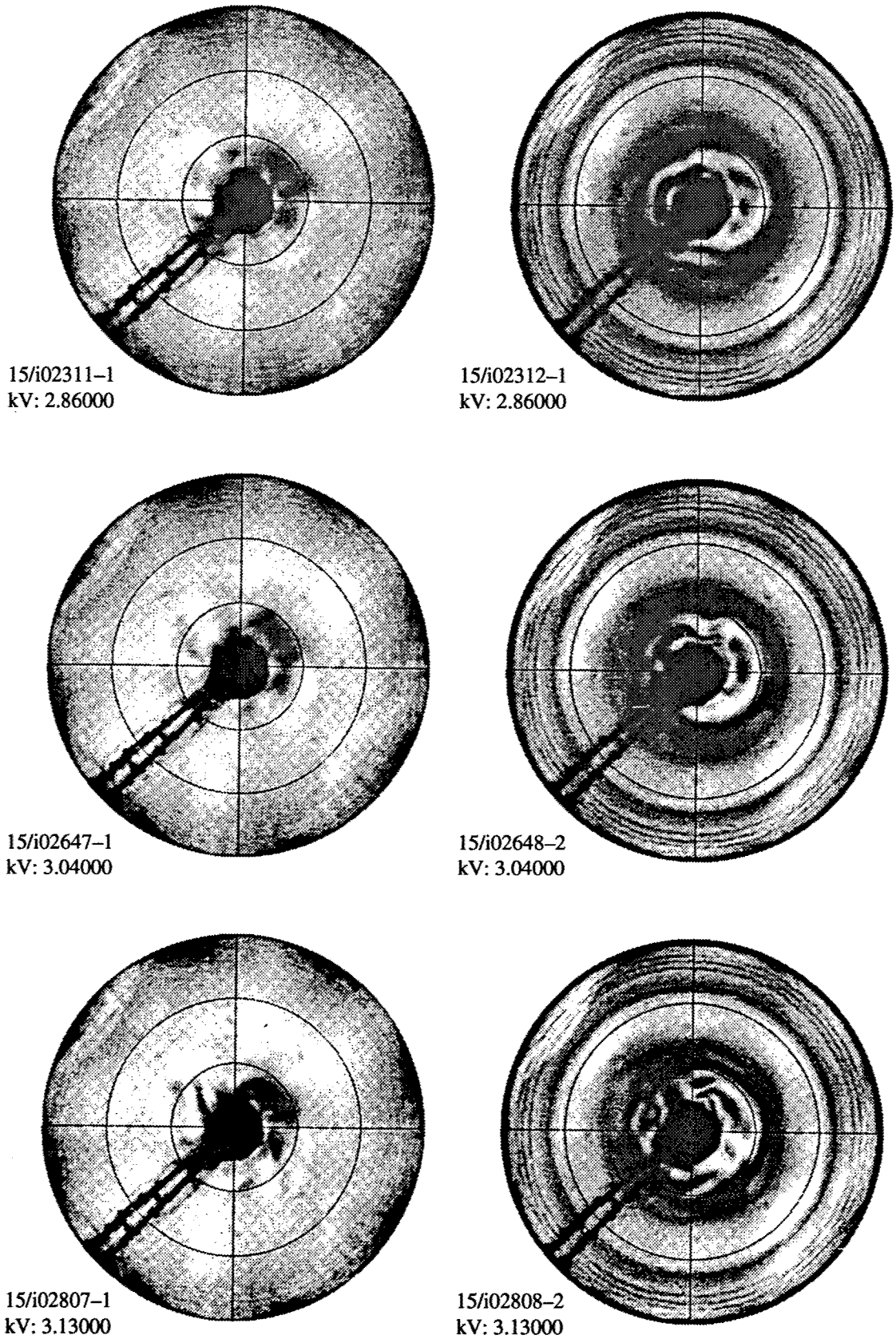

Figure 2. Unwrapped views of convection in scenario 15 with values of the voltage as indicated. Left columns are N–S fringes (sensitive to E–W gradienst) and the right columns show E–W fringe setting (sensitive to N–S gradients). Note the development of banana cell aligned with the rotation axis, following onset of polar disturbances. The applied kilovoltage is shown for each pair of images.

15/i03203-1
kV: 3.35000

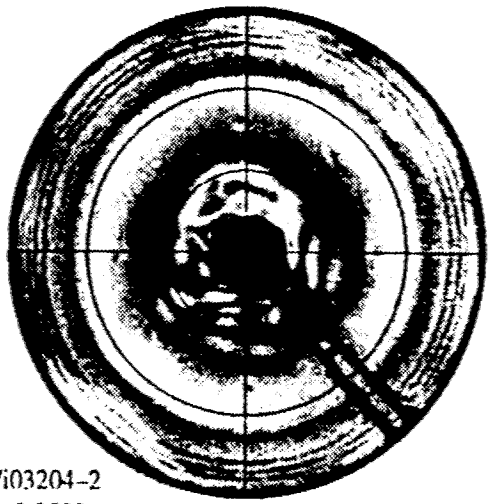

15/i03204-2
kV: 3.3500

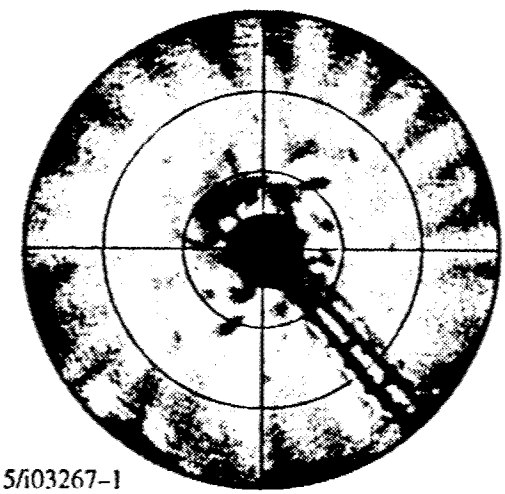

15/i03267-1
kV: 3.36000

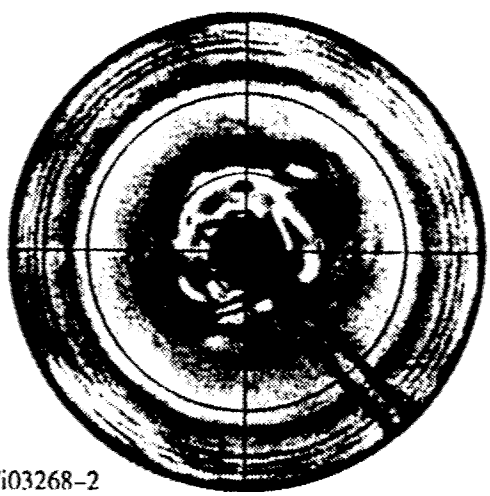

15/i03268-2
kV: 3.36000

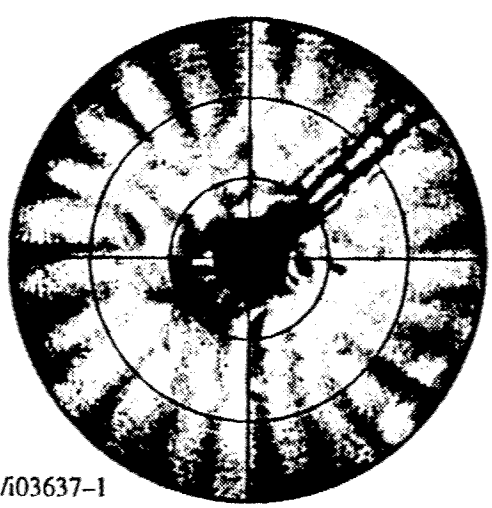

15/i03637-1
kV: 3.62000

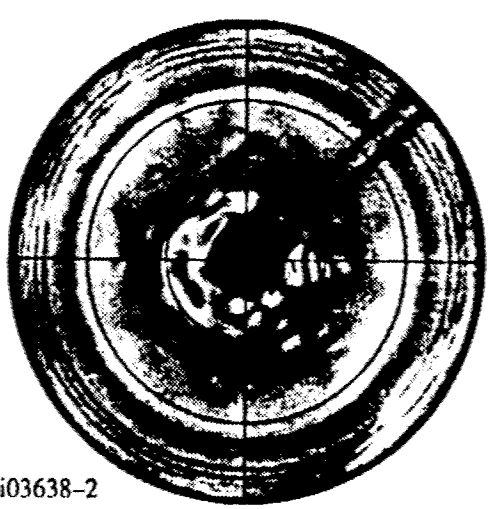

15/i03638-2
kV: 3.62000

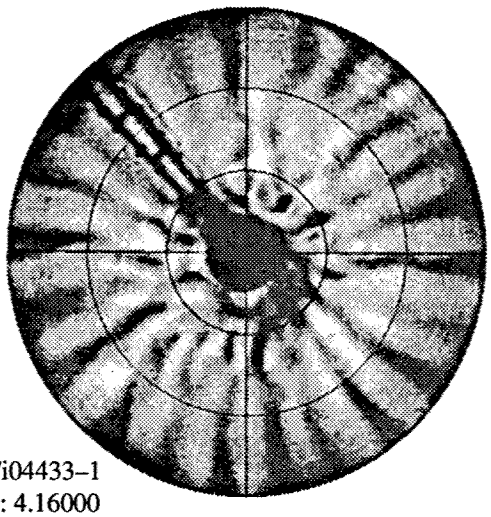

15/i04433–1
kV: 4.16000

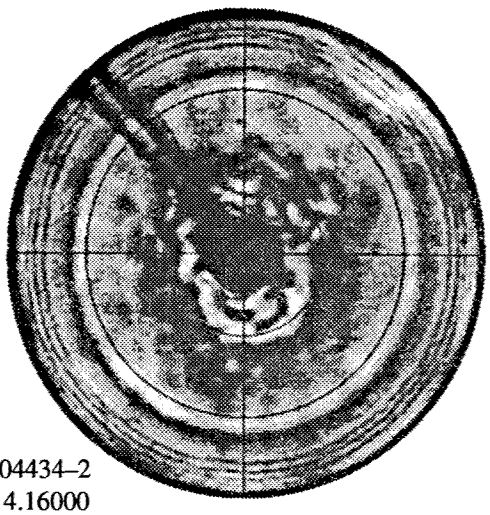

15/i04434–2
kV: 4.16000

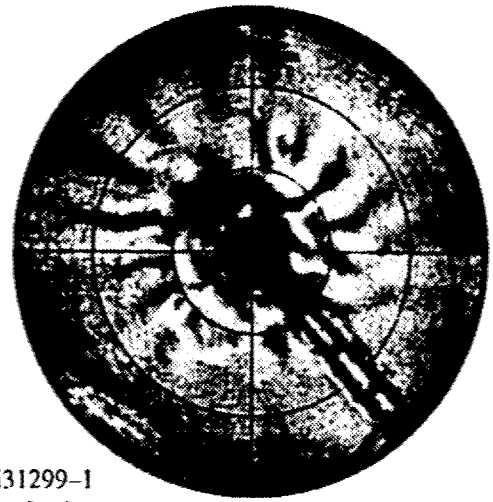

17/i31299–1
Time:2 min
kV:1.93000

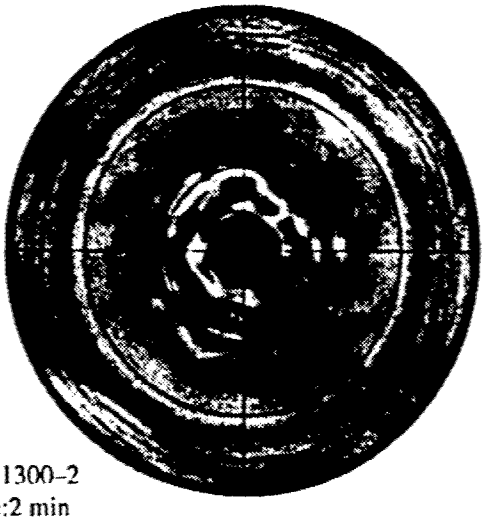

17/i31300–2
Time:2 min
kV:1.93000

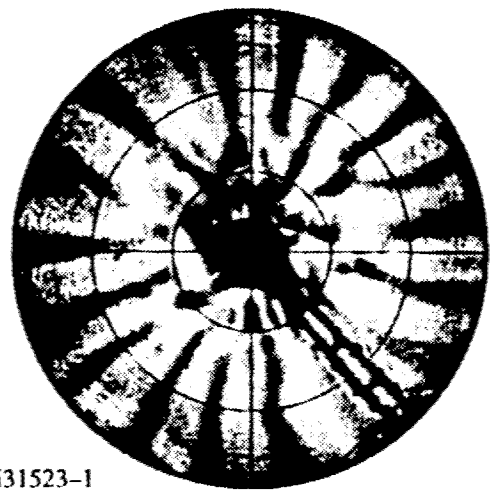

17/i31523–1
Time:17 min
kV:2.08000

17/i31524–2
Time:17 min
kV:2.08000

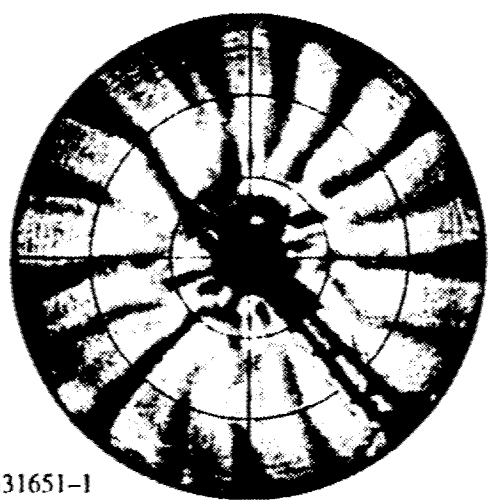

17/i31651–1
Time:26 min
kV:2.16000

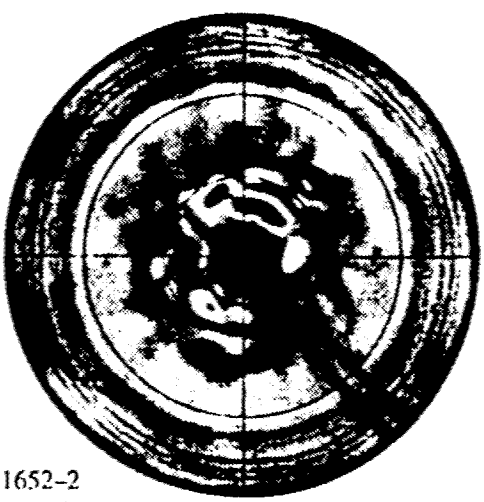

17/i31652–2
Time:26 min
kV:2.16000

Figure 3. Unwrapped views of convection in scenario 17 with values of the voltage as indicated. Left columns are N–S fringes (sensitive to E–W gradients) and the right columns show E–W fringe setting (sensitive to N–S gradients). Convection is similar to figure 2, except note that the banana wavenumber is lower.

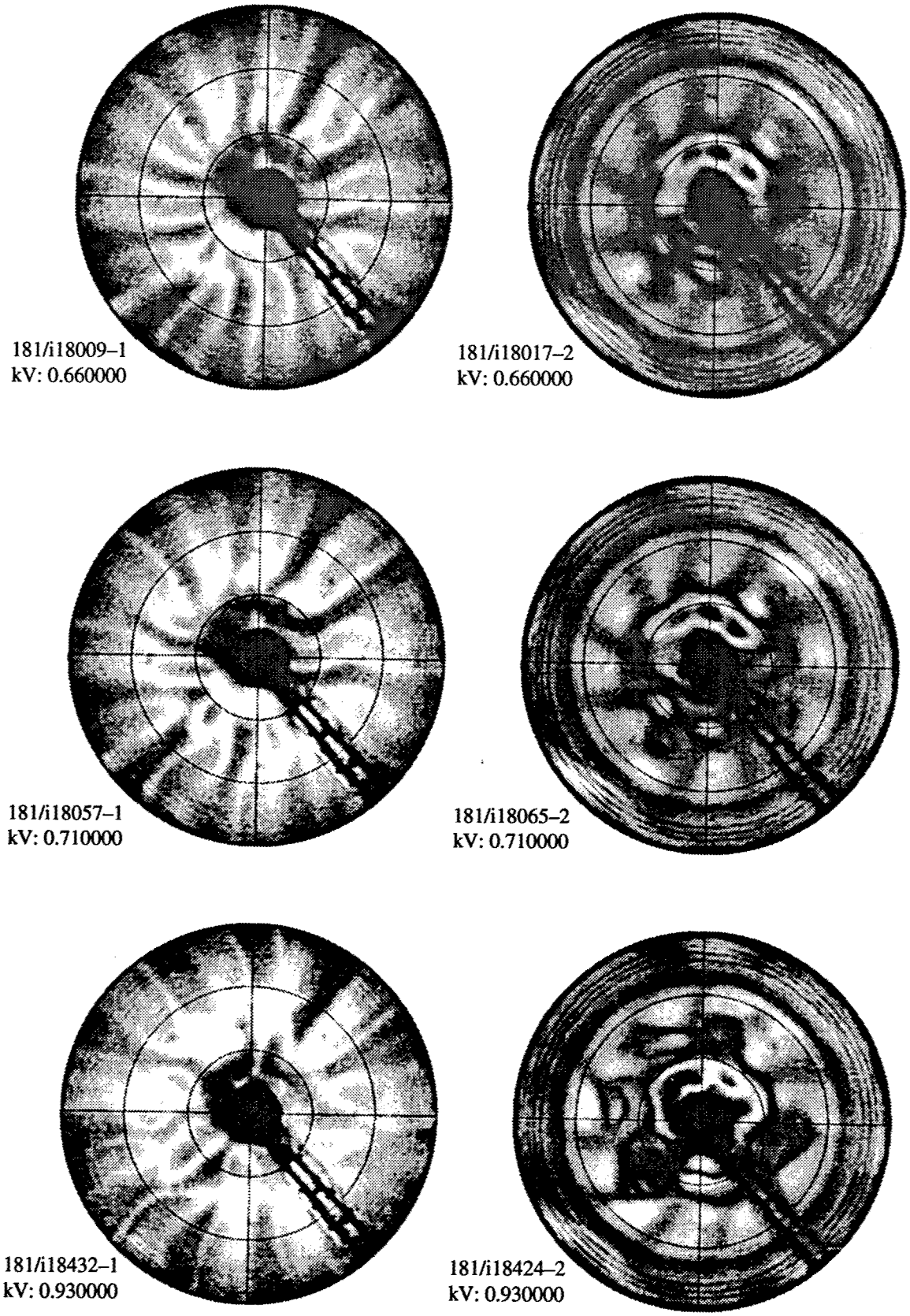

Figure 4. Unwrapped views of convection in scenario 181 with values of the voltage as indicated. Left columns are N–S fringes (sensitive to E–W gradients) and the right columns show E–W fringe setting (sensitive to N–S gradients). Although the rotation period is long compared with figs. 3 and 2 (16 seconds, vs. 4 and 2 respectively), banana cells still form, although the polar disturbances are more pronounced. As the voltage is increased the polar modes remain beautifully organized and stronger than the banana cells.

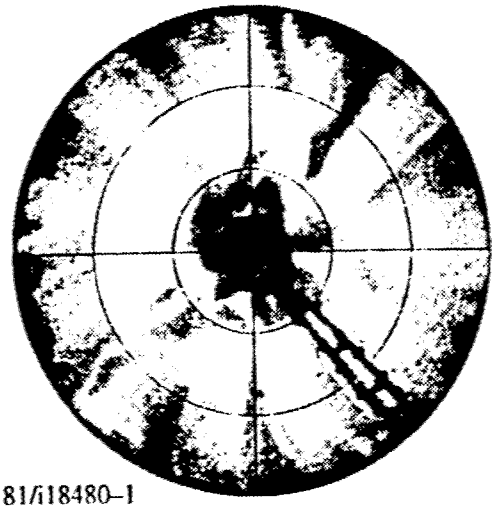

181/i18480–1
kV: 0.960000

181/i18472–2
kV: 0.96000

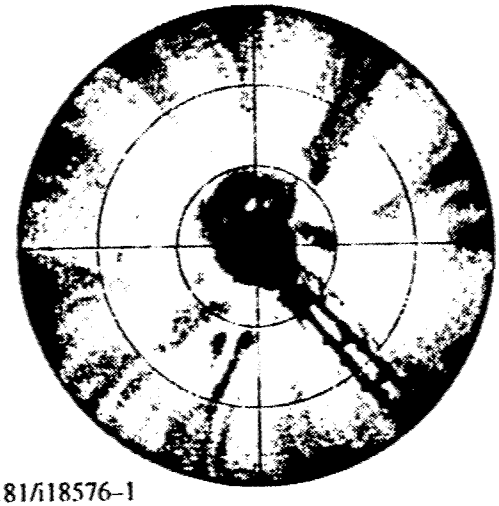

181/i18576–1
kV: 1.00000

181/i18584–2
kV: 1.03000

181/i18832–1
kV: 1.18000

181/i18840–2
kV: 1.18000

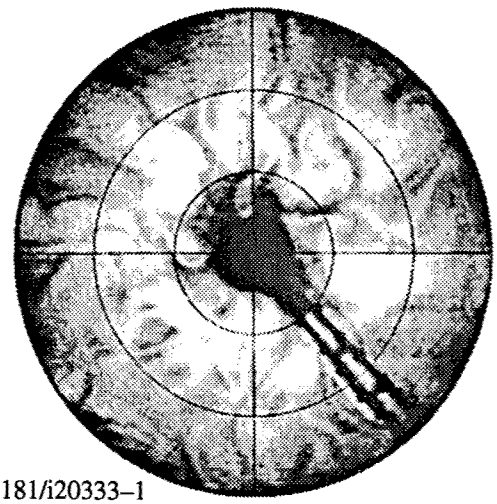

181/i20333–1
kV: 2.17000

181/i20325–2
kV: 2.17000

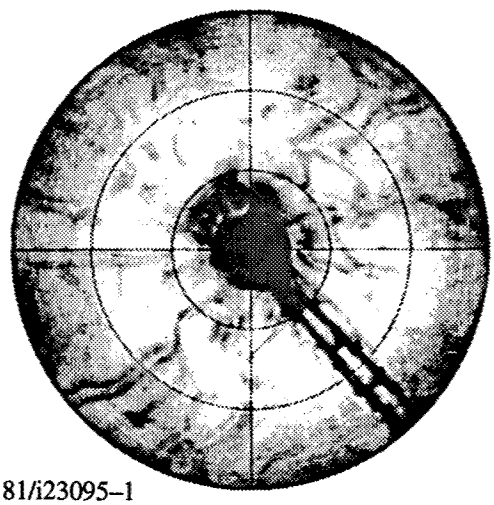

181/i23095–1
kV: 4.65000

181/i23087–2
kV: 4.65000

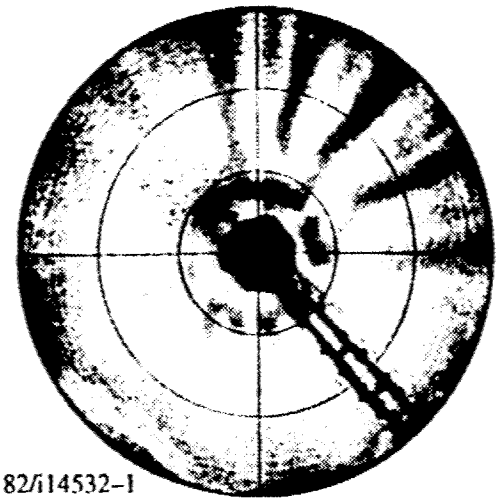

182/i14532–1
kV: 1.00000

182/i14533–2
kV:1.00000

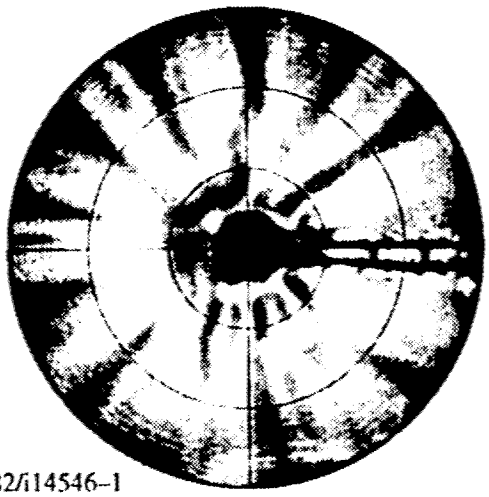

182/i14546–1
kV: 1.04000

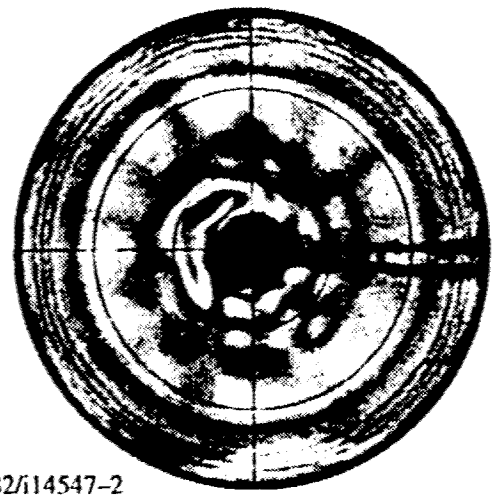

182/i14547–2
kV: 1.04000

182/i14592–1
kV: 1.18000

182/i14593–2
kV: 1.18000

Figure 5. Unwrapped views of convection in scenario 182 (8 second period) with values of the voltage as indicated. Left columns are N–S fringes (sensitive to E–W gradients) and the right columns show E–W fringe setting (sensitive to N–S gradients). The response is qualitatively similar to figure 4.

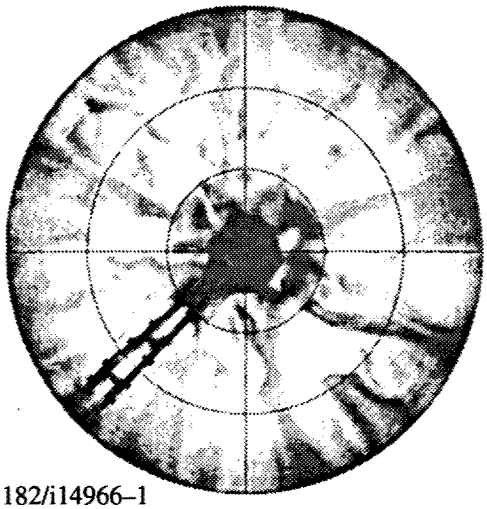

182/i14966–1
kV: 2.26000

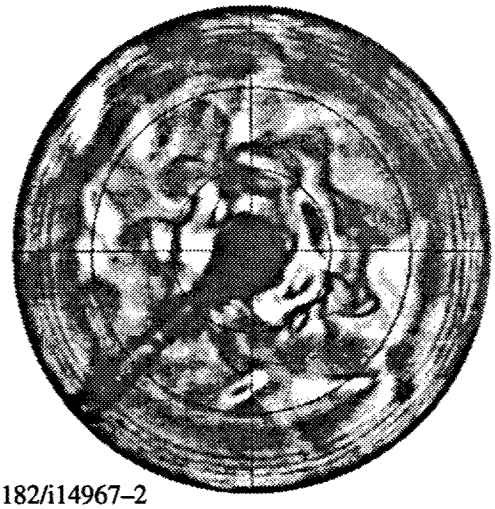

182/i14967–2
kV: 2.26000

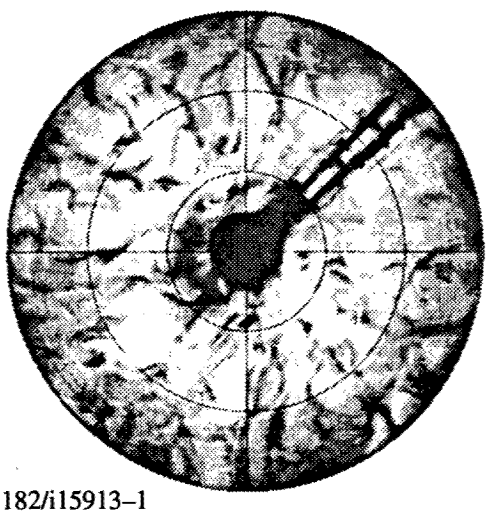

182/i15913–1
kV: 6.12000

182/i15914–2
kV: 6.12000

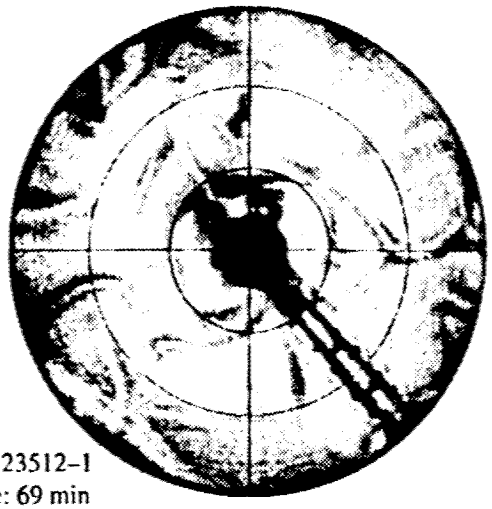

194/i23512-1
Time: 69 min
kV: 1.46000

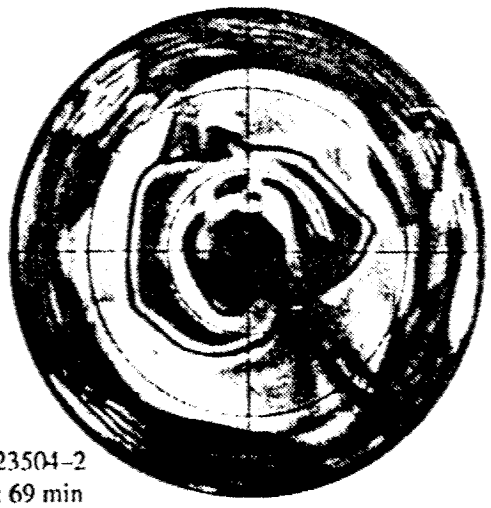

194/i23504-2
Time: 69 min
kV: 1.46000

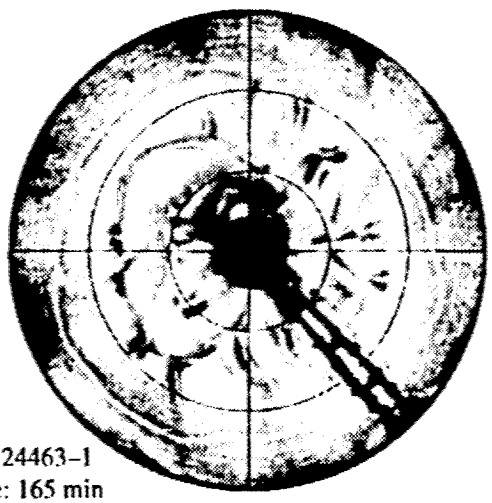

194/i24463-1
Time: 165 min
kV: 3.13000

194/i24471-2
Time: 165 min
kV: 3.16000

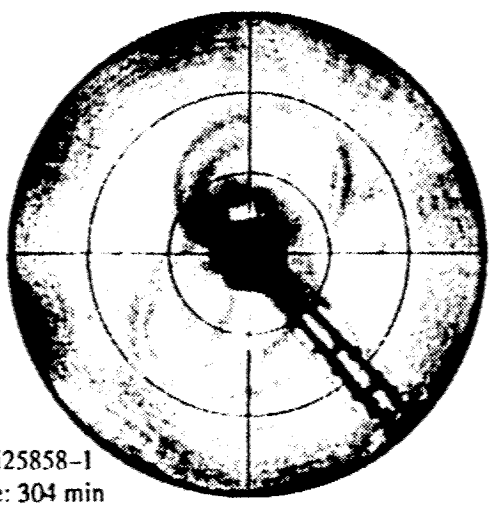

194/i25858-1
Time: 304 min
kV: 1.26000

194/i25866-2
Time: 304 min
kV: 1.26000

Figure 6. Unwrapped views of convection in scenario 194 (48 second period) with values of the voltage as indicated. Left columns are N–S fringes (sensitive to E–W gradients) and the right columns show E–W fringe setting (sensitive to N–S gradients). Note the mixture of axisymmetric convection and NS striations that evolves into strong steady wavenumber 2 mode as kV is raised.

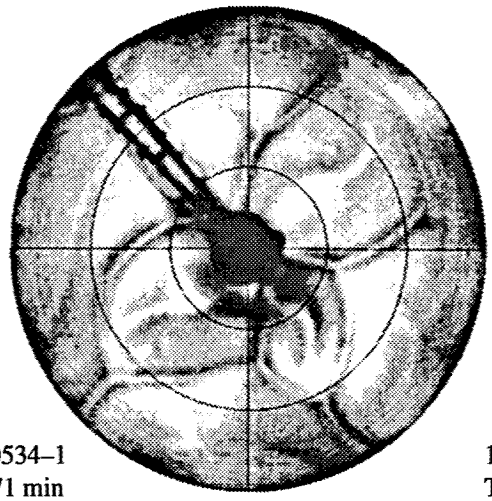

195/i00534–1
Time: 71 min
kV: 1.46000

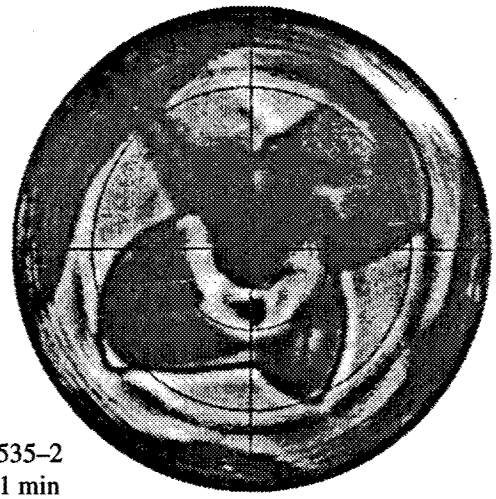

195/i00535–2
Time: 71 min
kV: 1.46000

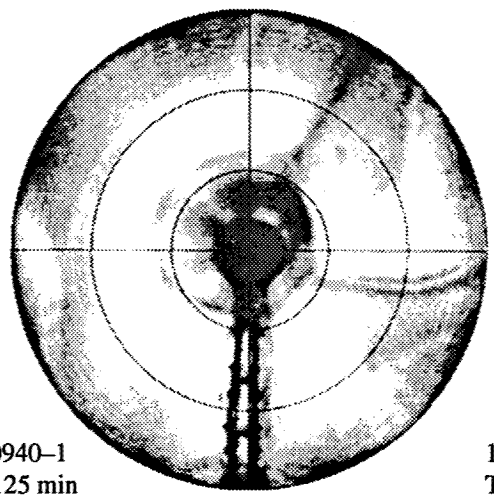

195/i00940–1
Time: 125 min
kV: 1.88000

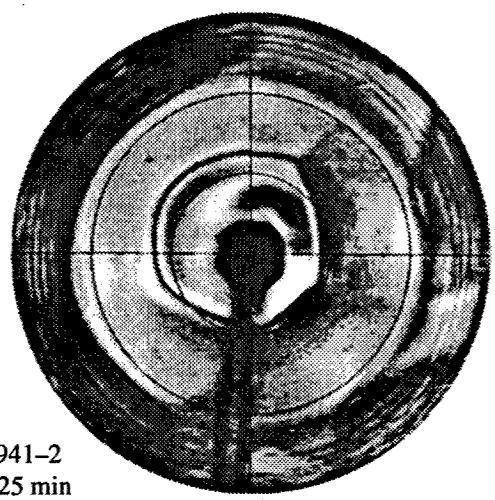

195/i00941–2
Time: 125 min
kV: 1.88000

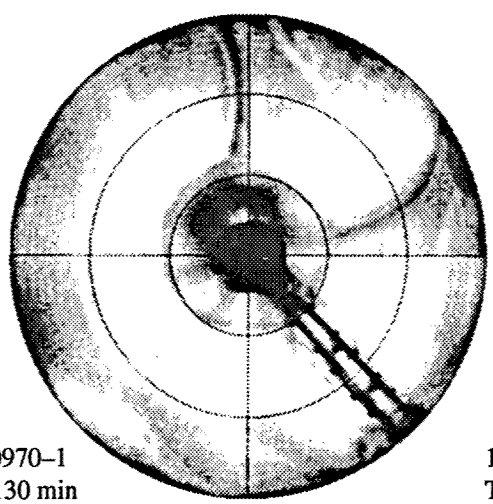

195/i00970–1
Time: 130 min
kV: 2.01000

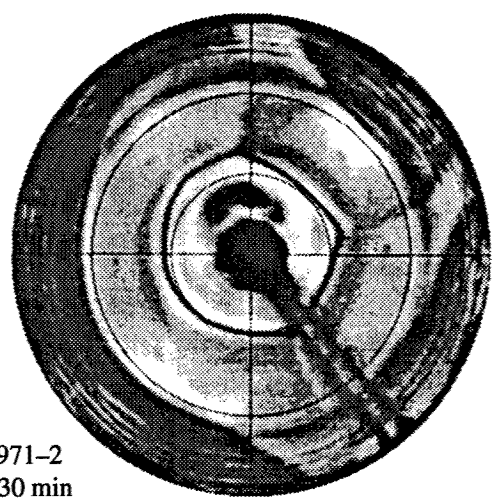

195/i00971–2
Time: 130 min
kV: 2.01000

Figure 7. Unwrapped views of convection in scenario 195 (128 second period) with values of the voltage as indicated. Left columns are N–S fringes (sensitive to E–W gradients) and the right columns show E–W fringe setting (sensitive to N–S gradients). Of particular interest is the polar, nearly axisymmetric cell and the steady pair of N–S convection rolls extending from the polar cell to the equator. Note that for kV above about 2, it is no longer possible to unwrap the images because of strong time dependence.

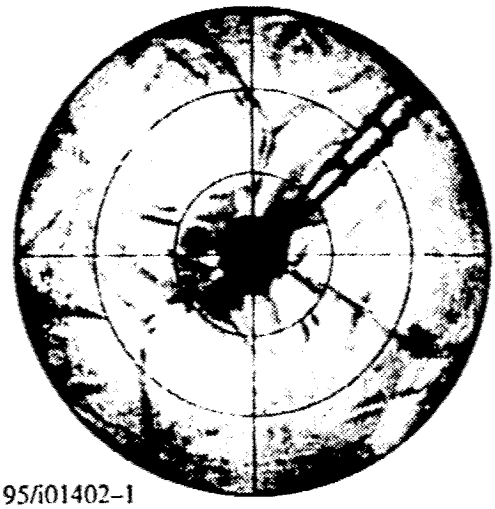

195/i01402-1
Time: 187 min
kV: 2.94000

195/i01403-2
Time: 187 min
kV: 2.9400

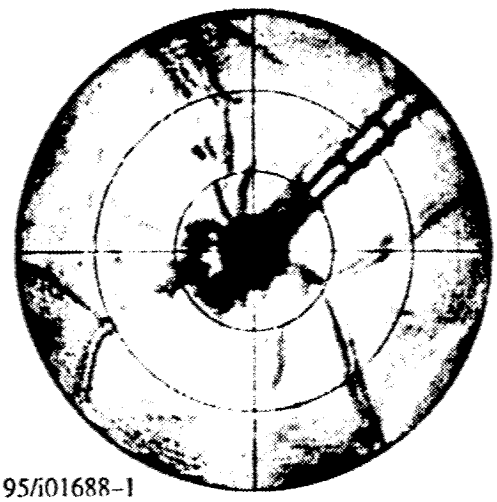

195/i01688-1
Time: 225 min
kV: 1.64000

195/i01689-2
Time: 225 min
kV: 1.64000

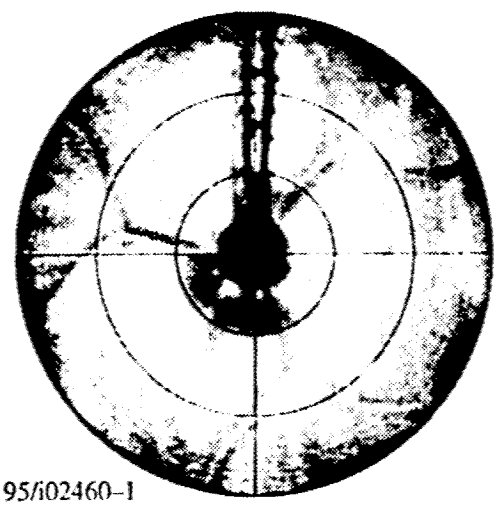

195/i02460-1
Time: 328 min
kV: 0.890000

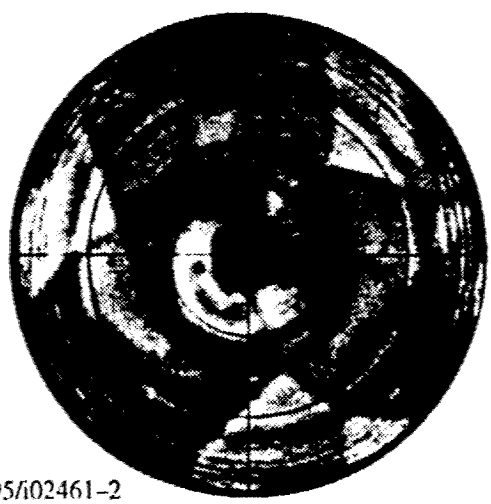

195/i02461-2
Time: 328 min
kV: 0.890000

APPENDIX 3

DETAILED COMPARISON OF GFFC RESULTS WITH VARIOUS COMPUTATIONAL SIMULATIONS

Comparisons to numerical simulations:

Two numerical models were used to make some general predictions of GFFC behavior before the USML2 flight and then to compare with actual GFFC results after the flight. The models are set up with the GFFC spherical geometry, electro-gravity, and the actual fluid parameters. Both models attempt to be direct numerical simulations of the experiment in that they have no additional dissipation beyond Laplacian molecular diffusion. A DNS model must have sufficient spatial resolution (i.e. a large enough number of grid points or spectral modes) so that nothing except molecular diffusion processes occur between the grid points in finite-difference formulation or at larger than the highest modeled wavenumber in spectral formulation. In addition, smaller spatial resolution implies smaller temporal resolution for numerical stability. Hence the more turbulent the flow, with small high-speed flow structures, the more expensive the computation. As shown below, the numerical model results are most like the GFFC results near convective onset as expected.

The model by Miller and Leslie (Miller, et. al., 1992) is 3-dimensional finite-difference in latitude and radius, and spectral in longitude. The post-flight runs discussed below were run with 30 radial points on a stretched grid that gives more points in the boundary layers, 60 latitudinal points and 45 longitudinal waves. The boundary conditions are able to mimic the temperature boundary conditions of the GFFC as well as the no-slip insulating boundary at the equator. The model by Glatzmaier (Glatzmaier, 1983 and Hart, et al. 1986) is spectral in latitude and longitude with a slightly better spatial resolution, and Chebyshev-spectral in radius. The spectral technique is numerically more accurate but does not implement the no-slip equatorial boundary of the GFFC apparatus. Instead, Glatzmaier requires symmetric solutions between northern and southern hemisphere, equivalent to a free-slip velocity boundary condition there.

Post-flight comparisons to individual scenarios:

Example 1) Solar case, 4 second rotation period, no intended latitudinal temperature gradient.

The voltage and temperature inputs to the numerical model were obtained from the GFFC experiment temperature and voltage readouts recorded on the 16 mm film (scenarios 145, 112, and 17). These conditions were simplified slightly (for numerical convenience) from the actual conditions of the USML-2 runs (see Appendix 1 for details on the actual temperature distributions) to:

$T_{inner} = 38.5C$

T_{outer} = 18C from 0 to 70 minutes, then a linear amp 18 - 24C over 70 - 200 minutes, and finally a linear ramp 24 - 26C during 200 - 360 minutes.

Linear voltage ramp from 0.806 - 4.95 kV during 0 - 230 minutes, then a ramp of 4.95 - 9.50 kV during 230 - 360 minutes.

Experiment:

In this scenario as time progressed the forcing voltage increased in the GFFC experiment, and convection began at voltage 1.57 kV near the pole with a longitudinal wavenumber of about 17. This pattern traveled prograde at about .0035 radians per second. When the voltage increased at 1.85 kV we get the typical north-south aligned "banana cells". These banana cells of wavenumber ~17 traveled prograde at speed ?. At slightly larger voltage the banana cells lengthened toward the pole and interacted with the polar convection. Further increase in voltage saw the polar convection region extend equatorward and erode the banana cell pattern. At the same time these equatorial cells became nonlinear in amplitude, decreased in average wavenumber, had energy in a wider range of wavenumbers and traveled more slowly. Examples of the observed patterns for increasing high voltage values are shown in Figure 1. The unwrapping technique was used to reconstruct the spatial dependence of the full hemispheric pattern from successive images taken every 1/8 revolution. In 1a the polar convection has begun and the equatorial bananas are just starting in the upper-left quadrant. By 1c the banana cells are interacting with the polar convection.

Miller-Leslie Model:

Two example images from the simulation are shown in Figure 2. In both, the temperature is shown on a color scale which runs from blue to red to green to yellow from cold to hot. Recall that the GFFC images show either the north/south or east/west temperature gradient rather than temperature directly as in the model. The patterns are barotropic with depth, D. Figure 2a is near onset of the model banana cells and 2b has nonlinear bananas interacting with the polar convection. In Figure 3 time-longitude plots of temperature at mid-radius at latitudes of 66 and 15 degrees show the onset values and phase speeds of the polar and equatorial convection respectively. The polar convection begins in the model at 2.10 kV, significantly higher than observed in the experiment, with a prograde-traveling wavenumber 5 pattern. Within a few minutes this simple pattern breaks into a complicated set of convection rolls which move both the simple pattern becomes . At 2.12 kV the banana cell convection begins, closer to the observed onset. The pattern is a mixture of wavenumbers 18 and 19, also close to the experimental values. The prograde longitudinal phase speed starts rapid (~9.3 deg./min. at time = 75 min. and voltage = 2.16 kV) and as the amplitude grows and wavenumber shrinks, slows to ~5.3 deg./min. at time

= 85 min. and voltage = 2.34 kV). In summary, the model calculates the onset of polar convection at too large a voltage, does better with the equatorial convection onset, finds the onset banana cell wavenumber very well, and does ? with the phase speed of the banana cells. The decrease in wavenumber and phase speed of the banana cells for increasing high voltage is consistent with the GFFC observations.

Glatzmaier model:

This model calculates the onset at of equatorial convection at about 1.6 kV, before the polar convection begins. The free-slip boundary at the equator in this model presumably damps the convection there less. This onset voltage for bananas is close to but lower than that observed in the experiment but completely misses the initial polar convection mode. Figure 4 shows contour plots of temperature and vertical velocity at D=0.5 for this model. The onset wavenumber for the bananas, 18, is consistent with both GFFC and the other model. As the voltage increases to the range of 3 to 5 kV, this fully spectral model does a qualitatively better job than the M-L model, predicting more GFFC-like, higher horizontal wavenumber structures.

Example 2) Mantle convection case, looking for possible hysteresis, 48 sec rotation period, no intended latitudinal temperature gradient, high voltage ramping up, holding, up again, down, holding again at same value, and then down again.

The voltage and temperature inputs to the numerical model were obtained from the GFFC experiment temperature and voltage readouts recorded on the 16 mm film for scenario 194. These conditions were simplified slightly for numerical convenience to:

T_{inner} = 39C

T_{outer} = 18C from 0 to 70 minutes, then a linear amp 18 - 23C over 70 - 180 minutes, and finally a linear ramp 23 - 21C during 180 - 360 minutes.

Linear voltage ramp from 0.66 - 1.47 kV during 0 - 70 minutes,
constant voltage of 1.47 kV during 70 - 106 minutes,
linear voltage ramp from 1.47 to 3.49 kV during 106 - 175 minutes,
linear voltage ramp from 3.49 to 1.47 kV during 175 - 246 minutes,
constant voltage of 1.47 kV during 246 - 281 minutes,
linear voltage ramp from 1.47 to 0.64 kV during 281 - 360 minutes.

Experiment:

Preflight numerical simulations with the M-L model had predicted hysteresis could be observed in the slowly-rotating cases. Indeed, in the first half of this scenario when the voltage was increasing then held fixed and then increasing, structures like Figures 5a, d were observed

with long rolls which extended a large fraction of the pole-to-equator distance and a circumpolar ring at high latitudes. For larger voltage (above about 2.5 kV) higher wavenumber, shorter rolls were observed near the pole along with a low-latitude (~20 deg.) ring which had smaller scale rolls attached to it (Figures 5b, e). For decreasing voltage a very stable wavenumber 2 ring was observed (Figures 5c, f) rather than the high-latitude ring and north/south rolls. This wavenumber 2 structure propagated prograde. It is not clear from the GFFC data that the pattern during the two constant voltage times was truly statistically steady and thus hysteretic or whether the entire run was a very long transient. Certainly the flow pattern was qualitatively different for increasing or decreasing high voltage.

Miller-Leslie Model:

The convection began right away in the simulation just as in the scenario 194 experiment, with an unsteady meandering of convection rolls that weren't obviously affected by the slow rotation. During the first constant voltage section, the pattern settled into a high-latitude ring with three long north/south rolls attached to it (Figure 6a). This pattern was stable and propagated. It is similar to the GFFC pattern of Figure 5a, d but more regular and more stable. At 2.0 kV the number of spokes declined to two and then at 2.1 kV to one. From 2.4 kV up to the maximum and then back down to the 2nd holding voltage at 1.46 kV the convection pattern looked like Figure 6b with a cool ring at mid-latitude and hot ring at high latitude and small-scale structures on each. Both rings and the waves on them are time-dependent. This pattern is reminiscent of Figures 5b, e but differs in the position of the rings and in the smallness of the other rolls. Furthermore, after less than 10 modeled minutes in the 2nd holding voltage, the entire convection pattern dissipated into axisymmetric flow rather than the stable 2 lobe structure of Figures 5c, f. In the GFFC experiment, the flow was convecting until the end of the run. Thus the modeled pattern is different for the two holding voltages, but not at all like the experiment. In general, the separate patterns are also more stable with less noise in the model and the transitions between patterns are shorter than in the experiment, so that separate flow regimes or qualitative patterns are more easily identified in the model.

Glatzmaier Model:

Qualitatively, the flow regimes are similar to GFFC during the first 2/3 of the run while the voltage increased, held steady, increased, and then decreased (Figures 7a-d). Again this model predicted axisymmetric flow before it was observed in the experiment, but not until the last hour of the scenario. The robust 2-lobed structure that dominated the 2nd half of the GFFC run was not calculated by this model Figures 7e), f).

Example 3) Mantle convection case, looking for possible hysteresis, 128 sec rotation period, no intended latitudinal temperature gradient, high voltage ramping up, holding, up again, down, holding again at same value, and then down again.

The voltage and temperature inputs to the numerical model were obtained from the GFFC experiment temperature and voltage readouts recorded on the 16 mm film for scenario 195. These conditions were simplified slightly for numerical convenience to:

T_{inner} = 39C

T_{outer} = linear ramp from 18 - 23C over 0 - 180 minutes, and then a linear ramp 23 - 22C during 180 - 360 minutes.

Linear voltage ramp from 0.66 - 1.46 kV during 0 - 53 minutes,
constant voltage of 1.46 kV during 53 - 105 minutes,
linear voltage ramp from 1.46 to 3.46 kV during 105 - 172 minutes,
linear voltage ramp from 3.46 to 1.46 kV during 172 - 230 minutes,
constant voltage of 1.46 kV during 230 - 279 minutes,
linear voltage ramp from 1.46 to 0.64 kV during 279 - 360 minutes.

Experiment:

Again, pre-flight numerical simulations had predicted that hysteresis might be observed in this slowly-rotating case. The patterns during the first half of the run until the end of the long voltage hold section (Figures 8a, g) are similar to the patterns observed in Scenario 194, long, unsteady, convection rolls which span most of the sphere from pole to equator. During the continuing voltage ramp from 1.46 to 3.5 kV (Figures 8b, c and 8h, i) the pattern switched to a high latitude ring with 2 spokes going all the way to the equator, very much like the pattern in the scenario 194 simulation by M-L (Figure 6a). Further into the scenario, the pattern became a soccer-ball of long convection rolls which persisted until the end of the run (Figures 8d-f, j-l). Within this basic pattern the larger voltage cases had more and sharper "noise" rolls. Like scenario 194, the convection pattern differed at like voltages for increasing and decreasing high voltage. Again it is not clear that either pattern was statistically steady or just stuck in a long transient.

Miller-Leslie Model:

The convection began right away in the simulation just as in the scenario 195 experiment, with an unsteady meandering of polar convection rolls that weren't obviously affected by the slow rotation (Figure 9a). During the first constant voltage section, the modeled flow became sub-critical and the pattern died away to axisymmetric flow (Figure 9b). When the convection began again at ~2.7 kV, the pattern of Figure 9c was maintained until early in the 2nd voltage holding

level at 1.46 kV when the convection died away to axisymmetric flow again. This simulation is quite different from the GFFC runs. Qualitatively, the modeled scenario 194 looks most like GFFC scenario 195.

Glatzmaier Model:

Again the flow regimes are similar to GFFC very early in the run. This model also predicts very weak convection and nearly axisymmetric flow beginning during the 2nd voltage holding section (Figure 10e).

Pre- and Post-flight Regime diagrams:

Before the USML2 flight, images from the Space Lab 3 GFFC experiment and both numerical models were combined in a plot in (Rayleigh number, Taylor number) space in order to have a basic idea of what flows we should expect. Figure 11 shows a post-flight version of such a diagram. The USML2 GFFC data is quite extensive for $H = 0$ (see table 2, lead section) and only 3 of the runs are shown. Comparable diagrams are shown in Figures 12-20 for SL3 data, the M-L model and the Glatzmaier model.

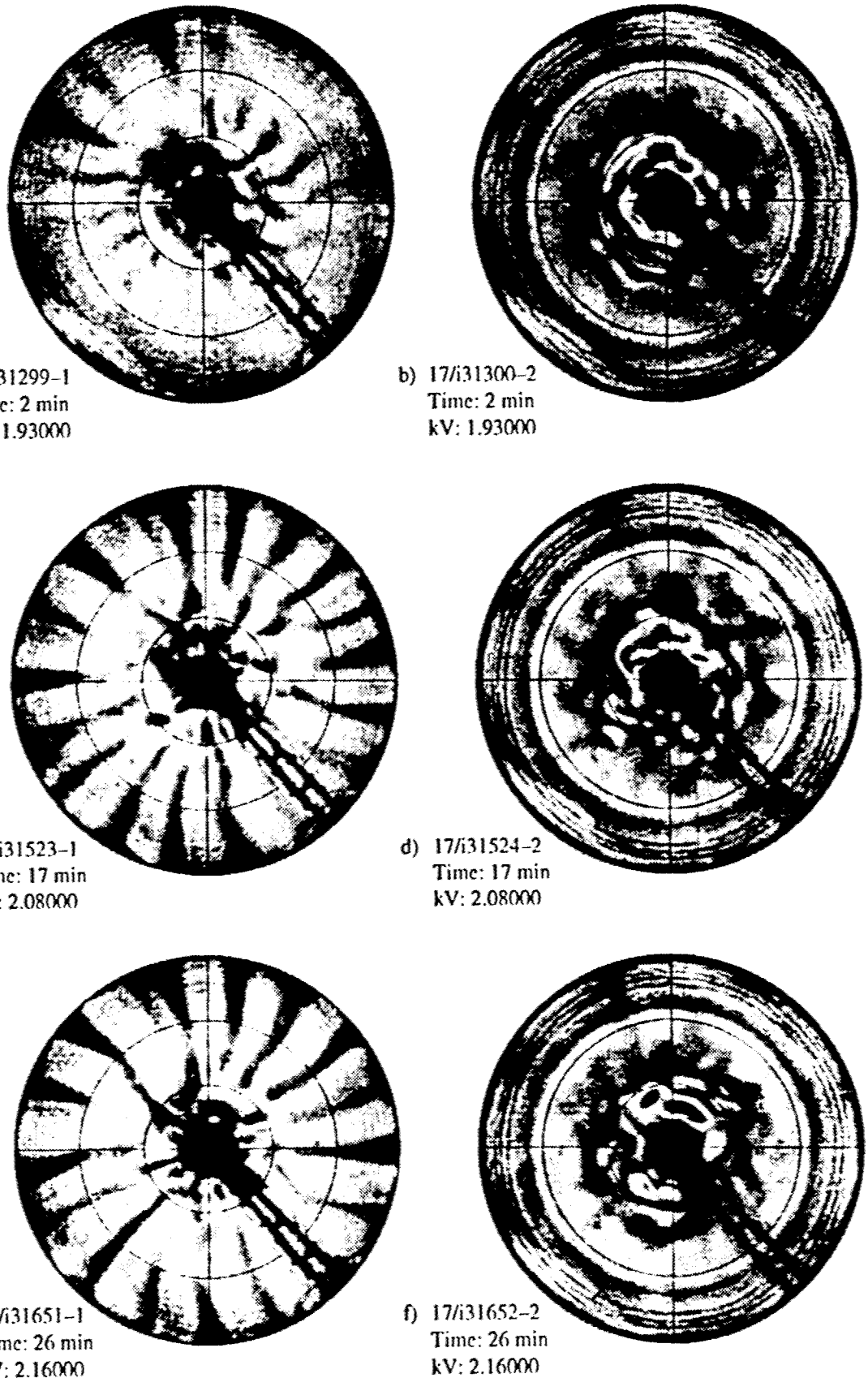

a) 17/i31299–1
Time: 2 min
kV: 1.93000

b) 17/i31300–2
Time: 2 min
kV: 1.93000

c) 17/i31523–1
Time: 17 min
kV: 2.08000

d) 17/i31524–2
Time: 17 min
kV: 2.08000

e) 17/i31651–1
Time: 26 min
kV: 2.16000

f) 17/i31652–2
Time: 26 min
kV: 2.16000

Figure 1. Unwrapping from 4 second rotation period, solar case, no latitudinal temperature gradient. Scenario 17 (same as 145, but with camera action 3). Grating in N/S orientation (a-c) and E/W orientation (d-f) . a,d) Polar convection with equatorial banana cells just beginning to grow. b, e) Banana cells with longitudinal wavenumber ~17. The pattern travels prograde (CW). Banana cells with longitudinal wavenumber ~16.

Figure 2) Miller-Leslie simulation of Scenario 145. *D* is the nondimensional height in the fluid layer of the temperature field shown. "Average" is the vertically averaged temperature field. This polar projection has latitude mapped linearly to radius as in the unwrapped GFFC images. **a)** 2.14 kV **b)** 2.41 kV.

(a)

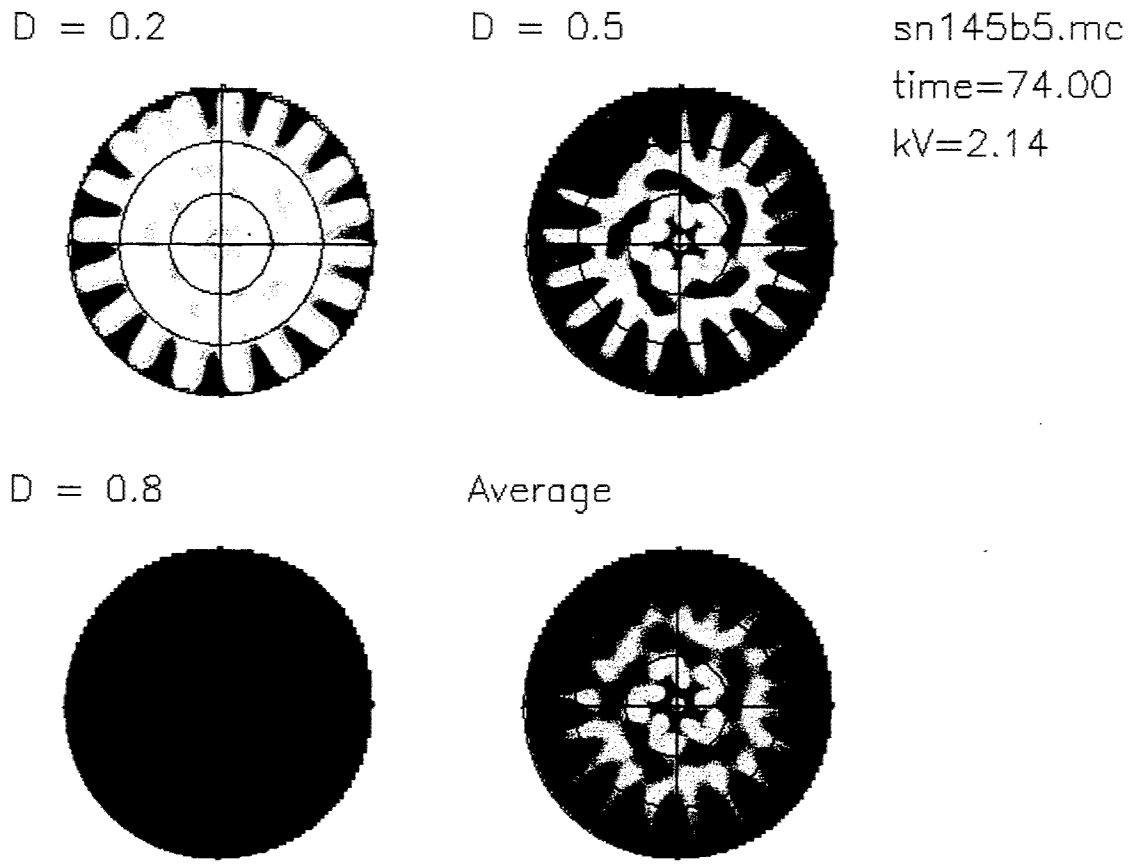

(b)

D = 0.2

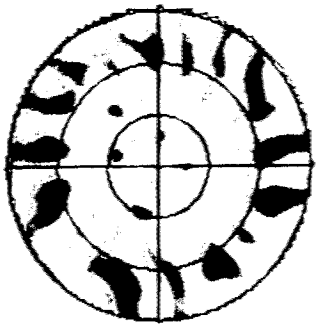

D = 0.5

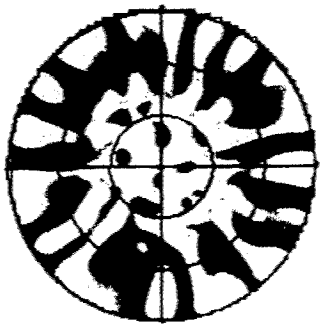

sn145b5.mc
time=89.00
kV=2.41

D = 0.8

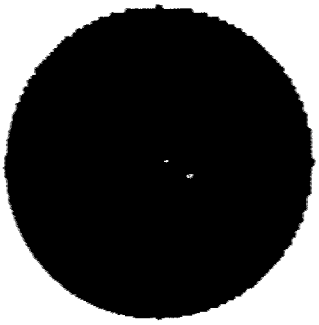

Average

Figure 3) Miller-Leslie simulation of Scenario 145. Temperature contours for all longitudes as a function of time at mid-height and latitude **a)** 66 deg. and **b)** 15 deg.

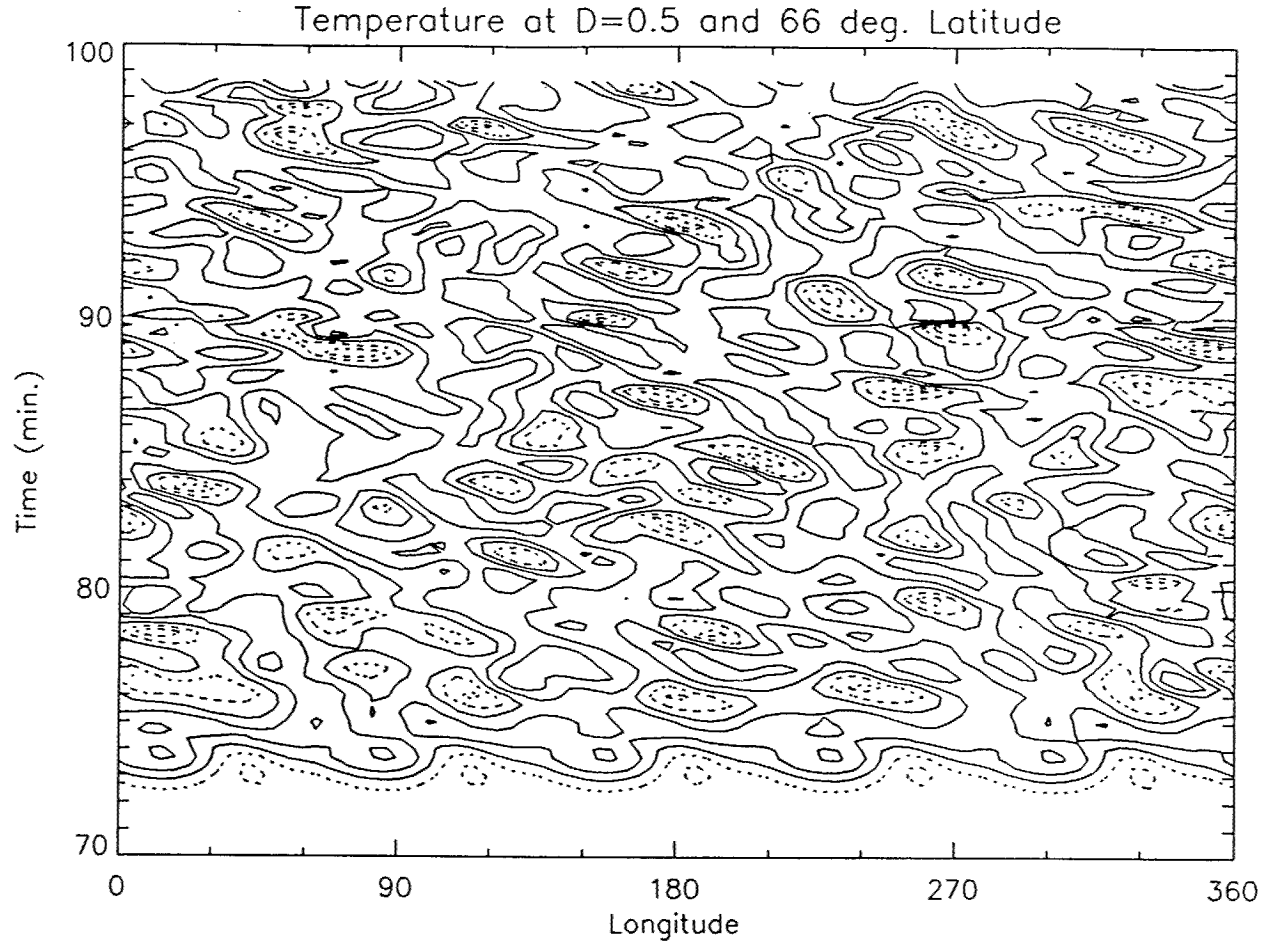

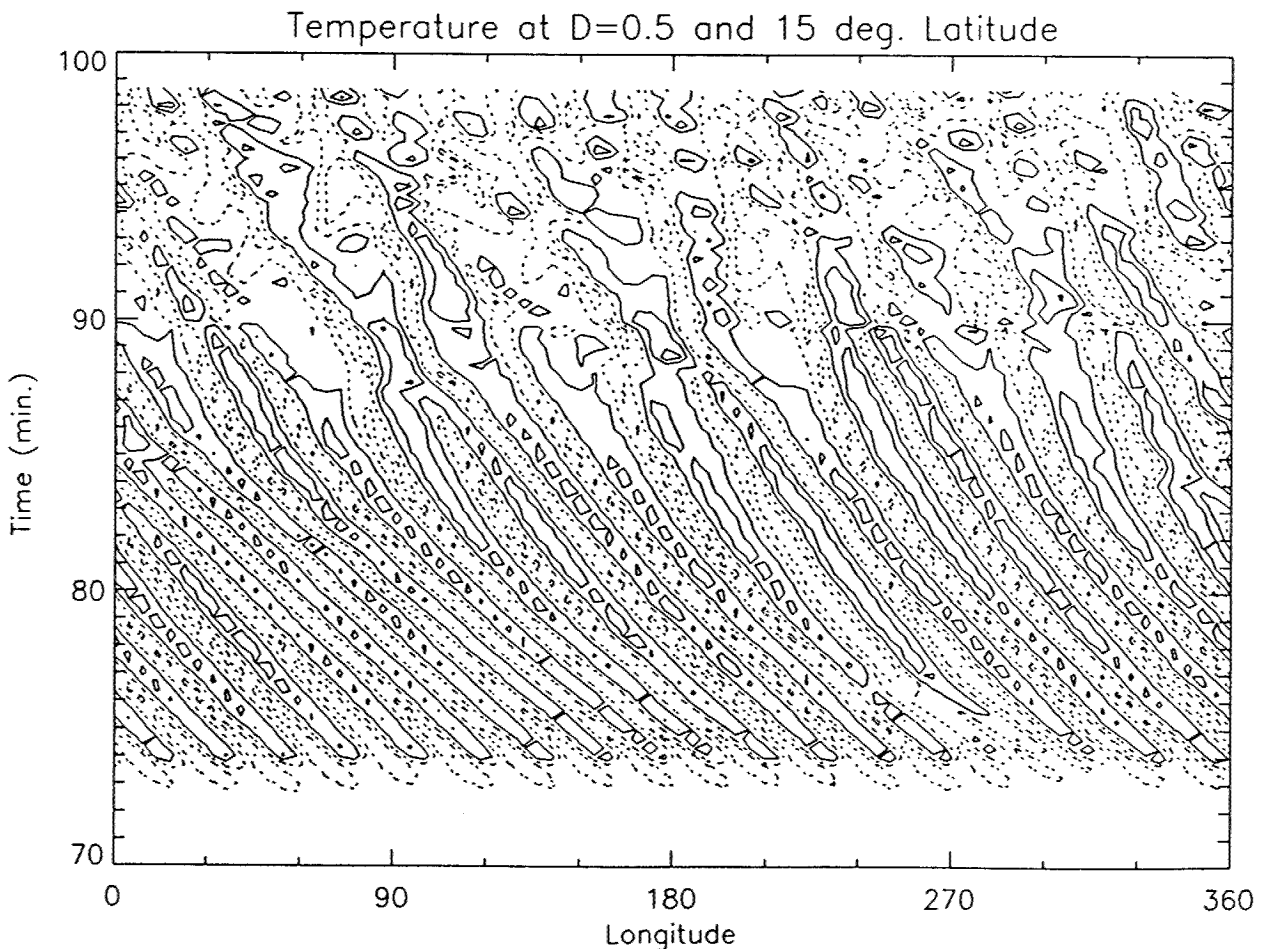

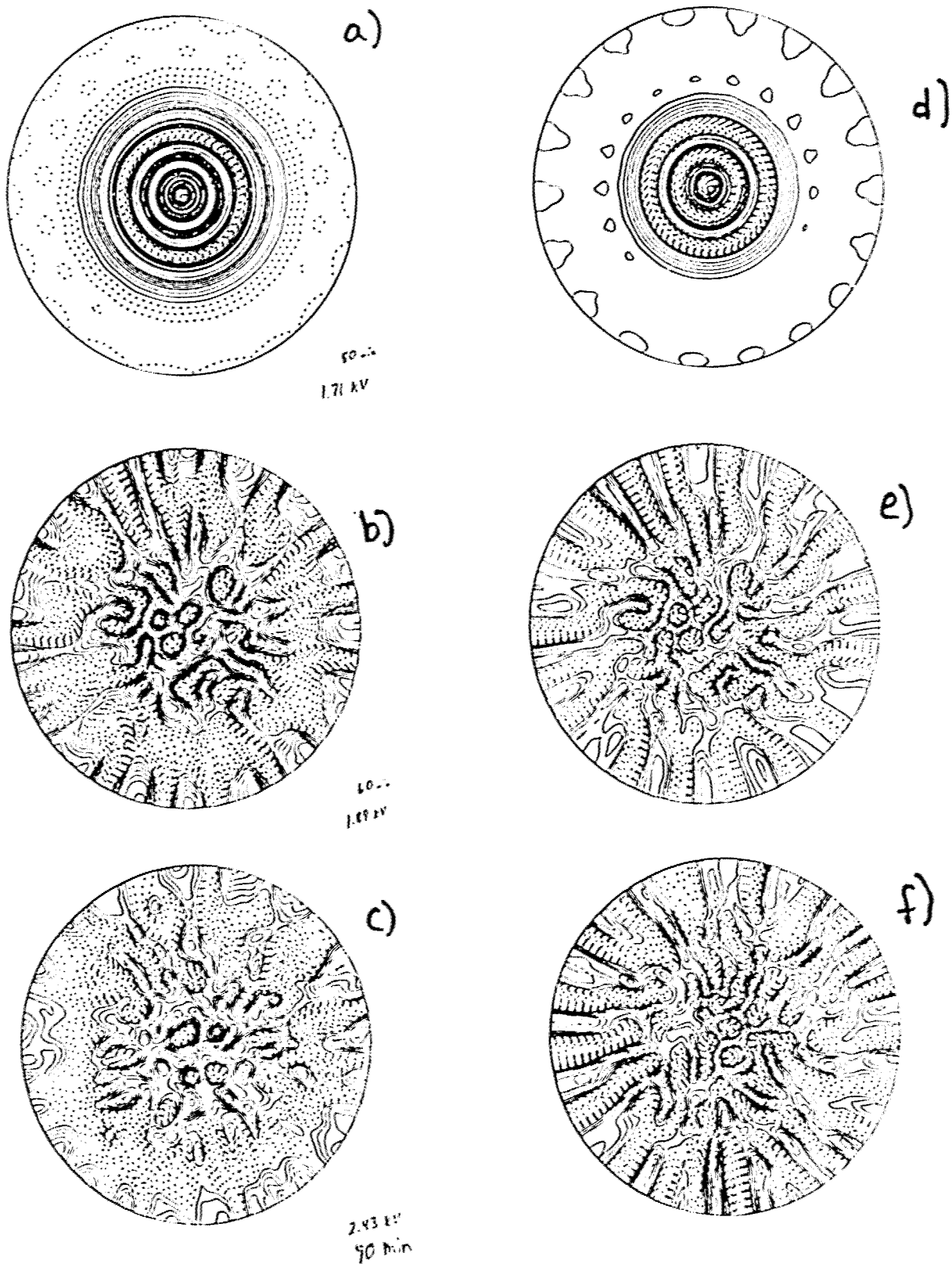

Figure 4) Glatzmaier simulation of Scenario 145. Polar projection (with latitude linearly mapped to radius) of contours of temperature (a-c) and vertical velocity (d-f) at mid-height for 1.71 kV (a, d), 1.89 kV (b, e) and 2.43 kV (c, f).

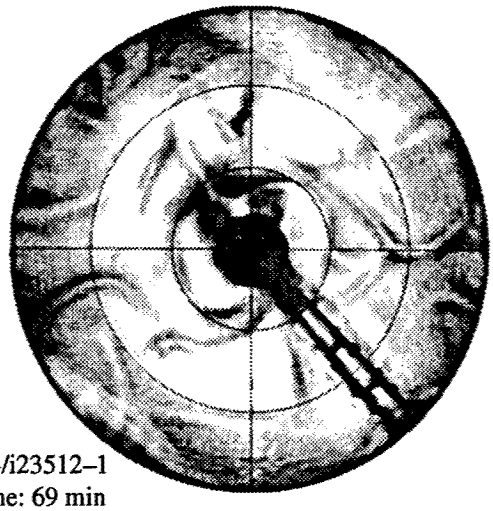

a) 194/i23512–1
Time: 69 min
kV: 1.460000

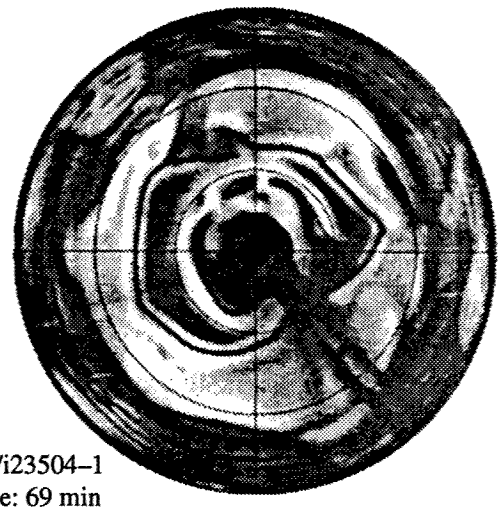

d) 194/i23504–1
Time: 69 min
kV: 1.460000

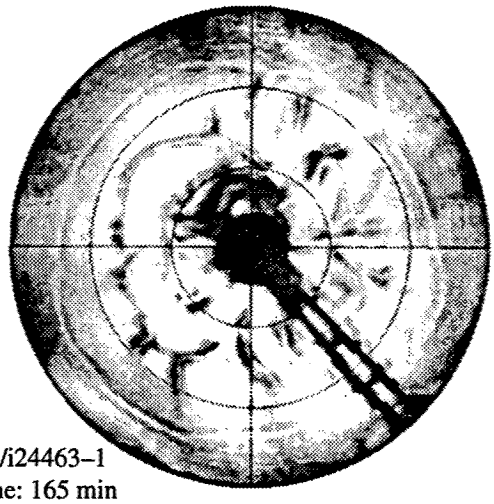

b) 194/i24463–1
Time: 165 min
kV: 3:130000

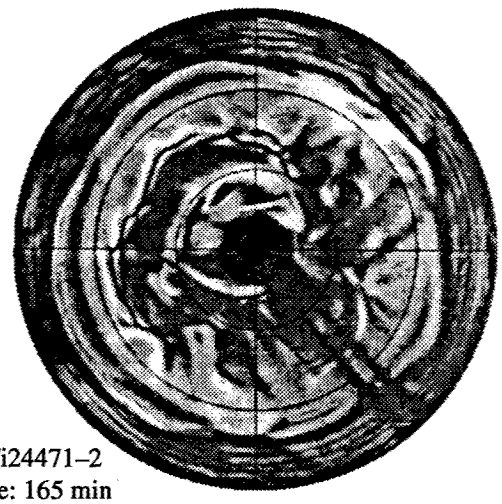

e) 194/i24471–2
Time: 165 min
kV: 3:16000

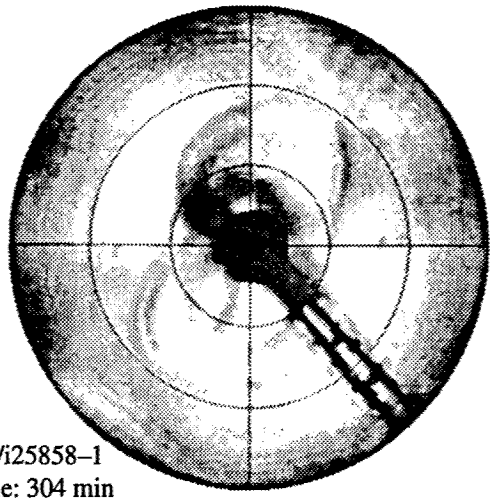

c) 194/i25858–1
Time: 304 min
kV: 1.260000

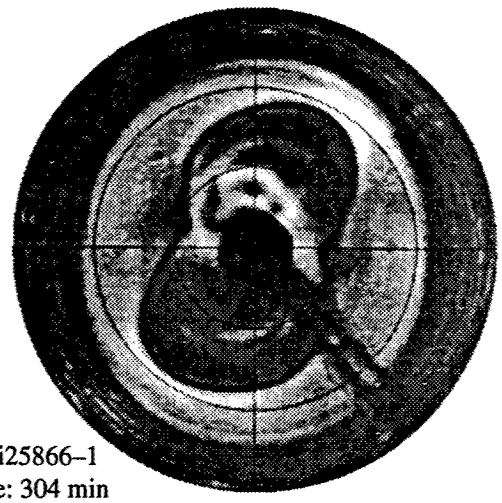

f) 194/i25866–1
Time: 304 min
kV: 1.260000

Figure 5. Unwrapping of GFFC Scenario 194, 48 second rotation period, mantle convection case, with no latitudinal temperature gradient. Grating in N/S orientation (a–c) and E/W orientation (d–f). a, d) During voltage plateau after increasing voltage. b, c) Pattern for high voltage. c, f) Just after voltage plateau after decreasing voltage.

(a)

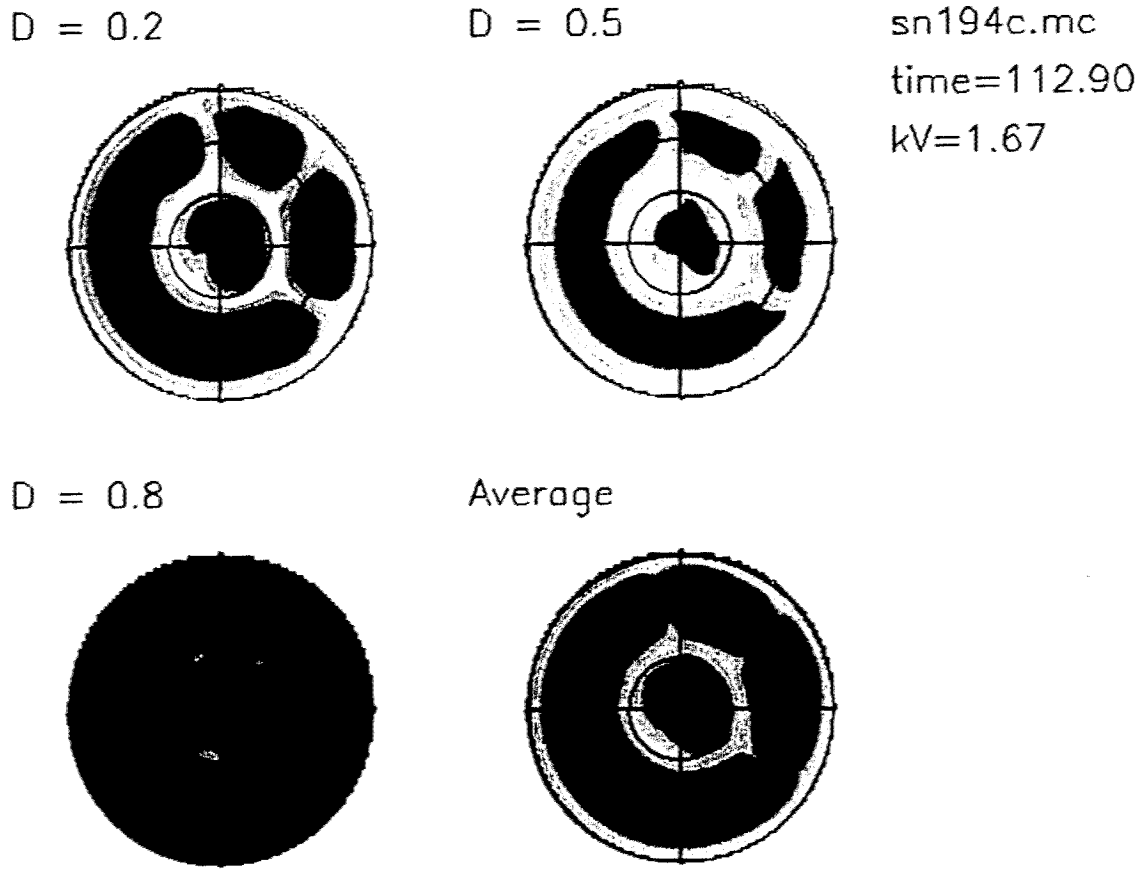

Figure 6) Miller-Leslie simulation of Scenario 194. *D* is the nondimensional height in the fluid layer of the temperature field shown. "Average" is the vertically averaged temperature field. This polar projection has latitude mapped linearly to radius as in the unwrapped GFFC images. **a)** 1.64 kV during the increasing voltage segment, **b)** 1.65 kV during the decreasing voltage segment.

(b)

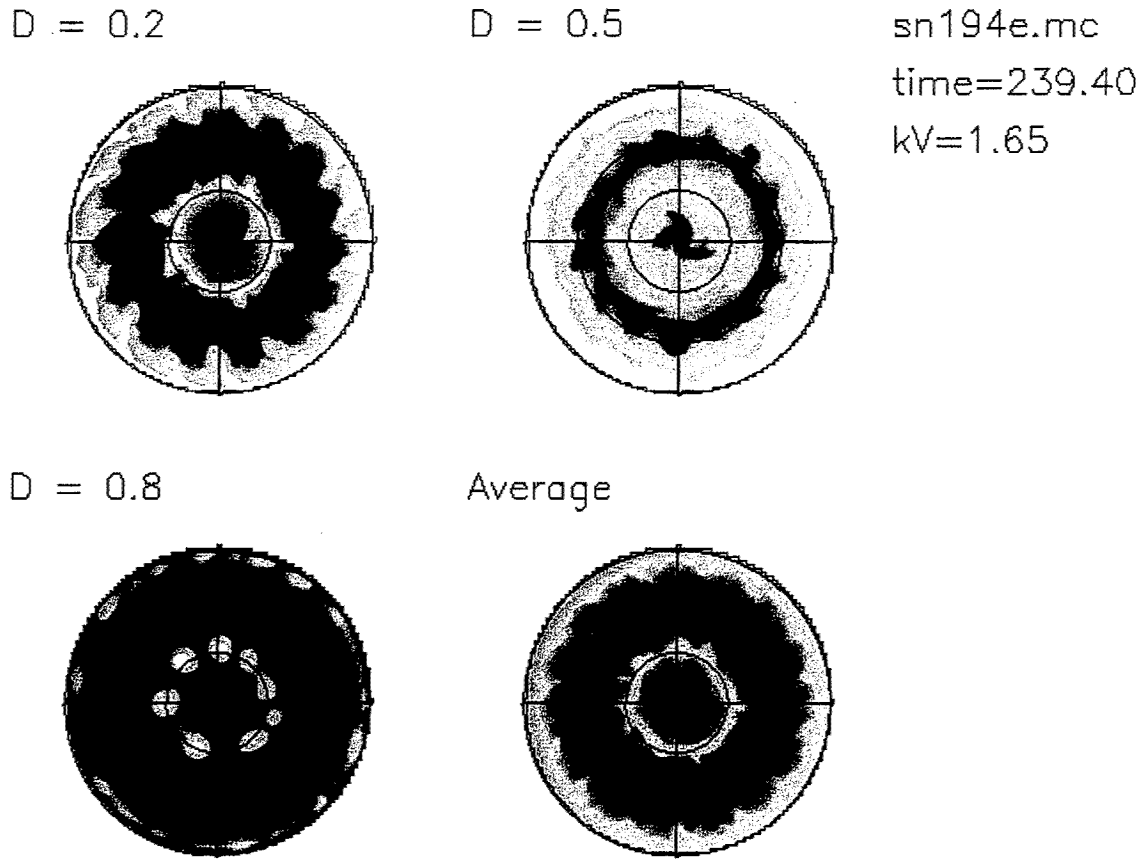

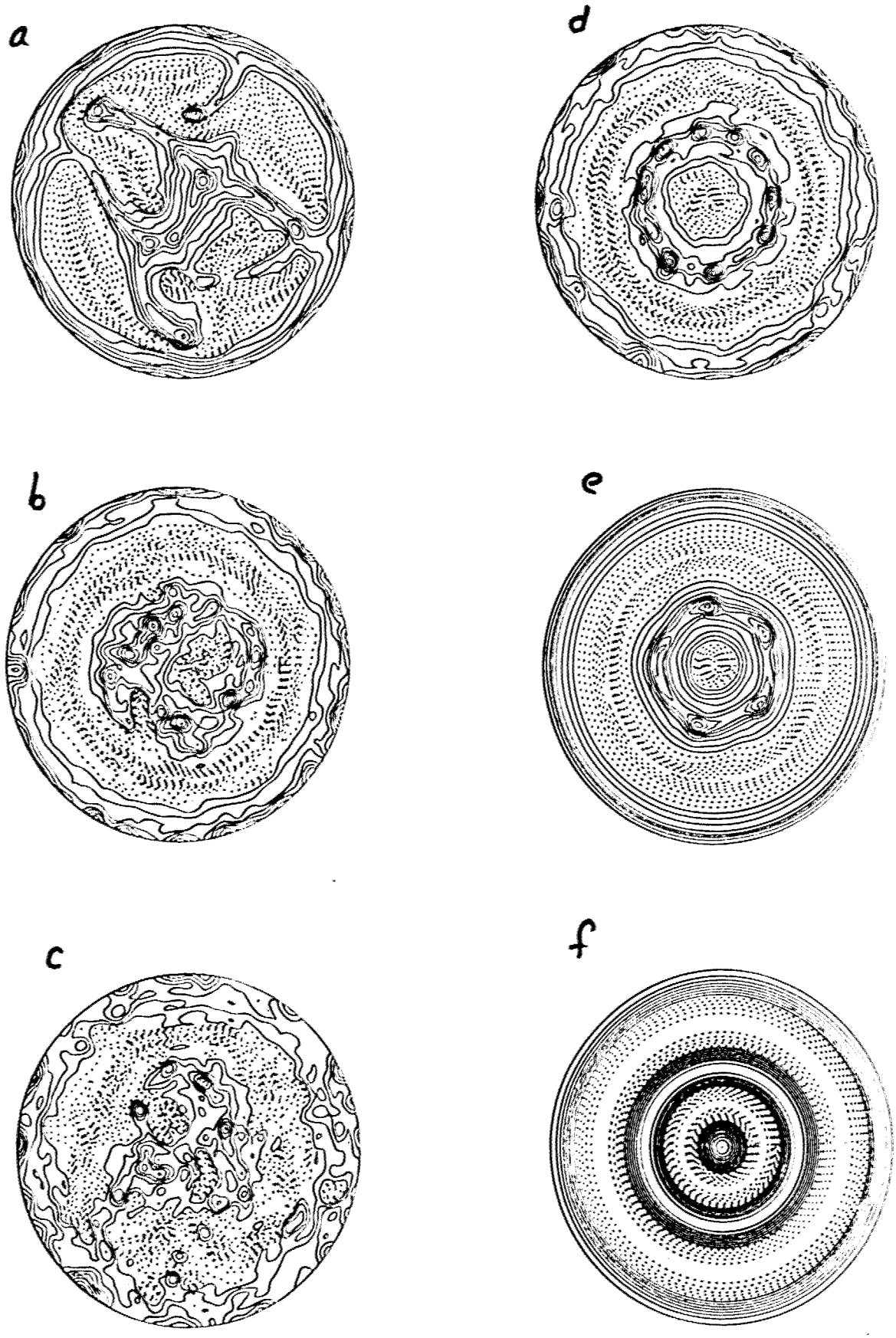

Figure 7) Glatzmaier simulation of Scenario 194. Polar projection (with latitude linearly mapped to radius) of contours of temperature at mid-height at the end of each hour during the run. **a)** 1.4 kV, **b)** 1.9 kV, **c)** 3.2 kV, **d)** 1.6 kV, **e)** 1.2 kV, **f)** 0.6 kV.

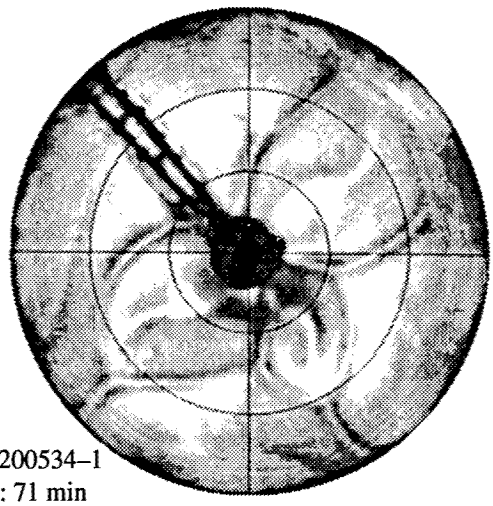

a) 195/i200534–1
Time: 71 min
kV: 1.460000

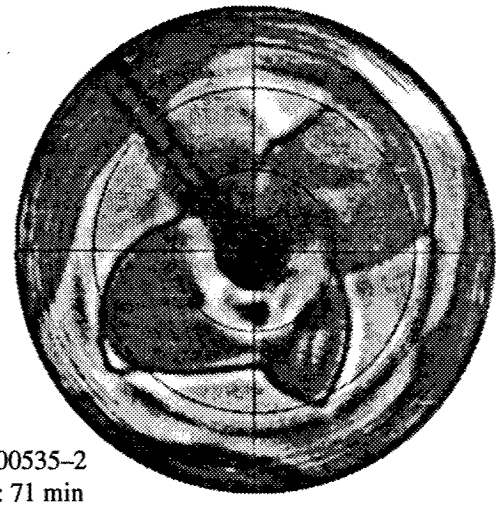

g) 194/i00535–2
Time: 71 min
kV: 1.460000

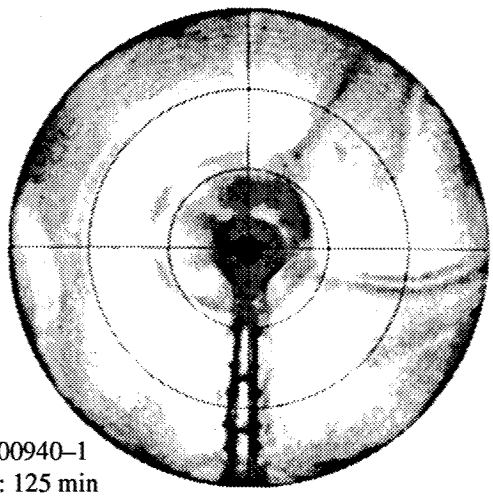

b) 195/i00940–1
Time: 125 min
kV: 1.880000

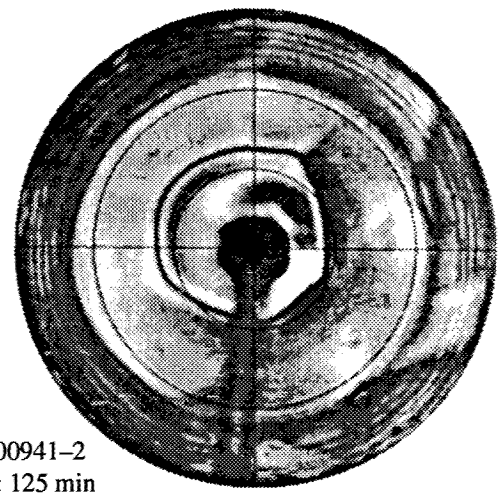

h) 195/i00941–2
Time: 125 min
kV: 1.880000

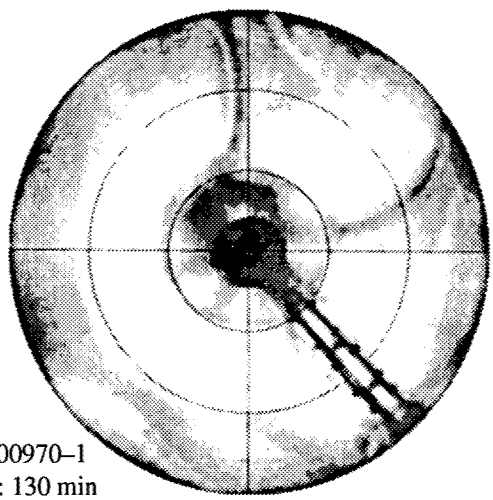

c) 195/i00970–1
Time: 130 min
kV: 2.010000

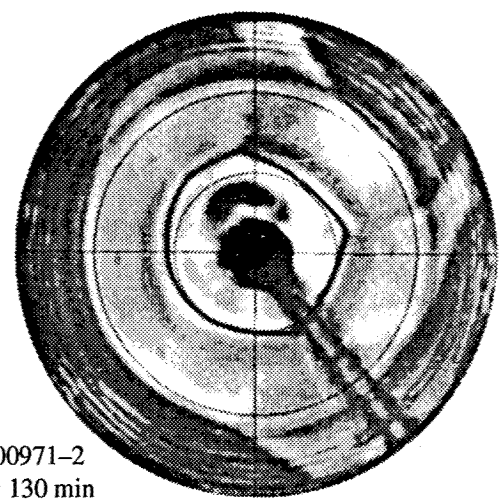

i) 195/i00971–2
Time: 130 min
kV: 2.01000

Figure 8. Unwrapping of GFFC Scenario 195, 128 second rotation period, mantle convection case, with no latitudinal temperature gradient. Grating in N/S orientation (a–f) and E–W orientation (g–l).

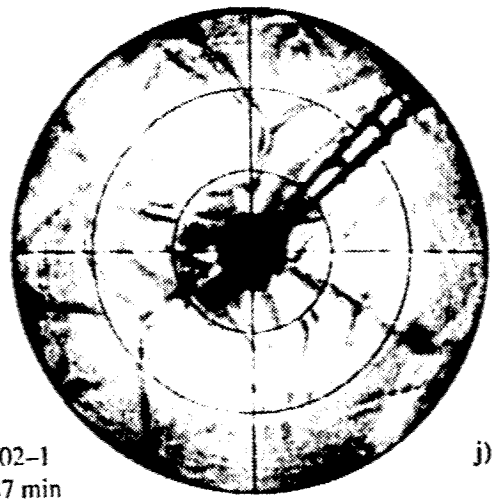

d) 195/i01402–1
Time: 187 min
kV: 2.940000

j) 195/i01403–2
Time: 187 min
kV: 2.94000

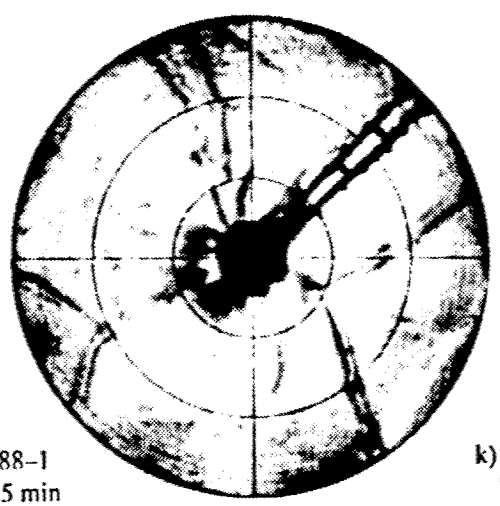

e) 195/i01688–1
Time: 225 min
kV: 1.640000

k) 195/i01689–2
Time: 225 min
kV: 1.640000

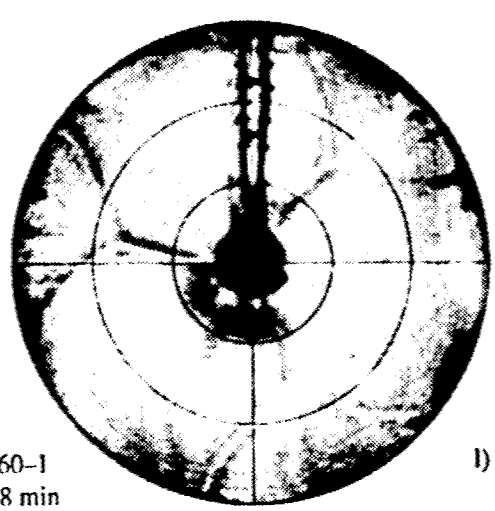

f) 195/i02460–1
Time: 328 min
kV: 0.890000

l) 195/i02461–2
Time: 328 min
kV: 0.890000

(a)

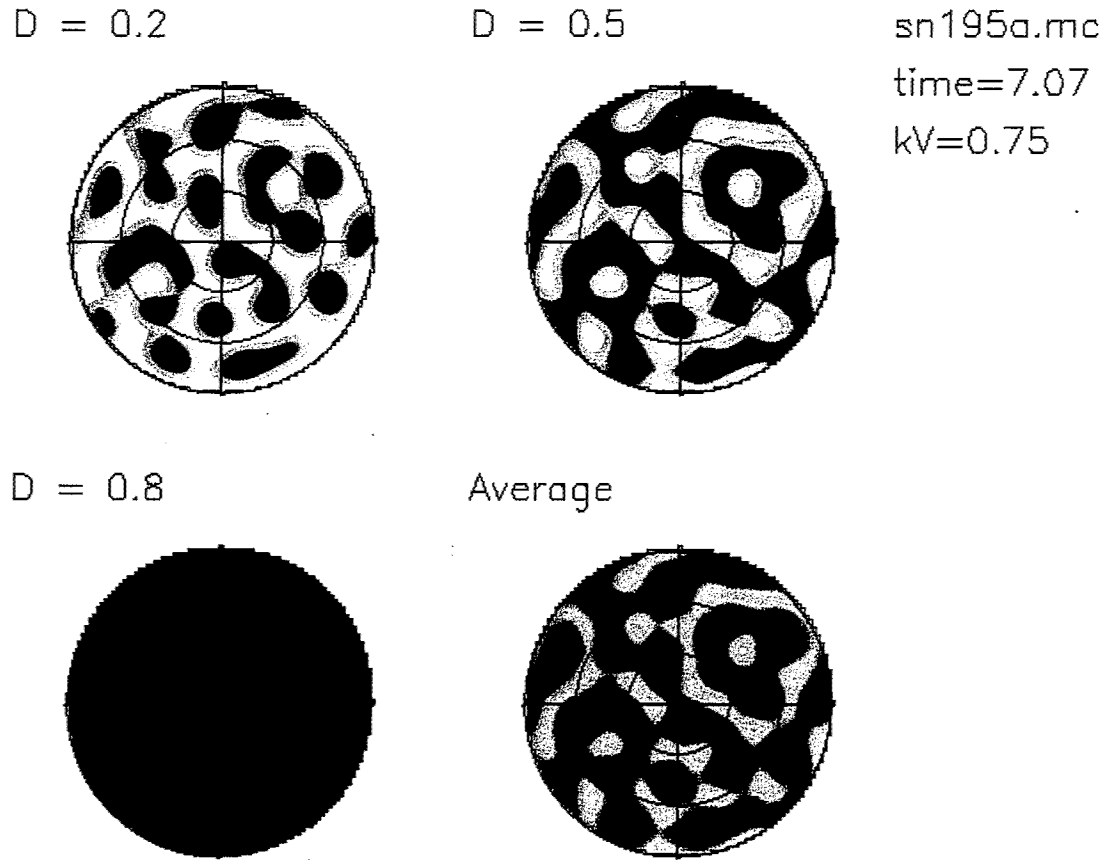

Figure 9) Miller-Leslie simulation of Scenario 195. *D* is the nondimensional height in the fluid layer of the temperature field shown. "Average" is the vertically averaged temperature field. This polar projection has latitude mapped linearly to radius as in the unwrapped GFFC images. **a)** 0.75 kV very early in the run, **b)** 1.93 kV just after the holding voltage. **c)** 2.97 kV. This basic pattern remained until the convection died away at 1.46 kV during the 2nd holding voltage.

(b)

D = 0.2

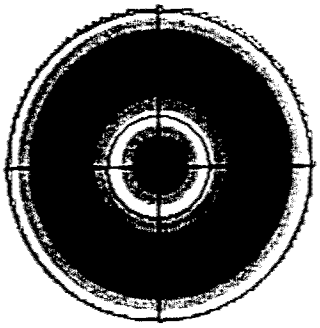

D = 0.5

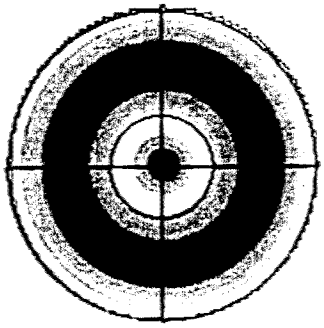

sn195c.mc
time=120.63
kV=1.93

D = 0.8

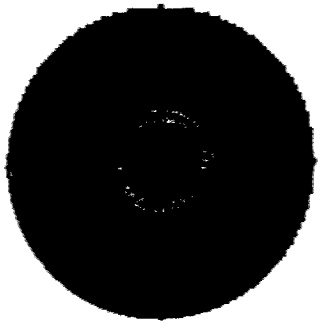

Average

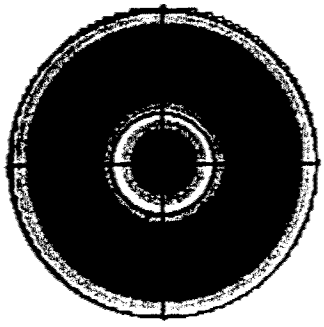

(c)

D = 0.2

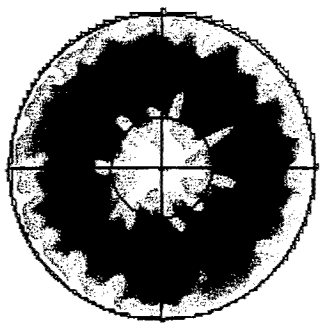

D = 0.5

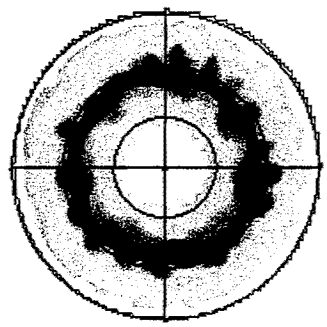

sn195e.mc
time=186.67
kV=2.97

D = 0.8

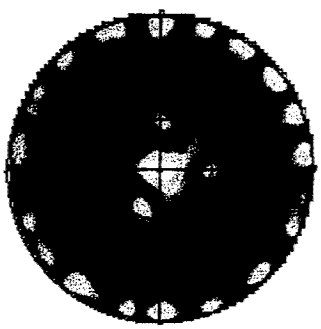

Average

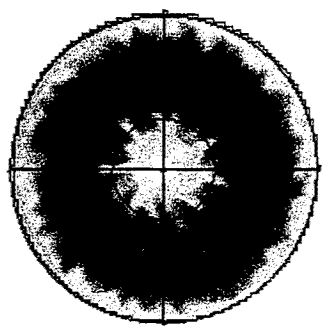

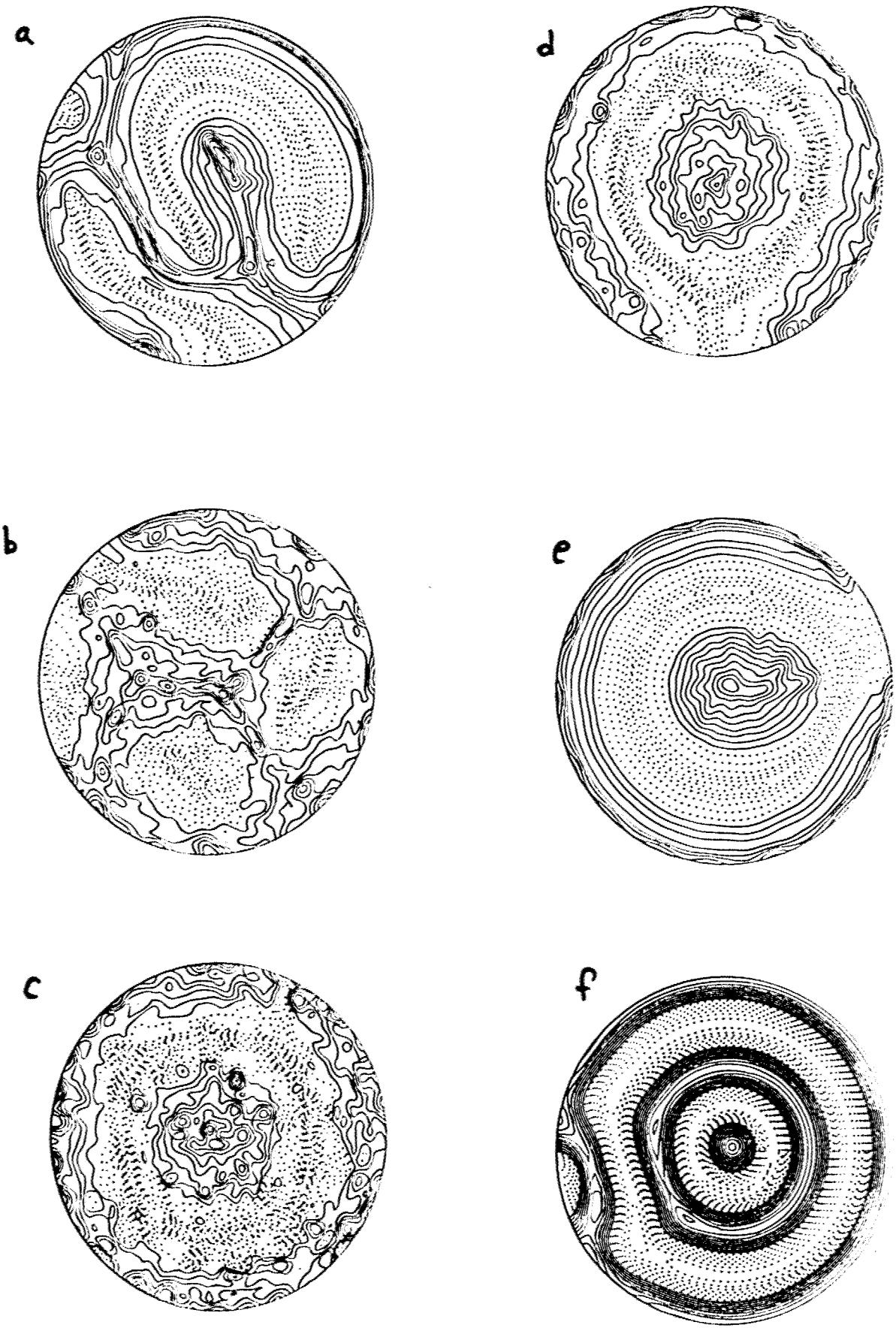

Figure 10) Glatzmaier simulation of Scenario 195. Polar projection (with latitude linearly mapped to radius) of contours of temperature at mid-height at the end of each hour during the run. **a)** 1.5 kV, **b)** 1.9 kV, **c)** 3.2 kV, **d)** 1.5 kV, **e)** 1.2 kV, **f)** 0.6 kV.

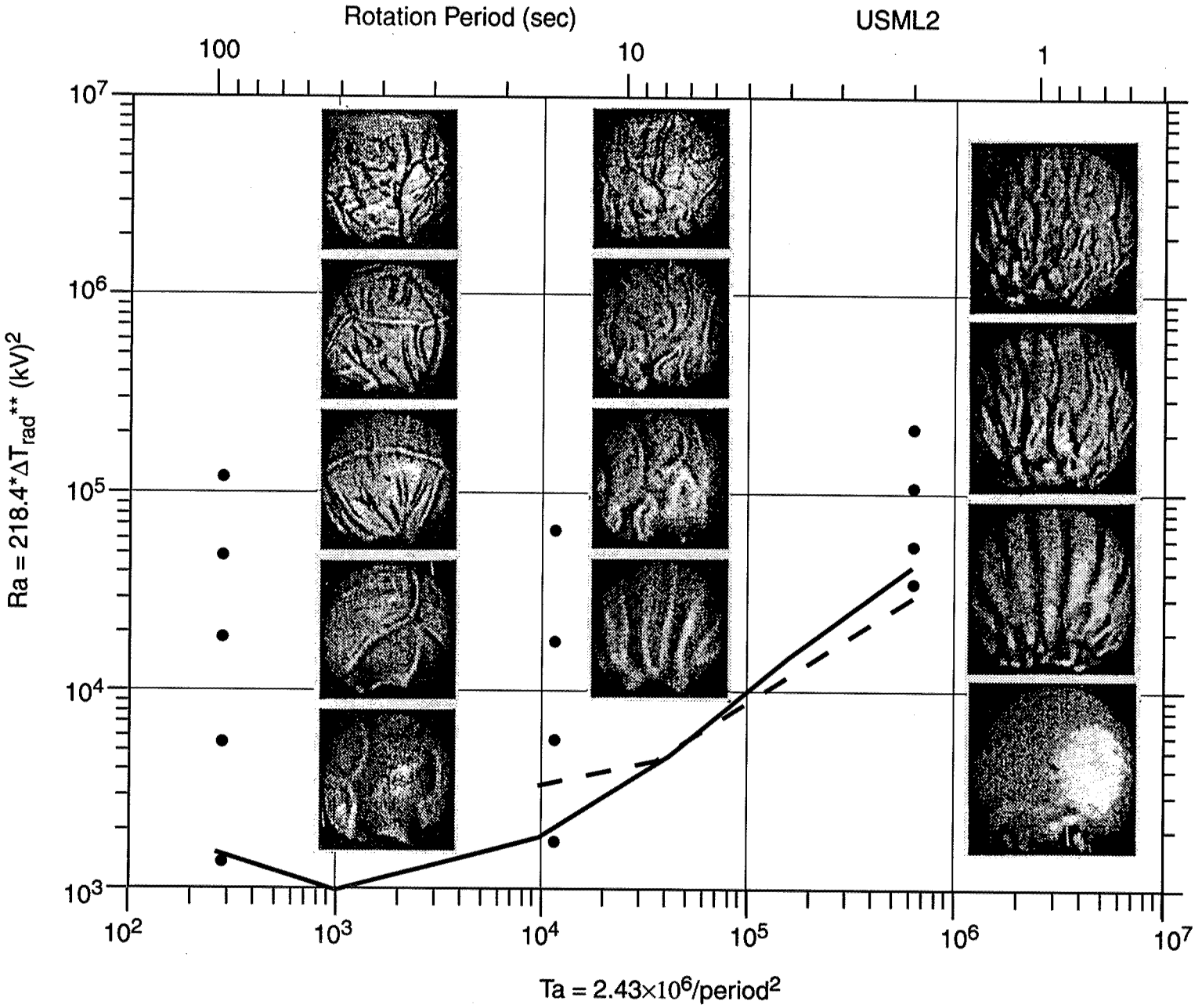

Figure 11. Regime diagram from the USML2 GFFC flight experiment showing qualitative results for several Rayleigh number ramp up experiments with symmetric heating (H=0). Each image is a single snapshot with the south pole at the bottom and the equator at the top. The solid (dashed) curve shows the onset of banana cell (polar wavy) convection. Each image corresponds to the dot to its left, in vertical order.

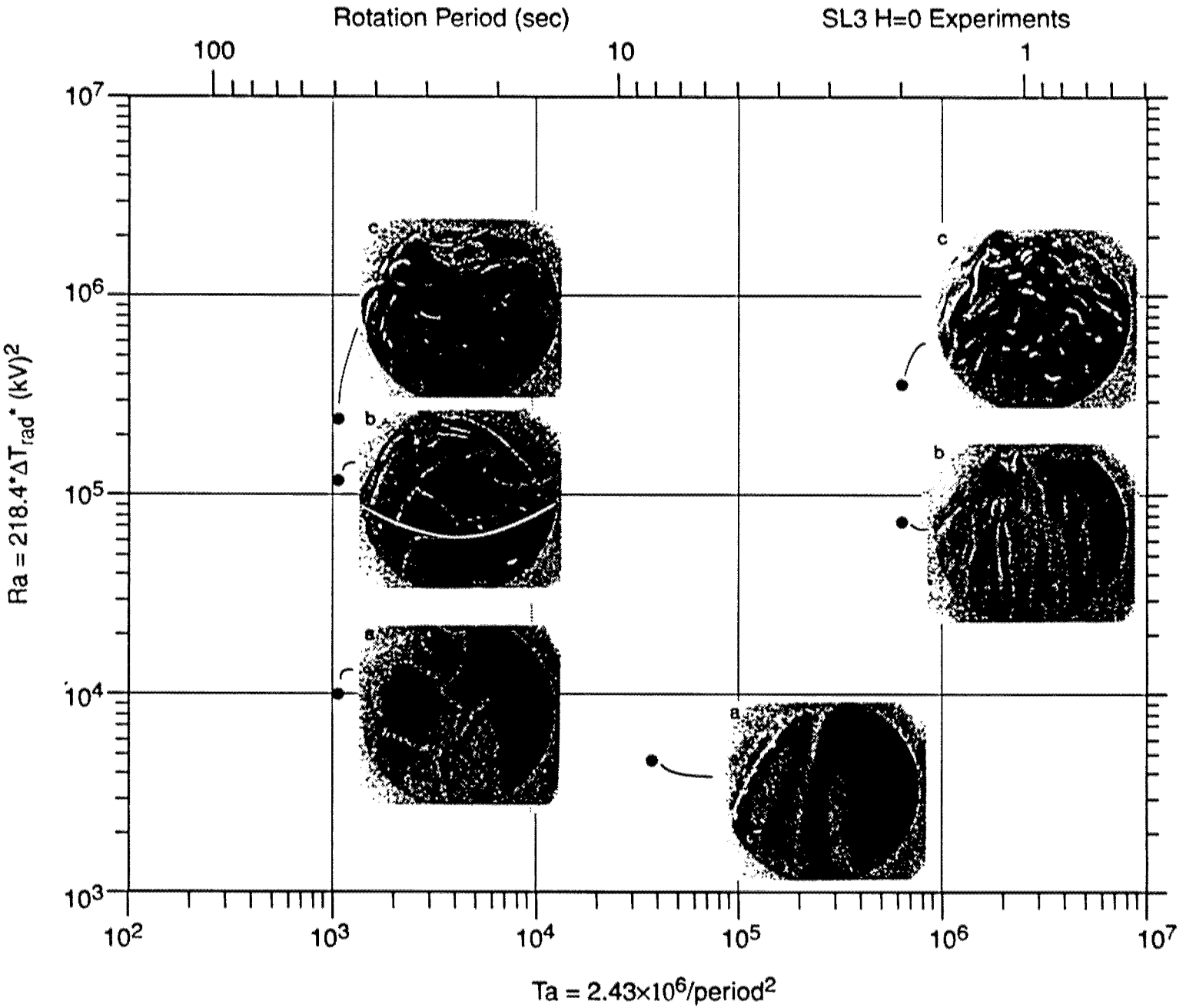

Figure 12–19. Pre USML2 flight regime diagrams organized by heating function, H (or organized by "SL3", "M–L model", "Glatzmaier model?")

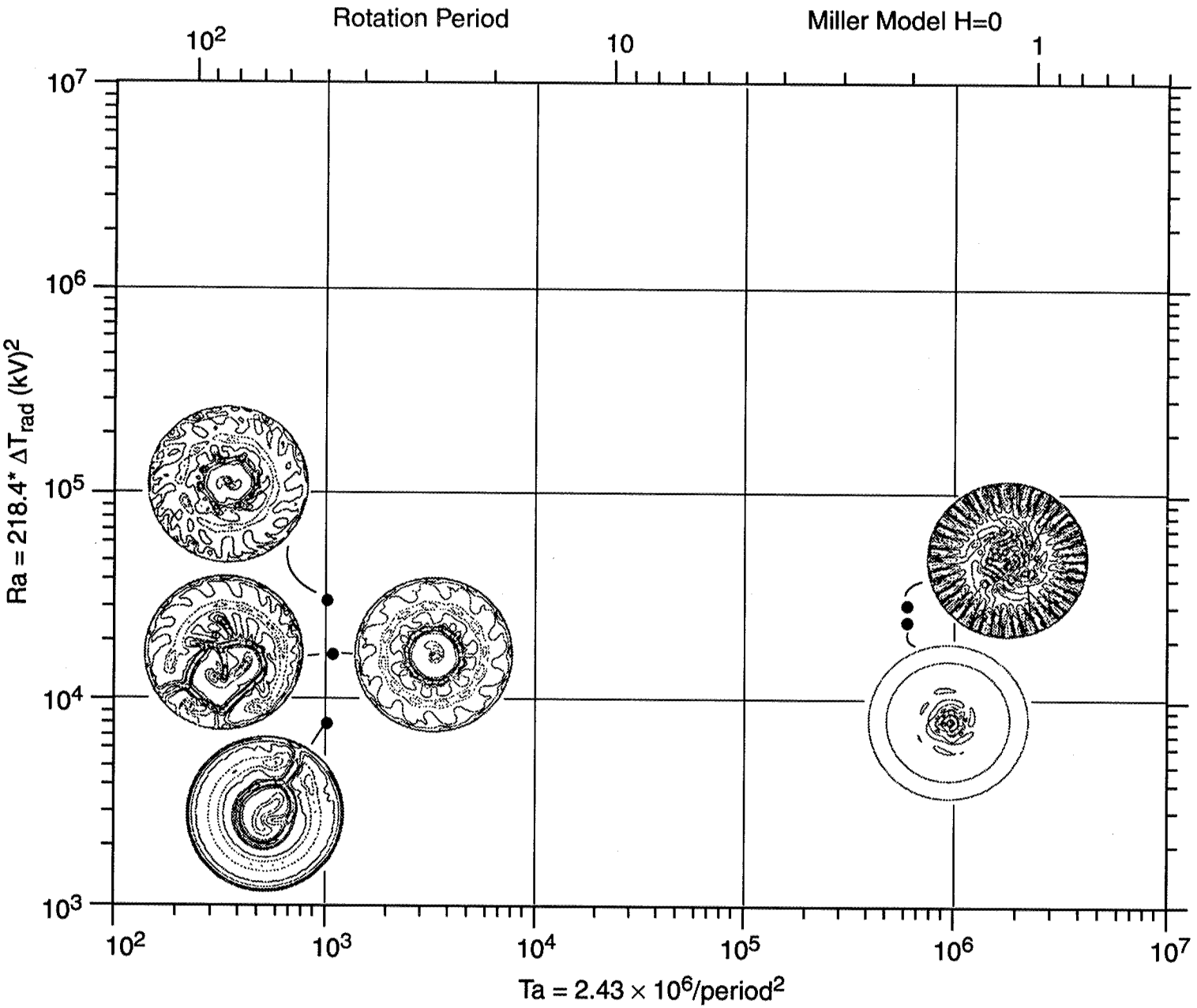

Figure 13. Computational simulations: Miller model H=0.

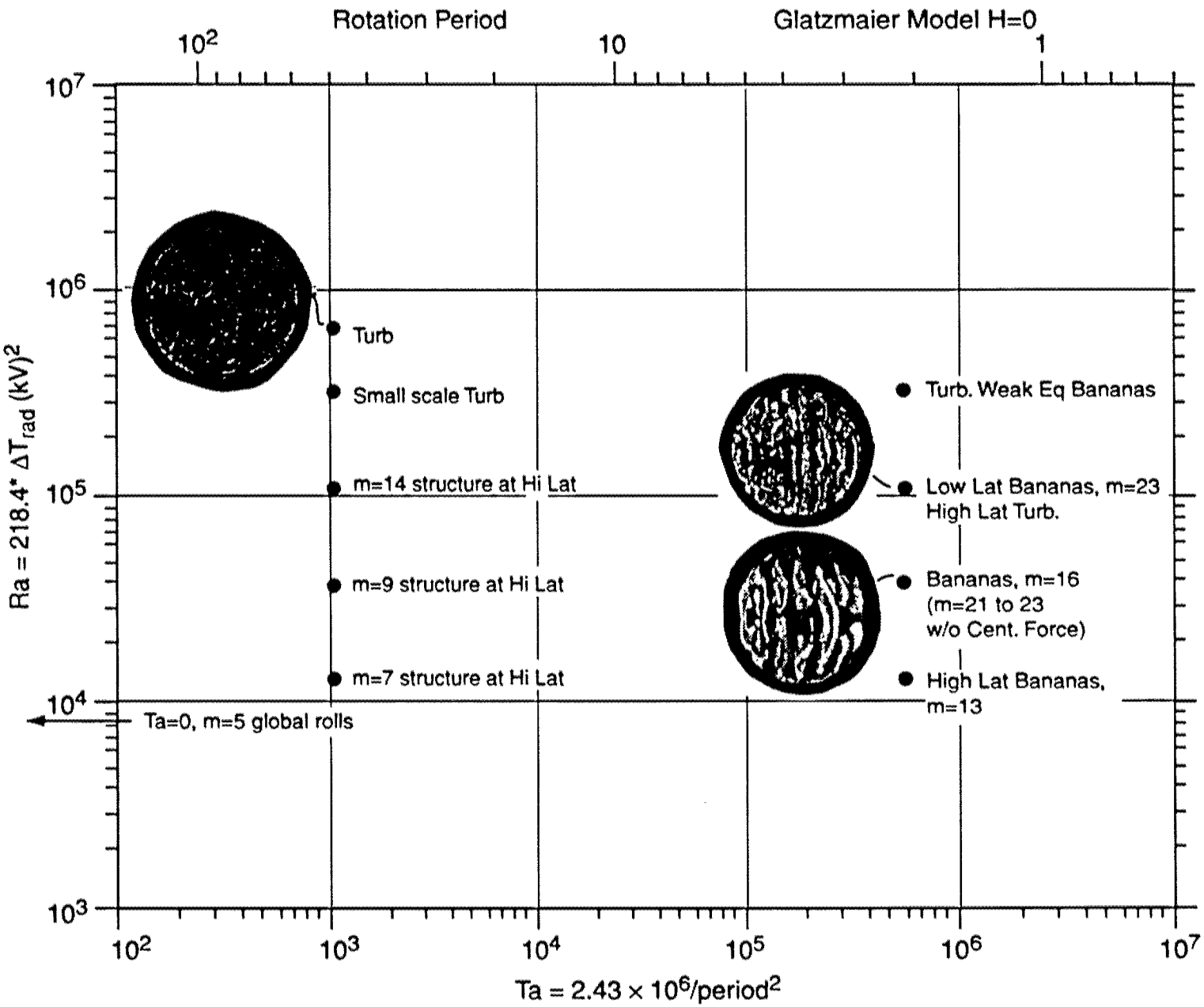

Figure 14. Computational simulations: Glatzmaier model H=0.

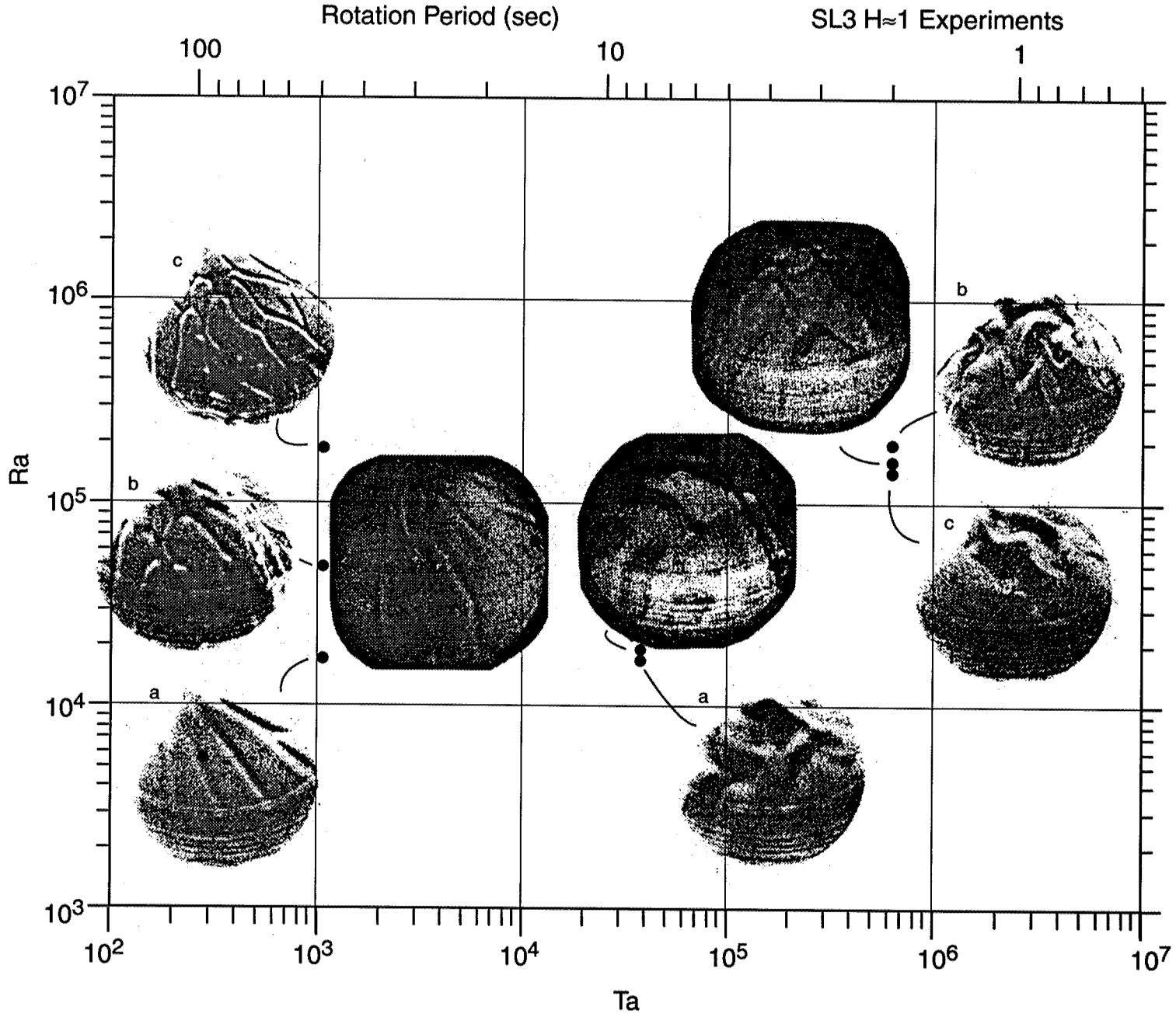

Figure 15. Summary of SL–3, H=1 states.

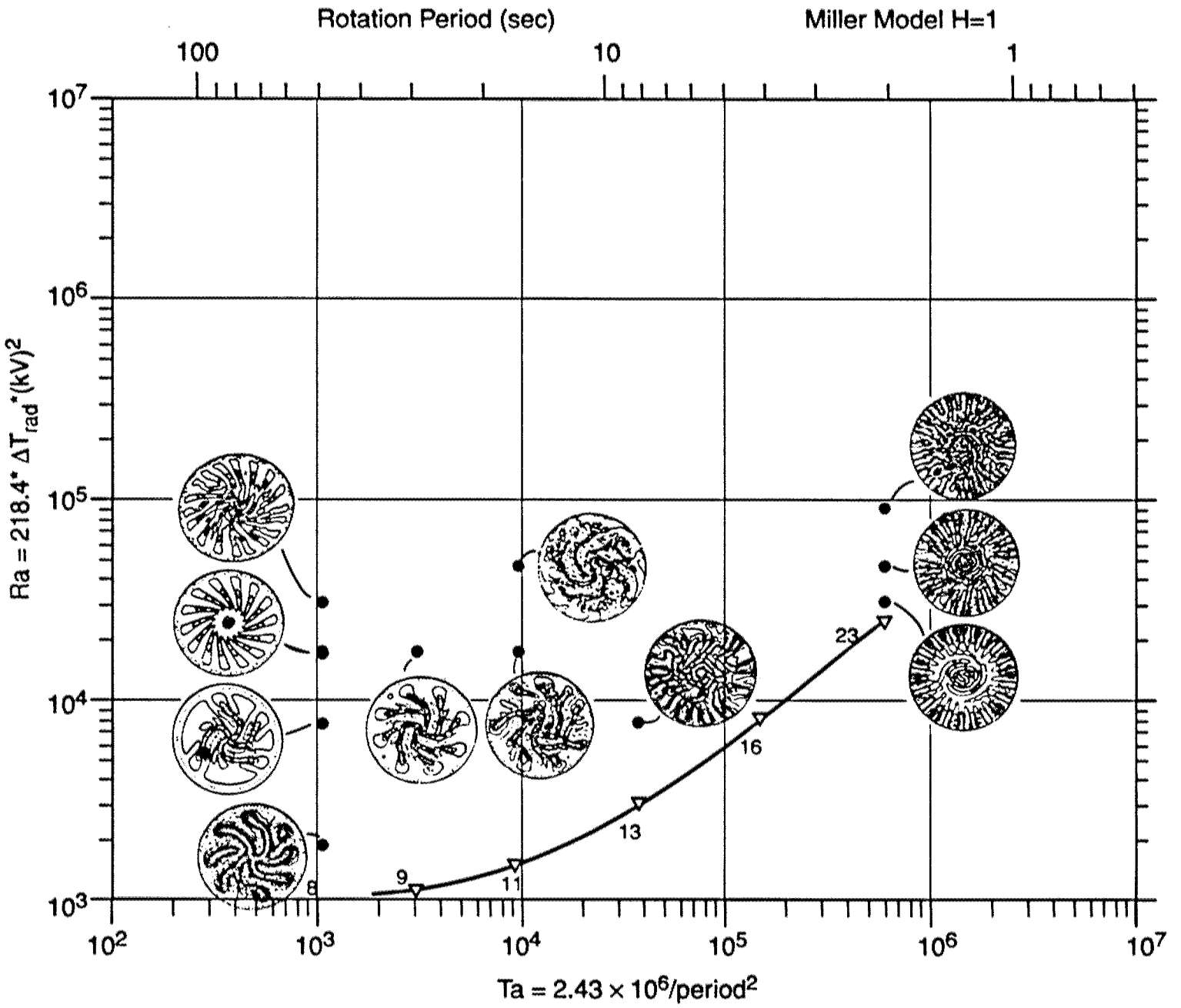

Figure 16. Miller Model H = 4.

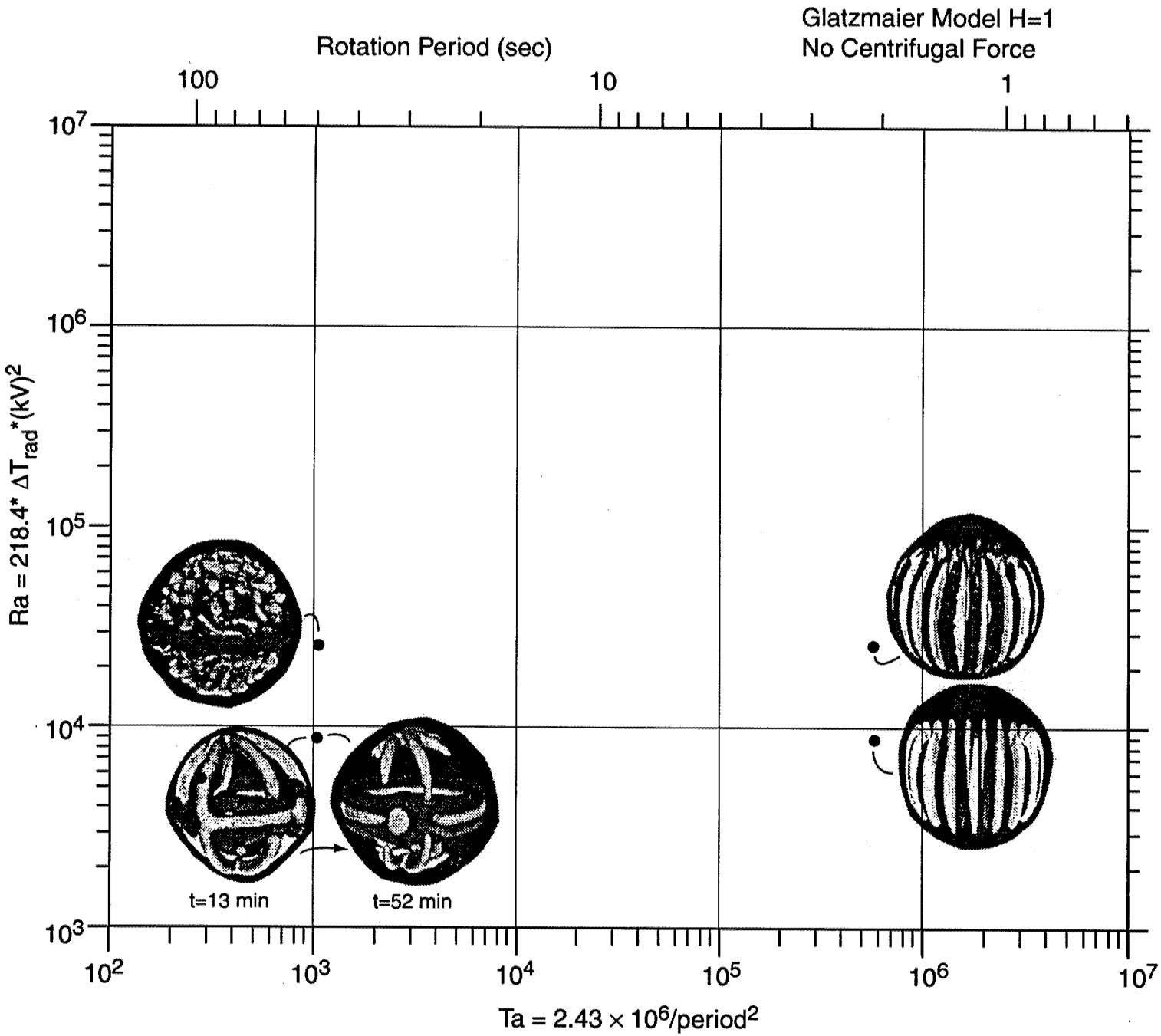

Figure 17. Glatzmaier Model H = 1.

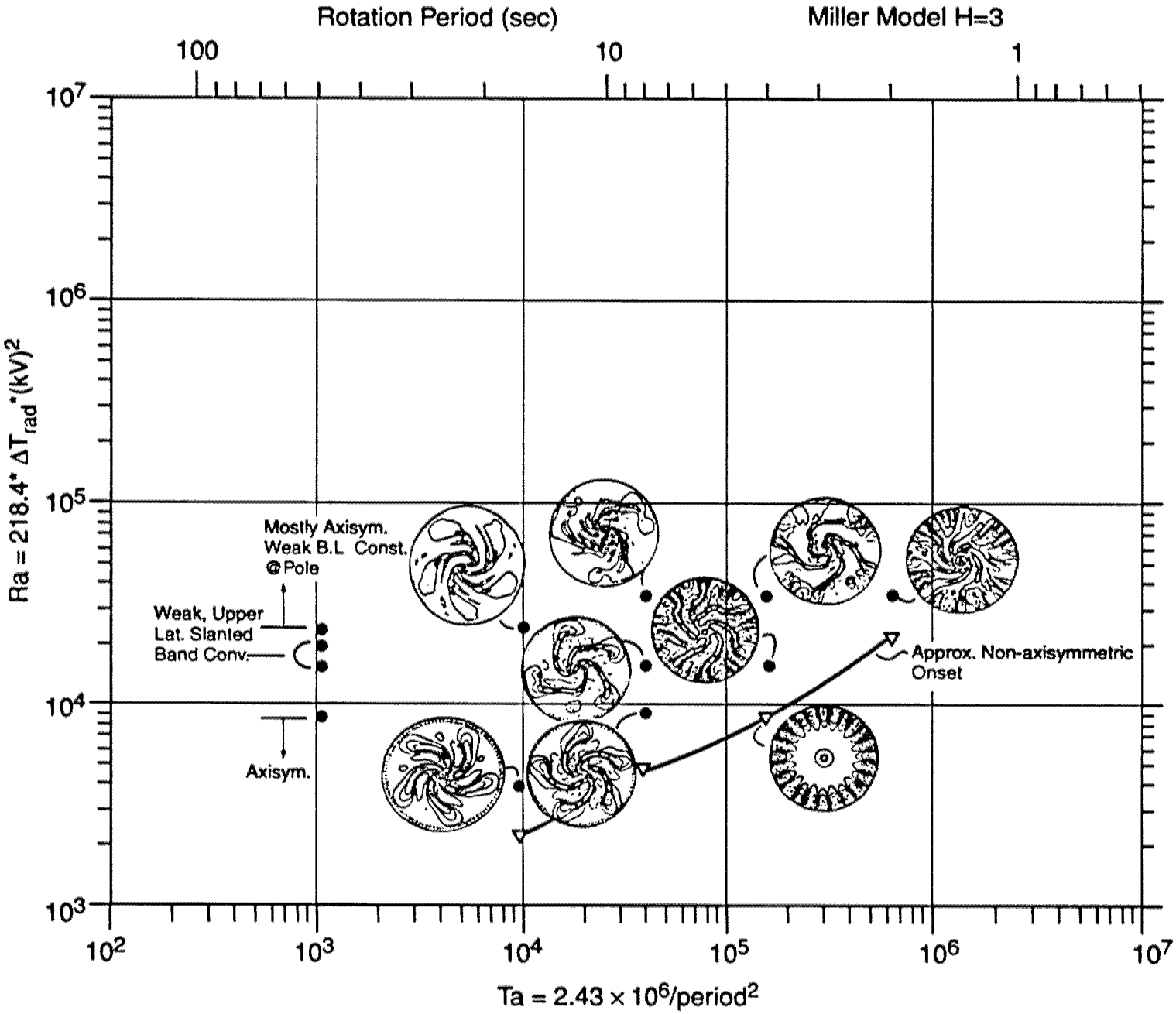

Figure 18. Miller Model H = 3.

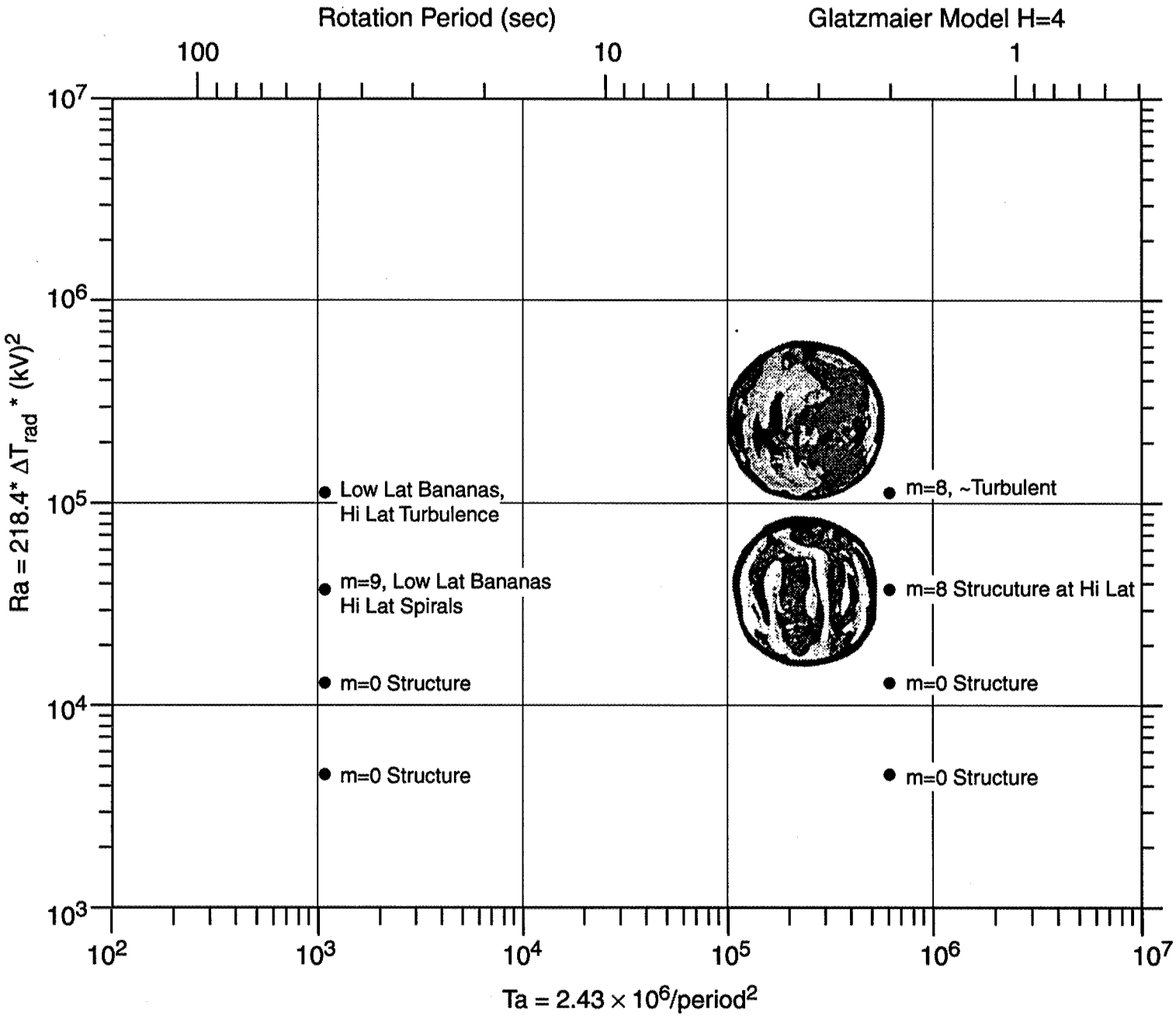

Figure 19. Glatzmaier Model, H = 4.

REPORT DOCUMENTATION PAGE

Form Approved
OMB No. 0704-0188

1. AGENCY USE ONLY *(Leave Blank)*	2. REPORT DATE	3. REPORT TYPE AND DATES COVERED
	September 1999	Technical Publication

4. TITLE AND SUBTITLE
The Geophysical Fluid Flow Cell Experiment

5. FUNDING NUMBERS
NAS8–31958

6. AUTHORS
J.E. Hart,* D. Ohlsen,* S. Kittelman,* N. Borhani,*
F. Leslie, and T. Miller

7. PERFORMING ORGANIZATION NAMES(S) AND ADDRESS(ES)
George C. Marshall Space Flight Center
Marshall Space Flight Center, Alabama 35812

8. PERFORMING ORGANIZATION REPORT NUMBER
M–938

9. SPONSORING/MONITORING AGENCY NAME(S) AND ADDRESS(ES)
National Aeronautics and Space Administration
Washington, DC 20546–0001

10. SPONSORING/MONITORING AGENCY REPORT NUMBER
NASA/TP—1999–209576

11. SUPPLEMENTARY NOTES
Prepared for the Microgravity Sciences and Applications Department, Science Directorate
*University of Colorado, Boulder, CO 80309

12a. DISTRIBUTION/AVAILABILITY STATEMENT
Unclassified-Unlimited
Subject Category 34
Standard Distribution

12b. DISTRIBUTION CODE

13. ABSTRACT *(Maximum 200 words)*

The Geophysical Fluid Flow Cell (GFFC) experiment performed visualizations of thermal convection in a rotating differentially heated spherical shell of fluid. In these experiments dielectric polarization forces are used to generate a radially directed buoyancy force. This enables the laboratory simulation of a number of geophysically and astrophysically important situations in which sphericity and rotation both impose strong constraints on global scale fluid motions. During USML–2 a large set of experiments with spherically symmetric heating were carried out. These enabled the determination of critical points for the transition to various forms of nonaxisymmetric convection and, for highly turbulent flows, the transition latitudes separating the different modes of motion. This paper presents a first analysis of these experiments as well as data on the general performance of the instrument during the USML–2 flight.

14. SUBJECT TERMS
spherical convection, microgravity of fluid dynamics, planetary atmospheres

15. NUMBER OF PAGES
107

16. PRICE CODE
A06

17. SECURITY CLASSIFICATION OF REPORT	18. SECURITY CLASSIFICATION OF THIS PAGE	19. SECURITY CLASSIFICATION OF ABSTRACT	20. LIMITATION OF ABSTRACT
Unclassified	Unclassified	Unclassified	Unlimited